Development of a high-resolution soft x-ray monochromator and its application to the study on surface chemistry and surface magnetism

A Thesis
Submitted to
the university of Tokyo
for the Degree
of
Doctor of Science
(Hakase(Rigaku))

by

Kenta Amemiya

December, 1999

Acknowledgements

The present study has been carried out under the supervision of Professor Toshiaki Ohta (The University of Tokyo). I would like to express my heartfelt thank to him for his continual encouragement and valuable suggestions.

I gratefully acknowledge Mr. Yoshinori Kitajima (Photon Factory, Institute of Materials Structure Science, High Energy Accelerator Research Organization). He has promoted the construction of the new beamline powerfully, and has given valuable discussions and assistance both for the development of the monochromator (BL-11A) and the experiments with it.

I would like to express sincere gratitude to Professor Toshihiko Yokoyama (The University of Tokyo) for his various assistance on the experiments and analyses, as well as helpful discussions and encouragement.

I am deeply grateful to Professor Kenji Ito (Photon Factory) for his valuable discussions on the design of the monochromator.

I would like to thank Dr Masato Koike (Japan Atomic Energy Research Institute), Professor Shoji Suzuki (Tohoku University), Professor Eiji Ishiguro (Ryukyu University) and Dr. Kazuo Sano (Shimadzu Corporation) for their valuable suggestions about the monochromator and the grating.

I wish to express thank to Dr. Hiroshi Kondo (The University of Tokyo) and Dr. H.-W. Yoem (The University of Tokyo) for their various discussions and encouragement.

I am grateful to the members of the BL-11A scrap-and-build group for their assistance on the construction of the monochromator.

I wish to express my gratitude to Professor Tsuneharu Koide (Photon Factory) for his valuable suggestions and information on the XMCD measurements, and professor Akio Kimura (Hiroshima University) for his helpful information on the equipment for the magnetic measurements.

I wish to thank Mr. Yoshiki Yonamoto, Dr. Shigeru Terada (Mitsubishi Chemical Corporation), Ms. Mariko Miyachi, Mr. Hiroki Tsukabayashi (Daiwa Institute of Research Corporation), Mr. Daiju Matusmura, Mr. Akira Nambu and Mr. Yasuo Nakayama (The University of Tokyo, if not indicated) for their various assistance on the experiments.

I am grateful for the financial support of Research Fellowships of the Japan Society for the Promotion of Science for Young Scientist (No. 199707918). The present study has been performed under the approval of the Photon Factory Program Advisory Committee (PF-PAC No. 97G312, 98G003 and 99G159).

Finally, thanks are given to all the members of the laboratories of Professor Toshiaki Ohta and department of chemistry for their encouragement and various discussions.

Contents

Chapter 1
General introduction

X-ray absorption spectroscopy with a core level excitation has been drastically advanced for these decades, thanks to the establishments and improvements of the continuous and intense x-ray sources, *i.e.* synchrotron radiation (SR). One of the most important advantages of the core-level x-ray absorption is the element selectivity, owing to the localization of the core level within a narrow region around an atomic nucleus. Therefore, the x-ray absorption techniques have been widely applied in order to investigate local geometrical and electronic structures around a specific element. The atomic and electronic structures are studied by means of extended x-ray-absorption fine-structure (EXAFS) and near-edge x-ray-absorption fine-structure (NEXAFS), both of which utilize the linearly polarized x rays. In addition, x-ray magnetic circular dichroism (XMCD) has been recently developed by using the circularly polarized x rays from SR. An important advantage of the XMCD technique is that one can separately obtain the spin and orbital magnetic moments for each element.

Surface chemistry, especially the adsorption of atoms and molecules on solid surfaces, has been paid much attention because of the importance of catalytic chemistry, petrochemistry and electric chemistry. Surface geometrical structures and electronic properties have been widely investigated to understand the adsorbate-substrate interaction as well as the adsorbate-adsorbate one. These interactions play essential roles in various surface reactions. On the other hand, magnetic thin films and multilayers have attracted much interest because of their extraordinary properties such as enhancement of the magnetic moments, giant magnetoresistance (GMR) and magnetic anisotropy. These properties can directly contribute to the progress in the computer science.

The element selectivity and high sensitivity of the x-ray absorption techniques allow examining small amounts of specimens such as submonolayer adsorbates and ultrathin films on solid surfaces. The surface geometrical structures, electronic properties and magnetic characters can be investigated with the x-ray absorption measurements and the obtained information is quite essential for the advances in the surface chemistry and surface magnetism. The objective of the present study is applying the x-ray absorption techniques, XAFS (x-ray absorption fine structure, including EXAFS and NEXAFS) and XMCD, to the investigations of the surface geometrical structures and electronic properties as well as the surface magnetism.

1-1. Surface chemistry and surface magnetism

Surface geometry and electronic property are essential parameters in the surface chemistry. A clue to understand the mechanism of surface reaction can be obtained from the adsorption structure of molecules. For instance, the adsorption structures have been studied for ethylene (C_2H_4) on Ni(111) and for acetylene (C_2H_2), which is formed by heating C_2H_4/Ni(111) [1]. It was concluded that ethylene adsorbs with its molecular axis parallel to the surface and locates at the aligned bridge site, where each C atom is approximately just above the Ni atom. Upon heating, the dehydrogenation occurs and the adsorption site of acetylene was found to be the cross bridge one, where each C atom locates approximately at the hollow site. This means that a rotation of the molecular axis occurs in the dehydrogenation process.

Adsorption structures of intermediates, not only reactants and products, have been also extensively studied, in order to obtain geometrical information during the surface reaction. Formate (HCOO) and methoxy species (CH_3O) are known as intermediate species in methanol synthesis, and their structures have been investigated by use of many techniques. In the case of adsorption on Cu(100), it has been found that formate adsorbs on the aligned bridge site via O atoms and that its molecular plane is almost perpendicular to the surface [2,3]. It has been reported, on the other hand, that the methoxy species adsorbs also via O atom but the adsorption site is somewhere between the hollow and bridge ones [4].

Adsorption site plays an important role for the properties of the adsorbed molecules. Interactions between the molecular orbital and the substrate one are significantly affected by the symmetry and coordination number of the adsorption site. In the case of CO adsorption on Ni surfaces, for instance, many structural studies have been performed. It has been revealed that CO adsorbs mainly on the atop site of Ni(100) at ~0.5 ML (monolayer) coverage [5,6], while the hollow site adsorption have been reported for CO/Ni(111) around the same coverage [7,8]. A surface stress study [9] showed that the CO adsorption on Ni(100) induces tensile stress, while the compressive one was observed for CO/Ni(111). From these results, it has been suggested that the charge transfer from Ni $d\pi$ ($d_{xz,yz}$, where z axis is normal to the surface) orbitals to CO $2\pi^*$ ones is more enhanced for the atop adsorption on Ni(100), compared with the hollow site adsorption on Ni(111). This difference can be simply understood, considering that the atop site adsorption leads to the "pure" π type bonding between the Ni $d\pi$ and CO $2\pi^*$ orbitals.

The adsorption of the molecule is significantly affected by many factors such as kind of substrate, coverage and temperature. An example for the substrate effect can be found in the adsorption of SO_2 on metal surfaces. It has been reported that SO_2 adsorbs on Ni(100) with its molecular plane parallel to the surface [10], while the perpendicular orientation has been found on Cu(100) [11] and Ag(110) [12,13]. This difference can be explained by the electronic structures of these surfaces; Ni

$3d$ bands lie more shallowly and interact more significantly with the π^* orbital of SO_2, compared to Cu and Ag. Since the π^* orbital plays an important role in the adsorption of SO_2 on the metal surfaces, the stronger π-type interaction lead to the flat lying adsorption structure. The difference in the strength of the π interaction was confirmed by means of NEXAFS, where the larger charge transfer from Ni to SO_2 π^* was observed, compared to those from Cu and Ag [10]. This implies the close correlation between the geometrical structures and the electronic properties.

The coverage dependence of the surface structure also has been widely investigated. The adsorption geometry of thiophenol (C_6H_5SH) [14] and alkanethiol [$CH_3(CH_2)_{n-1}SH$] [15], for instance, has been known to depend drastically on the coverage. It was found that thiophenol adsorbs on Ni(100) with its molecular plane parallel to the surface at low coverage, while the molecular plane comes to stand up at higher coverage [14]. A similar coverage dependence was observed for the alkanethiol adsorption [15]. In the case of CO adsorption mentioned above [5–8], the populations for three adsorption sites (atop, bridge and hollow) were also found to depend on the coverage.

Investigating the surface geometrical and electronic structures is indispensable for the understanding of the surface chemistry since these parameters significantly affect the surface properties and surface reactions as described above.

Magnetic thin films provide interesting properties such as significant enhancement of the magnetic moment compared to the bulk one. The magnetic properties of ultrathin films consisting of $3d$ transition metals, especially Fe, Co and Ni, are widely studied to find and understand such extraordinary magnetism. An Fe film (~3.6 ML) grown on Cu(100), for instance, has spin and orbital magnetic moments of 3.4 and 0.24 μ_B, respectively, which are greatly enhanced compared to bulk ones (2.3 and 0.09 μ_B, respectively) [16]. It should be noted that their ratio, m_l/m_s, also increases from 0.04 for the bulk to 0.07 for the thin film. A similar result has been reported for the Co thin films [17].

Another striking effect is a magnetic anisotropy. One of the most extensively investigated samples is Ni/Cu(100), where a sudden change of the magnetization easy axis has been observed at ~7 ML thickness [18–20]. Below 7 ML, the Ni film can be magnetized only in the direction parallel to the surface. The magnetization easy axis alters to the surface normal direction at ~ 7 ML, in spite that the parallel alignment is expected from the classical electromagnetic theory. This anomalous magnetic anisotropy has been explained by a strain of the Ni film. Since the Ni film initially grows pseudomorphically [21], the lattice constant for the thin Ni film is 2.5 % larger than that of the pure Ni crystal. Thus the film feels the strain and prefers to the perpendicular magnetization. The separation of orbital moment from the spin one is essential for the study on the magnetic anisotropy, because the orbital moment plays an important role in the appearance of

the magnetic anisotropy.

The magnetic properties of trilayers also have attracted much attention, because the interaction between the magnetic layers is the origin of the giant magnetoresistance (GMR) effects. In the case of Ni (1.6 ML) /Cu (3.5 ML) /Co (2.1 ML) trilayer grown on Cu(100), parallel alignment between the Ni and Co magnetic moments was observed, while the antiparallel one was found for Co (2.2 ML) /Cu (3.4 ML) /Co (3.6 ML) [22]. An oscillating interlayer coupling also has been observed for the Fe/Mn/Fe trilayer, where the magnetic coupling between two Fe layers changes as a function of the Mn thickness [23]. The element selectivity is indispensable for such studies, where the magnetic moment for each layer should be separately observed.

Effects of atomic and molecular adsorption on the magnetic film have been investigated since they are important for understanding the magnetic properties of practical materials. Adsorption of sulfur and oxygen on $3d$ transition metals provides typical examples. In many cases [24–26], such adsorption causes a magnetic "poisoning", where the surface magnetic moment is partially or completely "dead". It has been recently reported, however, that oxygen induces slight enhancement of the Fe magnetization [27,28]. Moreover, the magnetic anisotropy and magnetic coupling also can be affected by adsorption of atom and molecule. The rotation of the magnetization easy axis was found when H_2 adsorbs on Ni/Cu(100) [29], and the oxygen-induced changes in the magnetic direction of Mn were observed for Mn/Fe and Mn/Co [30,31]. Since the magnetic properties are drastically affected by the geometrical and electronic structures, it is important to investigate the magnetism, structure and electronic property of the adsorbates, as well as the substrates.

1-2. Comparison among experimental techniques for the surface investigation

1-2-1. Geometrical and electronic structures

Many experimental techniques are available for studying the surface geometrical structures. One of the most established methods is low energy electron diffraction (LEED) including the intensity versus voltage (I-V) curve measurements. Intensity of each diffraction spot is measured as a function of the incident electron energy, and compared with the calculated I-V curves for some model structures. The feasibility of the I-V LEED technique was significantly improved by the development of the Tensor LEED approximation [32,33]. Many parameters can be obtained concerning the surface structure for the adsorbate as well as the substrate. The essential limitation of the I-V LEED technique is, however, that it requires a long-range order. Since molecular-adsorption system often lacks the long-range order, I-V LEED method is not always effective for the study of surface chemistry.

Scanning tunneling microscope (STM) is a powerful tool to observe the surface morphology rather directly, though it has no element selectivity. For investigating the growth mode of the metal thin films, for instance, STM is likely to be the most suitable method since it provides direct imaging of the surface. The obtained surface structure is, however, not the atomic geometry itself, because STM probes the density of states. Therefore, when STM is applied to the molecular adsorption systems, the interpretation of the obtained image is difficult in many cases. The structural parameters of molecular adsorbates, such as orientation and bond length, are hard to be determined with STM.

Some vibrational techniques, *e.g.* infrared (IR) and electron energy loss spectroscopies (EELS), are also available for examining the surface structures. Since a vibration mode having a dipole moment change parallel to the surface is not observed (surface selection rule [34]), the symmetry of the adsorbate can be determined. The difficulty is, however, assignments of the observed peaks. In some cases wrong peak assignments have led to incorrect conclusions. Moreover, quantitative geometrical parameters such as bond length cannot be determined directly.

X-ray photoelectron diffraction (XPD) and EXAFS are powerful tools to determine the surface structure. These techniques utilize the core-level excitation and thus have the element selectivity. In the XPD measurements, the photoelectrons elastically scattered by surrounding atoms, as well as those emitted from the x-ray-absorbing atom, are collected by using an electron analyzer. Such photoelectrons contain the information about the local structure around the x-ray-absorbing atom, so that the geometrical parameters can be obtained. In the energy-scan mode XPD measurements [35], the intensity of the collected photoelectrons is recorded as a function of the incident photon energy, *i.e.* the wavelength of the photoelectrons. The interference condition between the scattered and directly emitted photoelectron wavefields changes depending on the photoelectron wavelength,

resulting in the modulation of the observed photoelectron intensity. On the other hand, EXAFS measures, in principle, the absorption coefficient as a function of photon energy, though some detection techniques are necessary to observe the x-ray absorption of the specimen on surfaces (see §2-1-3). The final state wave function for the x-ray absorption process is modulated by the interference between the wavefields of the emitted and scattered photoelectrons, so that the absorption spectra contain the geometrical information (§2-1-1). In both techniques (XPD and EXAFS), the measured spectra are usually compared with those obtained from calculations including multiscattering phenomena, in order to obtain the geometrical parameters.

Let me here discuss the advantages and disadvantages of XPD and EXAFS. Some differences arise from their data acquisition methods. Since XPD measures the intensities only for the photoelectrons, rather complicated procedure is necessary, which may make the obtained data unreliable. At each photon energy, one must record a short-range (~40 eV) electron energy spectra around the photoelectron peak, subtract a background and perform a peak fitting. On the contrary, the EXAFS spectra can be rather directly obtained by the absorption measurements. Of course the background subtraction from the obtained spectrum is, in addition, necessary in both the EXAFS and XPD techniques. Another difficulty of the XPD measurements is necessity of a detector with high sensitivity, since one must collect photoelectrons emitted in a narrow acceptance angle. This is, however, also an essential advantage of XPD, since more information can be extracted by altering the geometry of the detector alignment. XPD also has a possibility that the same kind of elements in different chemical states can be separately examined since the photoelectron energies for those states are different due to the chemical shift [36,37].

Another difference is due to their fitting procedure. Although many parameters can be determined from the analyses of the XPD data, such parameters are hard to be separately fitted. Therefore the parameter coupling often occurs [38]; an increase of the R factor induced by the change of a certain parameter can be compensated by altering the other one. This makes the errors of these parameters rather large. Moreover, more than one local minimums of the R factor are frequently found for the significantly different geometrical parameters. On the other hand, EXAFS has a great advantage; contributions from different atoms whose distances are different from each other can be separated by a Fourier filtering procedure [39] (see §2-1-1). This is because the bond distance directly affects the period of the EXAFS oscillation. Of course it is impossible to separate contributions from similarly distant atoms (difference of within ~0.5 Å). In such a case, the number of parameters in each fitting procedure increases and the reliability of the obtained parameters decreases.

In conclusion, combination of the XPD and EXAFS techniques seems to provide the detailed and reliable surface geometrical parameters. In the present study, I at first tried to establish the

surface EXAFS measurements because of its simplicity and reliability for the obtained parameters, leaving the XPD technique as a feature objective.

As regards the electronic structures, ultraviolet photoelectron spectroscopy (UPS) has been used to investigate the electronic properties of various solid surfaces. The occupied states lying under the Fermi level are observed with UPS and the electronic properties can be determined. Moreover, angle-resolved UPS (ARUPS) provides the information in the k space, which is essential to understand surface band structures. The symmetry of the surface adsorption system also can be determined by means of ARUPS. UPS has no element selectivity, however, and therefore a huge band structure arising from the metal substrates superimposes on the adsorbate-induced components. Thus the electron properties just below the Fermi level is rather hard to be obtained, in spite that such information about adsorbates is essential to understand the adsorbate-substrate interaction.

Complementary information, *i.e.* electronic structures of the unoccupied states, can be obtained by means of NEXAFS. Owing to the element selectivity of NEXAFS, the unoccupied adsorbate orbitals which directly interact with substrates can be clearly observed. Moreover, the orientation of the molecule can be determined from the polarization dependence of the NEXAFS spectra. Although the unoccupied states can be also investigated by inverse photoelectron spectroscopy, NEXAFS seems to superior because of its element selectivity and high sensitivity.

1-2-2. Magnetic properties

Quite high sensitivity is indispensable to investigate magnetic thin films, and element selectivity or quite high surface sensitivity is, in addition, necessary to obtain magnetic information about the adsorbates. Moreover, an ultra high vacuum system is required to prepare and investigate such samples. Although superconducting quantum interference devices (SQUID) and neutron scattering are, for instance, powerful tools to examine the magnetic properties, it is hard to apply them to the ultrathin (a few monolayer) magnetic films and surface adsorbates. The Magneto-optic Kerr effect (MOKE) has been widely used in order to study ultrathin ferromagnetic films, owing to its surface sensitivity. This technique is, however, not element specific because the Kerr effect arises from the shallow valence band. Moreover, no quantitative determination of the magnetic moment has been performed for such samples to my knowledge. Spin-polarized low-energy electron diffraction (SPLEED) also has been applied to the studies for surface magnetism. However, the long-range order is again necessary.

Another conventional method is spin-polarized photoelectron spectroscopy (SP-PES), where the exchange splitting of the ferromagnetic films can be directly observed by using a Mott detector.

Although some SP-PES studies have been reported on surface adsorbates on magnetic films [40,41], the spin polarization of the adsorbates around the Fermi level cannot be extracted because of the huge contribution of the magnetic films. Some similar techniques are available such as spin-polarized Auger electron and secondary electron spectroscopies. These methods are, however, based on rather complicated phenomena, and thus the quantitative information cannot be obtained.

XMCD has both the element selectivity and high sensitivity, so that a clear signal from even 0.02 ML (monolayer) Mn evaporated on a Fe film was observed [42]. Moreover, the spin and orbital magnetic moments can be determined separately by using "sum rules" [43,44] (see also §2-2-3). It seems that XMCD is one of the most suitable techniques for investigating surface magnetism of ultrathin films and adsorbates.

1-3. Necessity of a soft x-ray monochromator

1-3-1. Target of the investigation and required energy range

Light elements, *e.g.* carbon, nitrogen and oxygen, and 3*d* transition metals are the most fundamental in the surface chemistry. All the organic molecules consist of carbon, and many ones contain nitrogen and/or oxygen. Much has been studied for the adsorption of the light elements on the 3*d* transition metals, from the viewpoint of catalytic chemistry. Moreover, the 3*d* transition metals are fundamental and important components of many magnetic materials. Magnetic thin films and multilayers of such metals have been extensively investigated because of their interesting magnetic properties, as described in §1-1. In the present thesis, accordingly, I chose the light elements and the 3*d* transition metals as the targets of my investigations.

In order to apply the x-ray absorption techniques, the continuous x rays are required at the photon energy ranges around the absorption edges of the target elements. Figure 1-1 indicates the energies for *K* edges (corresponding to 1*s*) of the light elements and $L_{III,II}$ edges ($2p_{2/3}$ and $2p_{1/2}$) of the 3*d* transition metals. The required energy range is thus form ~200 to ~1500 eV, which is called soft x-ray region.

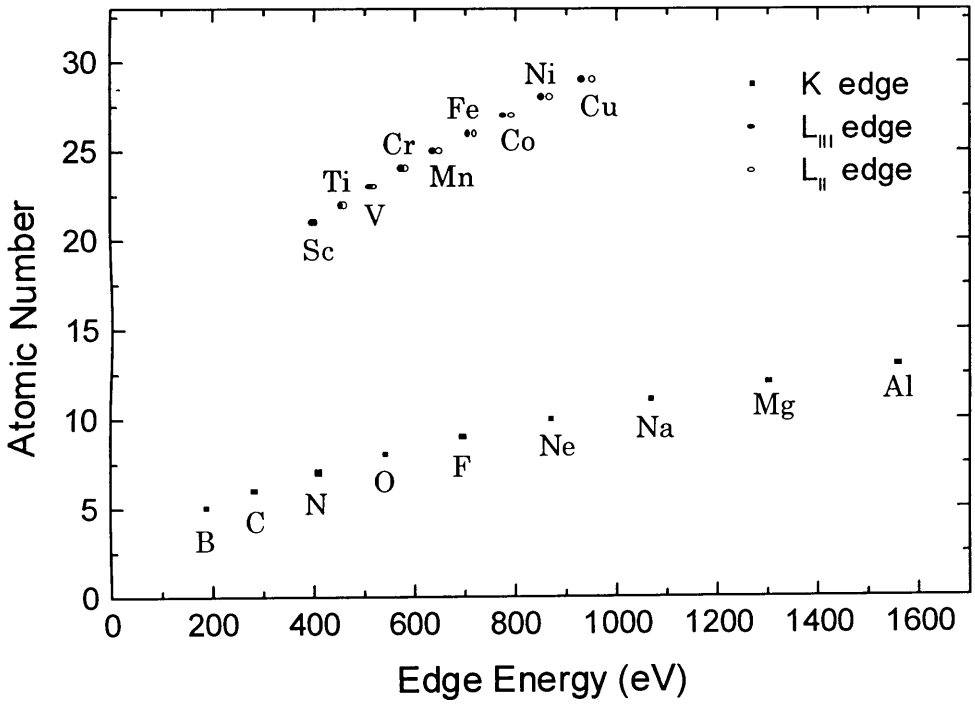

Fig. 1-1. Energies of *K* edges for light elements (square) and L_{III} and L_{II} edges for 3*d* transition metals (filled and open circles, respectively).

1-3-2. Soft x-ray monochromator

Although many XAFS studies have been carried out for heavier elements such as sulfur and chlorine in surface adsorbates, only some XAFS measurements including EXAFS have been reported for submonolayer amounts of light element adsorbates. Moreover, most of them deals with the saturation coverage (~0.5 ML) of the atomic adsorbate, and fewer data have been obtained for the molecular adsorbates. It is, however, essential to study the first-stage adsorption of the molecules in order to understand the interaction between the adsorbates and solid surfaces, which play important roles in the surface chemistry. The difficulty mainly arises from the lack of suitable soft x-ray monochromator, in spite that stable and intense soft x-rays are indispensable for the EXAFS measurements of the adsorbates. Moreover, a high resolution is also necessary to separately analyze some peaks appearing in the NEXAFS spectra.

On the other hand, a large number of XMCD measurements have been reported for magnetic thin films and multilayers. No XMCD data was, however, published for the light element adsorbates, though the investigation for the absorption of atoms and molecules on the magnetic thin films are quite important to understand the magnetic effects of such adsorbates. This is because the extremely intense and stable circularly polarized x rays are indispensable for the XMCD measurements of the surface adsorbates.

Although many attempts have been made to obtain the high-performance soft x-ray monochromator [45-49], few beamlines in the world were available for the EXAFS measurements for the surface adsorbates [39,48,49]. It should be noted that the EXAFS measurements require a flat photon flux distribution in a whole energy range (typically 500 eV wide). Although much more intense (sometimes more than 100 times larger) x rays can be obtained from an undulator source compared to the bending magnet, sharp structures in the photon flux curve from an undulator make the EXAFS measurements almost impossible. Accordingly, the development of a new soft x-ray monochromator with a bending magnet source is necessary in order to provide with intense and stable x rays over a wide energy range with high resolution.

1-4. Scope of this thesis

In the present study, I at first designed a soft x-ray monochromator in order to provide with intense and high resolution x rays, which are indispensable to carry out the XAFS, XMCD and XPD measurements. After the construction and improvements of the monochromator, I performed the XAFS measurements for the methoxy (CH_3O) species formed on Cu(111) and Ni(111) to investigate the geometrical and electronic structures. Since the adsorption structures for these systems have been determined by means of XPD, the previous results can be double-checked by the present study. I also tried to obtain further information about the electronic properties. Then I made an attempt to measure the XMCD spectra for molecular CO and atomic O adsorbed on Co thin films, as well as those for the Co films. A measuring system for the XMCD experiments was established and improved to collect reliable XMCD data for the small amounts of specimen. The information about the surface magnetism of the adsorbate was obtained and the magnetic and chemical interaction between the adsorbate and substrate was discussed.

In Chapter 2, theoretical outlines for XAFS and XMCD phenomena are given. Chapter 3 deals with the development of the soft x-ray monochromator. The XAFS measurements with the linearly polarized x rays for the methoxy species are described in Chapter 4. In Chapter 5, the XMCD measuring system with circularly polarized x rays are shown and the XMCD study of the molecular CO and atomic O adsorption is described.

References

[1] S. Bao, Ph. Hofmann, K.-M. Schindler, V. Fritzsche, A.M. Bradshaw, D.P. Woodruff, C. Casado and M.C. Asensio, Surf. Sci. **323**, 19 (1995).

[2] D.P. Woodruff, C.F. McConcille, A.L.D. Kilcoybe, T. Lindner, J. Somers, M. Surman, G. Paolucci and A.M. Bradshaw, Surf. Sci. **201**, 228 (1988).

[3] M. Sambi, G. Granozzi, M. Casarin, G.A. Rizzi, A. Vittadini, L.S. Caputi and G. Chiarello, Surf. Sci. **315**, 309 (1994).

[4] Th. Lindner, J. Somers, A.M. Bradshaw, A.L.D. Kilcoybe and D.P. Woodruff, Surf. Sci. **203**, 333 (1988).

[5] A. R. Kortan and R.L. Park, Phys. Rev. B **23**, 6340 (1981).

[6] J. Lauterbach, M. Wittmann and J. Küppers, Surf. Sci. **279**, 287 (1992).

[7] L. Becker, S. Aminpirooz, B. Hillert, M. Pedio, J. Haase and D. L. Adams, Phys. Rev. B **47**, 9710 (1993).

[8] M.E. Davila, M.C. Asensio, D.P. Woodruff, K.-M. Schindler, Ph. Hofmann, K.-U. Weiss, R. Dippel,

P. Gardner, V. Fritzsche, A.M. Bradshaw, J.C. Conesa and A.R. González-Elipe, Surf. Sci. **311**, 337 (1994).

[9] A. Grossmann, W. Erley and H. Ibach, Surf. Sci. **313**, 209 (1994).

[10] T. Yokoyama, S. Terada, S. Yagi, A. Imanishi, S. Takenaka, Y. Kitajima and T. Ohta, Surf. Sci. **324**, 25 (1995).

[11] N. Pangher, H.M. Köppe, J. Feldhaus and J. Hasse, Phys. Rev. Lett. **71**, 4365 (1993).

[12] J. L. Solomon, R.J. Madix, W. Wurth and J. Stöhr, J. Phys. Chem. **95**, 3687 (1991).

[13] Y.-M. Sun, D. Sloan, D.J. Alberas, M. Kovar, Z.-J. Sun and J.M. White, Surf. Sci. **319**, 34 (1994).

[14] Y. Kitajima, A. Imanishi, H. Aga, S. Yagi, Y. Takata, T. Yokoyama and T. Ohta, Photon Factory Activity Report **11**, 17(1993).

[15] H. Kondoh, C. Kodama and H. Nozoye, J. Phys. Chem. B **102**, 2310 (1998).

[16] J. Hunter Dunn, D. Arvanitis and N. Mårtensson, Phys. Rev. B **54**, 11157 (1996).

[17] M. Tischer, O. Hjortstam, D. Arvanitis, J. Hunter Dunn, F. May, K. Baberschke, J. Trygg, J. M. Willis, B. Johonsson and O. eriksson, Phys. Rev. Lett. **75**, 1602 (1995).

[18] W.L. O'Brien, T. Droubay and B. P. Tonner, Phys. Rev. B **54**, 9297 (1996).

[19] M. Farle, B. Mirwald-Schulz, A.N. Anisimov, W. Platow and K. Baberschke, Phys. Rev. B **55**, 3708 (1996).

[20] F. Huang, M.T. Kief, G.J. Mankey and R.F. Willis, Phys. Rev. B **49**, 3962 (1994).

[21] J. Zhang, Z.-L. Han, S. Varma and B.P. Tonner, Surf. Sci. **298**,351 (1993).

[22] F. May, M. Tischer, D. Arvanitis, J. Hunter Dunn, H. Henneken, H. Wende, R. Chauvistré and K. Baberschke, J. Phys. IV France, **7**, C2-389 (1997).

[23] Shi-shen Yan, R. Schreiber, F. Voges, C. Osthöver and P. Grünberg, Phys. Rev. B **59**, 11641 (1999).

[24] B. Sinkovic, P.D. Johnson, N.B. Brooks, A. Clarke and N.V. Smith, Phys. Rev. B **52**, 6955 (1995).

[25] F. May, M. Tischer, D. Arvanitis, M. Russo, J. Hunter Dunn, H. Henneken, H. Wende, R. Chauvistré, N. Mårtensson, and K. Baberschke, Phys. Rev. B **53**, 1076 (1996).

[26] P. Ferro, R.Moroni, M. Salvietti, M. Canepa and L. Mattera, Surf. Sci. **407**,212 (1998).

[27] S.R. Chubb and W.E. Pickett, Phys. Rev. Lett. **58**, 1248 (1987).

[28] R. Wu and A. J. Freeman, Phys. Rev. B **45**, 7532 (1992).

[29] R. Vollmer, Th. Gutjahr-Loser, J. Kirschner, S. van Dijken and B. Poelsema, Phys. Rev. B **60**, 6277 (1999).

[30] W. L. O'Brien and B.P. Tonner, Phys. Rev. B **58**, 3191 (1998).

[31] S. Andrieu, E. Foy, H. Fischer, M. Alnot, F. Chevrier, G. Krill and M. Piecuch, Phys. Rev. B **58**,

8210 (1998).

[32] P.J. Rous, J.B. Pendry, D.K. Saldin, K. Heinz, K. Muler and N. Bickel, Phys. Rev. Lett. **57**, 2951 (1986).

[33] P.J. Rous, Prog. Surf. Sci. **29**, 3 (1992).

[34] E. Evans and D.L. Mills, Phys. Rev. B **5**, 4126 (1972).

[35] D.P. Woodruff and A.M. Bradshaw, Rep. Prog. Phys. **57**, 1029 (1994).

[36] K.-U. Weiss, R. Dippel, K.-M. Schindler, P. Gardner, V. Fritzsche, and A.M. Bradshaw, A.L.D. Kilcoyne and D.P. Woodruff, Phys. Rev. Lett. **69**, 3196 (1992).

[37] K.-U. Weiss, R. Dippel, K.-M. Schindler, P. Gardner, V. Fritzsche, and A.M. Bradshaw, D.P. Woodruff and A.R. González-Elipe, Pys. Rev. Lett. **71**, 581 (1993).

[38] O. Schaff, G. Hess, V. Fernandez, K.-M. Schindler, A. Theobald, Ph. Hofmann, A.M. Bradshaw, V. Fritzsche, R. Davis, and D.P. Woodruff, J. Electron Spectrosc. Relat. Phenom. **75**, 117 (1995).

[39] *X-ray absorption: Principles, Applications, Techniques of EXAFS, SEXAFS and XANES*, edited by D.C. Koningsberger and R. Prins (Wiley, New York, 1988).

[40] W. Clemens, E. Vescovo, T. Kachel, C. Carbone, and W. Eberhardt, Pys. Rev. B **46**, 4198 (1992).

[41] M. Getzlaff, J. Bansmann, and G. Schönhense, J. Chem. Phys. **103**, 6691 (1995).

[42] O. Rader, W. Gudat, D. Schmitz, C. Carbone and W. Eberhardt, Pys. Rev. B **56**, 5053 (1997)

[43] B.T. Thole, P. Carra, F. Sette, and G. van der Laan, Phys. Rev. Lett. **68**, 1943 (1992).

[44] P. Carra, B.T. Thole, M. Altarelli, and X. Wang, Phys. Rev. Lett. **70**, 694 (1993).

[45] F.C. Brown, R.Z. Bachrach and N. Lien, Nucl. Instr. Methods **152**, 73 (1978).

[46] W. Eberhardt, G. Kalkoffen and C. Kunz, Nucl. Instr. Methods **152**, 81 (1978).

[47] C.T. Chen, Nucl. Instr. Methods A **256**, 595 (1987).

[48] E. Dietz, W. Braun, A.M. Bradshaw and R.L. Johnson, Nucl. Instr. Methods A **239**, 359 (1985).

[49] H. Petersen, Opt. Comm. **40**, 402 (1982).

Chapter 2

Principle of the x-ray absorption spectroscopies

2-1. XAFS spectroscopy

Figure 2-1 shows an example of the x-ray absorption spectrum. Subtle modulations of the absorption intensity can be seen at high-energy region, while prominent structures are observed around the threshold at ~2840 eV. The oscillations starting from a few tenth of eV above the threshold are called EXAFS (extended x-ray-absorption fine structure) and the sharp structures are named NEXAFS (near-edge x-ray-absorption fine structure). Although these fine structures have been known for more than half a century, a theoretical explanation of EXAFS was presented as late as in 1971 [1]. In the following sections, I describe the outline of the principle of EXAFS and NEXAFS.

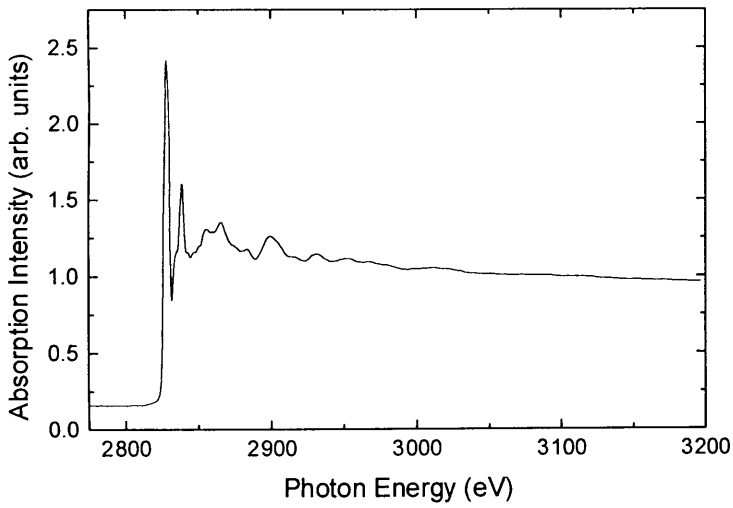

Fig. 2-1. An example of the XAFS spectrum taken at the chlorine K edge.

2-1-1. EXAFS

The origin of EXAFS is the interference of the outgoing photoelectron with the scattered one from the surrounding atoms, as schematically illustrated in Fig. 2-2. The photoelectron travels as a spherical wave with a wavelength $\lambda = 2\pi/k$, if no neighboring atoms exist. Here, k is the wavenumber of the photoelectron and can be written by

$$k = \sqrt{\frac{2m}{\hbar^2}(E - E_0)}, \tag{2-1}$$

where E is the incident photon energy and E_0 is the threshold energy of the absorption edge. In the presence of neighboring atoms, the outgoing photoelectron is backscattered from the surrounding atoms (scatterer). The scattered wave then interfere with the outgoing wave, resulting in a periodic modulation of the wavefield at the x-ray absorbing atom (absorber) as a function of the wavelength of the photoelectron. Thus the absorption coefficient, μ, oscillates with increasing incident photon energy. The EXAFS function, $\chi(k)$ is defined by

$$\chi(k) = \frac{\mu(k) - \mu_0(k)}{\mu_0(k)}, \tag{2-2}$$

where μ_0 is the background absorption. In principle, μ_0 is the absorption coefficient when no scattering by surrounding atoms occurs but the absorber is under the same environment as the actual one.

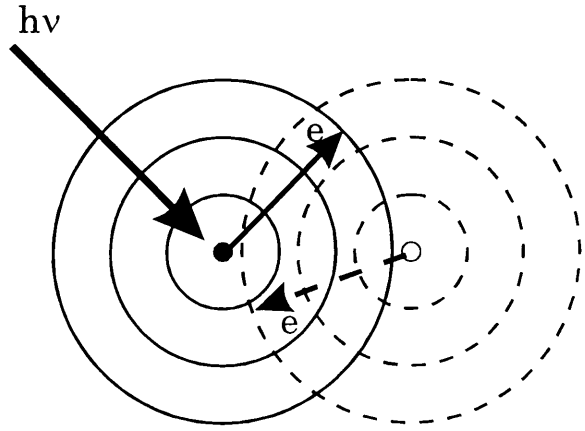

Fig. 2-2. Schematic view of the origin of EXAFS. Filled and open circles denote x-ray absorber and neighboring electron scatterer, respectively.

This simple picture of EXAFS has been formulated into the generally accepted short-range single-electron theory [2–5]. The EXAFS function can be written by

$$\chi(k) = \sum_j N_j S_0^2(k) F_j(k) \exp(-2\sigma_j^2 k^2) \exp(-2r_j / \lambda(k)) \frac{\sin(2kr_j + \phi_j(k))}{kr_j^2}, \tag{2-3}$$

where

N_j: coordination number of the neighboring atoms of jth type which are distant by r_j,

$F_j(k)$: backscattering amplitude from each of the neighboring atoms,

σ_j: Debye-Waller factor for thermal vibration and static disorder,

$\phi_j(k)$: total phase shift experienced by the photoelectron,

$\lambda(k)$: electron mean free path and

$S_0^2(k)$: amplitude reduction factor due to many-body effects such as shake up/off processes at the absorber atom.

It can be recognized that each EXAFS wave is determined by the back-scattering amplitude, $N_jF_j(k)$, modified by the sinusoidal oscillation, $\sin(2kr_j+\phi_j(k))$, and reduced by $S_0^2(k)$, $\exp(-2\sigma_j^2k^2)$, $\exp(-2r_j/\lambda)$ and $1/kr_j^2$. The phase shift contains contributions from both the absorber and scatterer:

$$\phi_{ab}^{l}(k) = \phi_a^l(k) + \phi_b(k) - l\pi, \tag{2-4}$$

where $l = 1$ for K and L_1 edges and $l = 2$ or 0 for $L_{III,II}$ edges, and ϕ_a^l and ϕ_b are the phase shifts of absorber and scatterer, respectively. Therefore, the period of the EXAFS oscillation is essentially determined by only the interatomic distance, if the scatterer is the same.

Owing to this comprehensive relationship between the bondlength and EXAFS oscillation period, a useful technique, *i.e.* Fourier filtering, is available for analyzing the EXAFS spectra [6]. Although the obtained EXAFS function contains many contributions from surrounding atoms, each components can be isolated by Fourier transforming the data, truncating it in r space and back transforming the truncated data into k space. Only the contributions from the atoms in the desired distance range can be isolated and fitted by rather small number of parameters. This decoupling of fitting parameters is quite helpful and makes the obtained parameters reliable.

When EXAFS is applied to a single crystal surface or an oriented sample by using linearly polarized x rays, the EXAFS equation must include the direction relation between the crystal axis and the electric field of x rays [6]. The coordination number N_j in eq. (2-3) is substituted by the effective coordination number, N_j^*, which is introduced by

$$N_j^* = 3\sum_{i=1}^{N_j}\cos^2\delta_i, \tag{2-5}$$

where δ_i is the angle between the electric field vector of the x rays and vector from the central atom to the ith atom in the jth shell. Note that eq. (2-5) is valed for K and L_1 edges. The information about the bond direction can be thus obtained from the polarization dependence of EXAFS. Being applied to the single crystal surfaces, the observed EXAFS is an average of all contributions from equivalent bonds. In the case of hollow site adsorption of an atom on a fcc(100) surface, for instance, four adsorbate-substrate bonds contribute to the EXAFS oscillation with the same period but different amplitudes. In addition, one must consider the "domain effect" for calculating the

effective coordination number. In the case of bridge-site adsorption on a fcc (100) surface, for example, two types of adsorption geometry coexist in the same probabilities, as shown in Fig. 2-3. One of them can be obtained by rotating the other geometry by 90° around the surface normal. The effective coordination number, N_j^*, is thus calculated as follows for the threefold or higher substrate symmetry, averaging over such equivalent bonds and domains:

$$N_j^* = P[1+\frac{1}{2}(3\cos^2\theta-1)(3\cos^2\alpha-1)+(1-P)\frac{3}{2}\sin^2\alpha$$
$$=1+\frac{1}{2}(3P\cos^2\theta-1)(3\cos^2\alpha-1), \quad (2\text{-}6)$$

where θ is the incidence angle of x rays (θ = 90° corresponds to the normal incidence; electric field vector, E, parallel to the surface), α is the polar angle of the bonds from the surface normal, and P is the linear polarization factor (P= 1 and 0.5 for the perfect and random polarization, respectively).

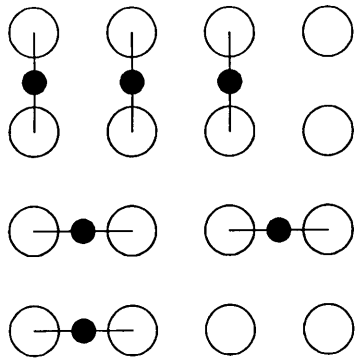

Fig. 2-3. Schematic drawing of two equivalent domains for a bridge-site adsorption on a fcc(100) surface. Open and filled circles denote the substrate and adsorbate atoms, respectively.

2-1-2. NEXAFS

Interpretation of the NEXAFS spectra with the scattering theory is difficult because of the complicated effects of multiple scattering events. Although the theoretical approach from the scattering calculation has been significantly advanced recently [7], a molecular orbital (MO) theory is more comprehensive and mostly adopted to understand the NEXAFS spectra [8]. Each peak appearing in the NEXAFS region is assigned to the transition from the core level to the empty MO such as π^* and σ^* orbitals. When NEXAFS is applied to a single crystal surface or an oriented sample by using linearly polarized x rays, the absorption intensity, I, is written by

$$I \propto |< f | \mathbf{e} \cdot \mathbf{p} | i >|^2 \propto |\mathbf{e} \cdot < f | \mathbf{p} | i >|^2 \propto \cos^2 \delta. \tag{2-7}$$

where **e** is a unit vector in the electric field direction, **p** is the momentum operator, $i>$ and $f>$ denote the initial and final states, respectively, and δ is the angle between the transition moment and the electric field vector. The polarization dependence of the NEXAFS spectra can be derived similarly for the surface with threefold of higher symmetries. By averaging the contributions of the MO's in all domains, the absorption intensity can be rewritten by

$$\begin{aligned} I &\propto P[\frac{1}{3}\{1+\frac{1}{2}(3\cos^2\theta-1)(3\cos^2\alpha-1)\}]+(1-P)\frac{1}{2}\sin^2\alpha \\ &= \frac{1}{3}+\frac{1}{6}(3P\cos^2\theta-1)(3\cos^2\alpha-1), \end{aligned} \tag{2-8}$$

where θ is the incidence angle of x rays and α is the polar angle of the transition moment from the surface normal.

Let me here describe about the effects of the vibration (wagging) of the molecules. When the molecule is, for instance, wagging around the surface normal as illustrated in Fig. 2-4, the observed NEXAFS spectra should be an average of "snap shots" for all molecules, since the time scale of the x-ray absorption is much faster than that of the vibration. At each moment, the tilt angles of the molecules are distributed in the wagging range with a certain probability distribution. Considering the domain effect, which is described above, the spectra can be simulated by averaging eq. (2-8) over whole wagging range of α, using a proper angle distribution. A simple simulation was performed, where the absorption intensity, I, is calculated by averaging the intensities for $\alpha = 0$, ± 2, ± 4, ± 6, ± 8 and $\pm 10°$. This corresponds to the $1s \rightarrow \sigma^*$ transition of a certain molecule whose bond is oriented around the surface normal as shown in Fig. 2-4. Note here that the intensities for $\alpha =$ +2 and –2° are, for instance, apparently the same. Figure 2-5 gives the simulated absorption intensity as a function of x-ray incident angle, together with those for $\alpha = 0$ and 10° (corresponding to the rigid molecule with polar angles of 0 and 10°, respectively). One may be surprised because the intensity curve for the wagging molecule is different from that for $\alpha = 0°$ (rigid molecule) in spite that the averaged orientation of the transition moment is 0° for both cases. This is, however, quite reasonable considering that, at the normal incidence ($\theta = 90°$) configuration, the intensity never goes to zero or negative values when $\alpha \neq 0°$ regardless of the sign of α, while it is zero for $\alpha = 0°$. The reason can be found in eq. (2-7), indicating that the intensity is not affected by the sign of δ.

On the other hand, another simulation was performed for the molecule whose transition moment (corresponding to the molecular axis in this example) is wagging between 10 and 20° from the surface normal as depicted in Fig. 2-6. Results of a similar simulation is shown in Fig. 2-7,

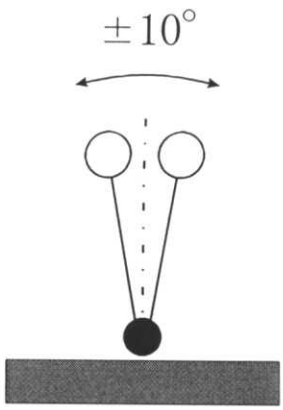

Fig. 2-4. Schematic image of a molecule wagging around the surface normal by ±10°.

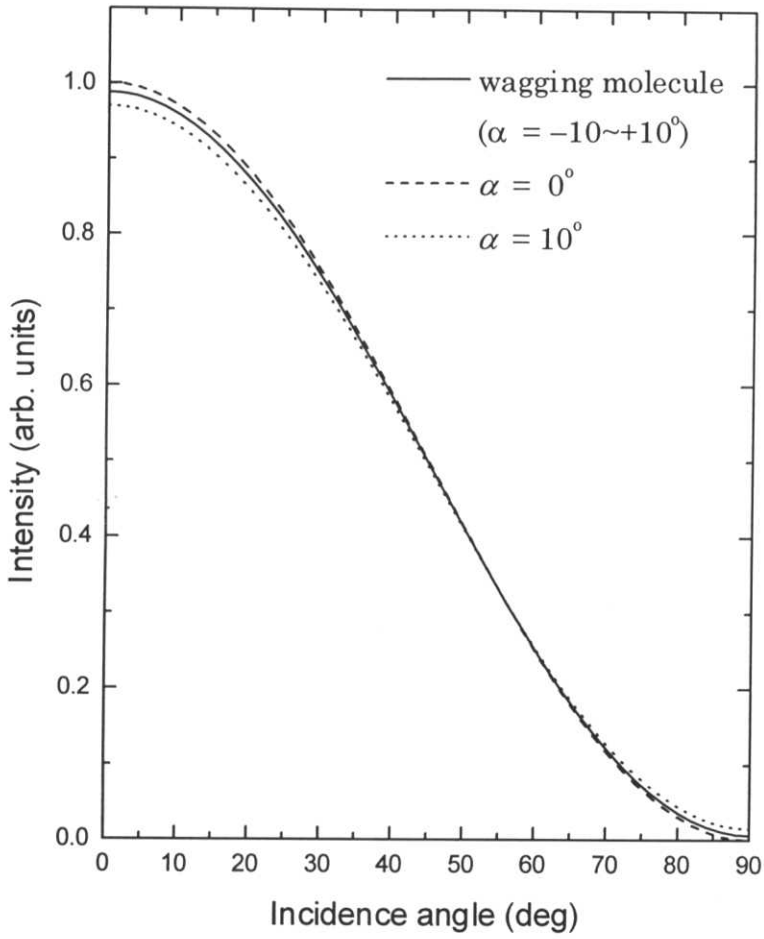

Fig. 2-5. Simulated polarization dependence of the NEXAFS spectra for the wagging molecule illustrated in Fig. 2-4. The transition moment is assumed to be oriented along the molecular axis.

where I is calculated by averaging the intensities for α = 10, 12, 14, 16, 18 and 20°, and compared with intensity curves for α = 10, 15 and 20°. In contrast to the above case (Fig. 2-5), the simulated intensity curve is close to that for the averaged orientation (α = 15°).

In conclusion, when the observed intensity curve indicates a non-zero value of α, it can be interpreted both as the inclined molecule (with or without wagging) and wagging one around the surface normal. On the contrary, the orientation of the molecule can be determined exclusively to be the surface normal direction, in principle, when the observed intensity curve matches to that calculated for α = 0°.

Another information obtained from the NEXAFS spectra is bond length of the molecule. The 1s→σ^* transition can be easily pictured as arising from a scattering process where the photoelectron wave is resonantly scattered back-and-force along the internuclear axis between the

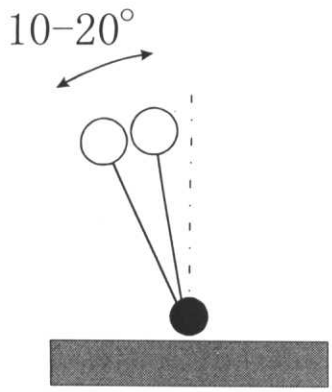

Fig. 2-6. Schematic image of a molecule wagging between 10 and 20° from the surface normal.

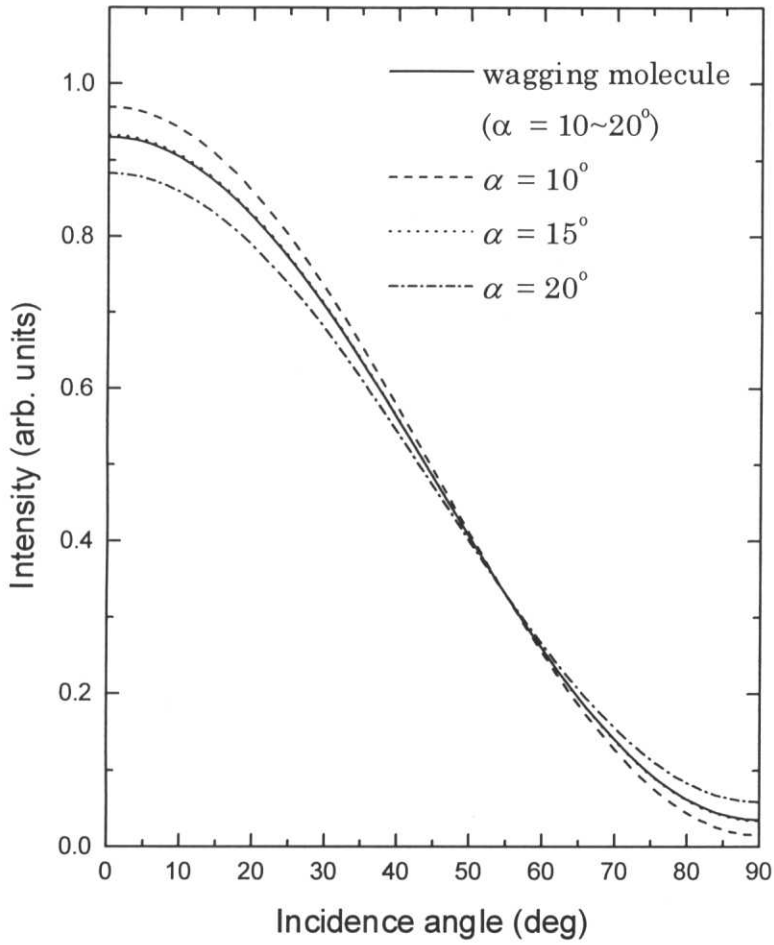

Fig. 2-7. Simulated polarization dependence of the NEXAFS spectra for the wagging molecule illustrated in Fig. 2-6.

absorber and neighboring atoms (σ^* shape resonance). This simple scattering picture suggests that the shape resonance energy should be related to the intramolecular distance. The peak energy and thus the photoelectron energy for such a resonance should be lower as the bondlength increases. Although no strict formula has been derived theoretically, empirical relations have been obtained experimentally [8]. The bondlength of a molecule can be therefore roughly estimated from the peak position of the $1s \rightarrow \sigma^*$ transition.

2-1-3. Detection methods for the XAFS measurements

The most conventional detection technique for the x-ray absorption measurements is transmission method, which can not be applied to the surface chemistry since the soft x rays cannot penetrate the thick substrate and the amount of the specimen is too small. The relaxation process

of the excited atom, *i.e.* emission of fluorescent x-rays, Auger electrons and secondary electrons, can be alternatively used to detect the x-ray absorption. Since the probability for the fluorescent process is quite small for the light elements such as C, N and O, electron yield methods are widely adopted for low-Z atoms [8]. Among some kinds of electron yield detection techniques, the Auger electron yield mode is superior to the other ones because of its high surface sensitivity. It requires, however, an electron energy analyzer with quite high sensitivity to obtain the reliable signals from submonolayer amounts of adsorbates. Moreover, the photoelectrons sometimes superimpose the Auger electrons during the energy scan.

A rather practical method is the partial electron yield mode, where the emitted electrons having the kinetic energies higher than a certain retarding voltage are collected. Since the low-energy electrons contain mainly the signals from the substrate, rather surface-sensitive spectra can be obtained with the partial electron yield mode. This technique requires no electron energy analyzer but only an electron collector and a grid for reject the low-energy electrons. Typical signal-to background (S/B) ratio with the partial electron yield detection is 1/5 for 0.5 ML amount of adsorbate.

2-2. XMCD spectroscopy

2-2-1. Definition of the circular polarization and the magnetic circular dichroism

In the case of circularly polarized x rays, the electric field vector rotates clockwise or counterclockwise as the wave travels. If the z axis of the Cartesian coordination system is defined so that it points into the x-ray propagation direction, the unit electric field for the right circularly polarized x rays can be expressed by [9]

$$\mathbf{e} = -\frac{1}{\sqrt{2}}(\mathbf{e}_x + i\mathbf{e}_y), \tag{2-9}$$

where $\mathbf{e}_x$ and $\mathbf{e}_y$ are unit vectors pointing into the directions of x and y axes, respectively. The unit electric field vector for the left circularly polarized x rays is similarly defined by

$$\mathbf{e} = \frac{1}{\sqrt{2}}(\mathbf{e}_x - i\mathbf{e}_y). \tag{2-10}$$

The right circular polarized light is also called "up spin" x rays or +1 helicity, while the left one corresponds to "down spin" and –1 helicity. It is well known that the x-ray absorption coefficient, μ, for a transition from an initial state $|i>$ to a final state $|f>$ is given by

$$\mu \propto |< f | \mathbf{e} \cdot \mathbf{r} | i >|^2, \tag{2-11}$$

where $\mathbf{r}$ is the electron-position vector which is expressed by

$$\mathbf{r} = x\mathbf{e}_x + y\mathbf{e}_y + z\mathbf{e}_z. \tag{2-12}$$

The absorption coefficients μ_+ and μ_- for the +1 and –1 helicity, respectively, can be therefore obtained from eqs. (2-9)–(2-12):

$$\mu_\pm \propto |< f | x \pm iy | i >|^2 . \tag{2-13}$$

The corresponding equation for the linearly polarized x rays with E vector along the z axis is given by

$$\mu_0 \propto |< f | z | i >|^2 . \tag{2-14}$$

These dipole operators for $\mu_\pm$ and μ_0 can be rewritten by using the well known spherical harmonics,

$Y_l^{m_l}(\theta,\phi)$. The dipole operators for the right ($P_1^{(1)}$), left ($P_1^{(-1)}$) and linearly ($P_1^{(0)}$) polarized x rays are expressed by

$$P_1^{(1)} = -\frac{1}{\sqrt{2}}(x+iy) = r\sqrt{\frac{4\pi}{3}}Y_1^1,$$
$$P_1^{(-1)} = \frac{1}{\sqrt{2}}(x-iy) = r\sqrt{\frac{4\pi}{3}}Y_1^{-1},$$
$$P_1^{(0)} = z = r\sqrt{\frac{4\pi}{3}}Y_1^0. \qquad (2\text{-}15)$$

Note here that the circularly polarized x rays *never* directly interact with electron spin, because no spin operators are included in the dipole operators.

When the sample is magnetized along the z axis, the electron spin should point either "up" ($+z$) direction or "down" ($-z$) one. The XMCD intensity, $\Delta\mu$, is defined by using the relative relationship between the photon and electron spins. In this paper I adopt the definition [9]

$$\Delta\mu = \mu_{\uparrow\uparrow} - \mu_{\uparrow\downarrow}, \qquad (2\text{-}16)$$

where $\mu_{\uparrow\uparrow}$ and $\mu_{\uparrow\downarrow}$ correspond to the parallel and antiparallel orientation between the photon spin and majority electron spin, respectively. From the following calculations, it can be understood that the same XMCD spectra are obtained with two different measurements technique; changing the helicity of the x rays leaving the sample magnetization unchanged, and altering the sample magnetization keeping the helicity of the x rays constant.

2-2-2. Interaction between the circularly polarized x rays and the sample magnetization

In the case of $L_{III,II}$-edge XMCD for the $3d$ transition metals and K-edge one for light elements, the transition from the angular momentum l to the state $l+1$ should be considered (l = 1 and 0 for $L_{III,II}$ and K edges, respectively). The dipole matrix elements appearing in eqs. (2-13) and (2-14) for such transitions from $|n,l,m_l>$ state are given by

$$<n',l+1,m_l+1|P_1^{(1)}|n,l,m_l> = -\sqrt{\frac{(l+m_l+2)(l+m_l+1)}{2(2l+3)(2l+1)}}R,$$
$$<n',l+1,m_l-1|P_{-1}^{(1)}|n,l,m_l> = -\sqrt{\frac{(l-m_l+2)(l-m_l+1)}{2(2l+3)(2l+1)}}R, \qquad (2\text{-}17)$$

and all other matrix elements are zero, *i.e.* only the transition where the magnetic quantum number, m_l, increases by 1 is allowed for the circularly polarized light with +1 helicity (right

circularly polarization or "up" photon spin), and *vice versa*. Here,

$$R = \int R^*_{nl}(r) R_{n'l'}(r) r^3 dr \tag{2-18}$$

is the radial matrix element. The initial state wave functions (including spin operator, α and β corresponding to $m_s = +1/2$ and $-1/2$, respectively), can be expressed as follows for $K(1s)$ and $L_{\mathrm{III,II}}$ ($2p_{3/2}$ and $2p_{1/2}$) edges:

$$\begin{aligned}
1s: \quad & Y_0^0 \alpha && (m_j = +1/2), \\
& Y_0^0 \beta && (m_j = -1/2), \\
2p_{3/2}: & Y_1^1 \alpha && (m_j = +3/2), \\
& \tfrac{1}{\sqrt{3}}(\sqrt{2} Y_1^0 \alpha + Y_1^1 \beta) && (m_j = +1/2), \\
& \tfrac{1}{\sqrt{3}}(Y_1^{-1} \alpha + \sqrt{2} Y_1^0 \beta) && (m_j = -1/2), \\
& Y_1^{-1} \beta && (m_j = -3/2), \\
2p_{1/2}: & \tfrac{1}{\sqrt{3}}(Y_1^0 \alpha - \sqrt{2} Y_1^1 \beta) && (m_j = +1/2), \\
& \tfrac{1}{\sqrt{3}}(\sqrt{2} Y_1^{-1} \alpha - Y_1^0 \beta) && (m_j = -1/2).
\end{aligned} \tag{2-19}$$

One can thus calculate the transition probabilities for $1s \rightarrow 2p$ and $2p \rightarrow 3d$ transitions for each helicity of the circularly polarized x rays, by expressing the final state wave function with the $|n,l,m_l,m_s>$ basis. In the case of $2p_{1/2}$ excitation, for instance, matrix elements for the +1 helicity ($\Delta m_l = +1$) are obtained as

$$\begin{aligned}
2p_{1/2}(m_j = +1/2) \rightarrow 3d(m_l = +1, m_s = +1/2): \quad & \tfrac{1}{3} |< 3,2,+1,+\tfrac{1}{2} | P_1^{(1)} | 2,1,0,+\tfrac{1}{2} >|^2 = \tfrac{1}{15} R^2, \\
\rightarrow 3d(m_l = +2, m_s = -1/2): \quad & \tfrac{2}{3} |< 3,2,+2,-\tfrac{1}{2} | P_1^{(1)} | 2,1,+1,-\tfrac{1}{2} >|^2 = \tfrac{4}{15} R^2, \\
2p_{1/2}(m_j = -1/2) \rightarrow 3d(m_l = 0, m_s = +1/2): \quad & \tfrac{2}{3} |< 3,2,0,+\tfrac{1}{2} | P_1^{(1)} | 2,1,-1,+\tfrac{1}{2} >|^2 = \tfrac{2}{45} R^2, \\
\rightarrow 3d(m_l = +1, m_s = -1/2): \quad & \tfrac{1}{3} |< 3,2,+1,-\tfrac{1}{2} | P_1^{(1)} | 2,1,0,-\tfrac{1}{2} >|^2 = \tfrac{1}{15} R^2,
\end{aligned} \tag{2-20}$$

and all other matrix elements are zero. Similar calculations for the -1 helicity ($\Delta m_l = -1$) yield

$$\begin{aligned}
2p_{1/2}(m_j = +1/2) \rightarrow 3d(m_l = -1, m_s = +1/2): \quad & \tfrac{1}{3} |< 3,2,-1,+\tfrac{1}{2} | P_1^{(-1)} | 2,1,0,+\tfrac{1}{2} >|^2 = \tfrac{1}{15} R^2, \\
\rightarrow 3d(m_l = 0, m_s = -1/2): \quad & \tfrac{2}{3} |< 3,2,0,-\tfrac{1}{2} | P_1^{(-1)} | 2,1,+1,-\tfrac{1}{2} >|^2 = \tfrac{2}{45} R^2, \\
2p_{1/2}(m_j = -1/2) \rightarrow 3d(m_l = -2, m_s = +1/2): \quad & \tfrac{2}{3} |< 3,2,-2,+\tfrac{1}{2} | P_1^{(-1)} | 2,1,-1,+\tfrac{1}{2} >|^2 = \tfrac{4}{15} R^2, \\
\rightarrow 3d(m_l = -1, m_s = -1/2): \quad & \tfrac{1}{3} |< 3,2,-1,-\tfrac{1}{2} | P_1^{(-1)} | 2,1,0,-\tfrac{1}{2} >|^2 = \tfrac{1}{15} R^2,
\end{aligned} \tag{2-21}$$

and again all other matrix elements are zero. It can be recognized that, as regards $2p_{1/2}$ excitation,

the total transition probability of the "up" (α) spin for the +1 helicity is smaller than that for the –1 helicity (their ratio is 1/9:1/3), and the opposite is true for the "down" (β) spin. Thus the circularly polarized x rays couple to the electron spin via the spin-orbit interaction in the $2p$ levels.

Figure 2-8 schematically shows the calculated relative transition probabilities for the K- and $L_{III,II}$-edge excitations. It should be remarked that, for the K-edge excitation, transition probability of the "up" electron spin is identical to the " down" one regardless of the photon helicity, indicating that no information about the electron spin can be obtained. This is due to the lack of the spin-orbit splitting in the K ($1s$) shell. In the case of the $2p_{3/2}$ excitation, in contrast, the transition probability of the "up" electron spin for the +1 helicity is larger than that for the "down" one (25:15), while the "down" one is more excited by the +1 helicity light from the $2p_{1/2}$ level.

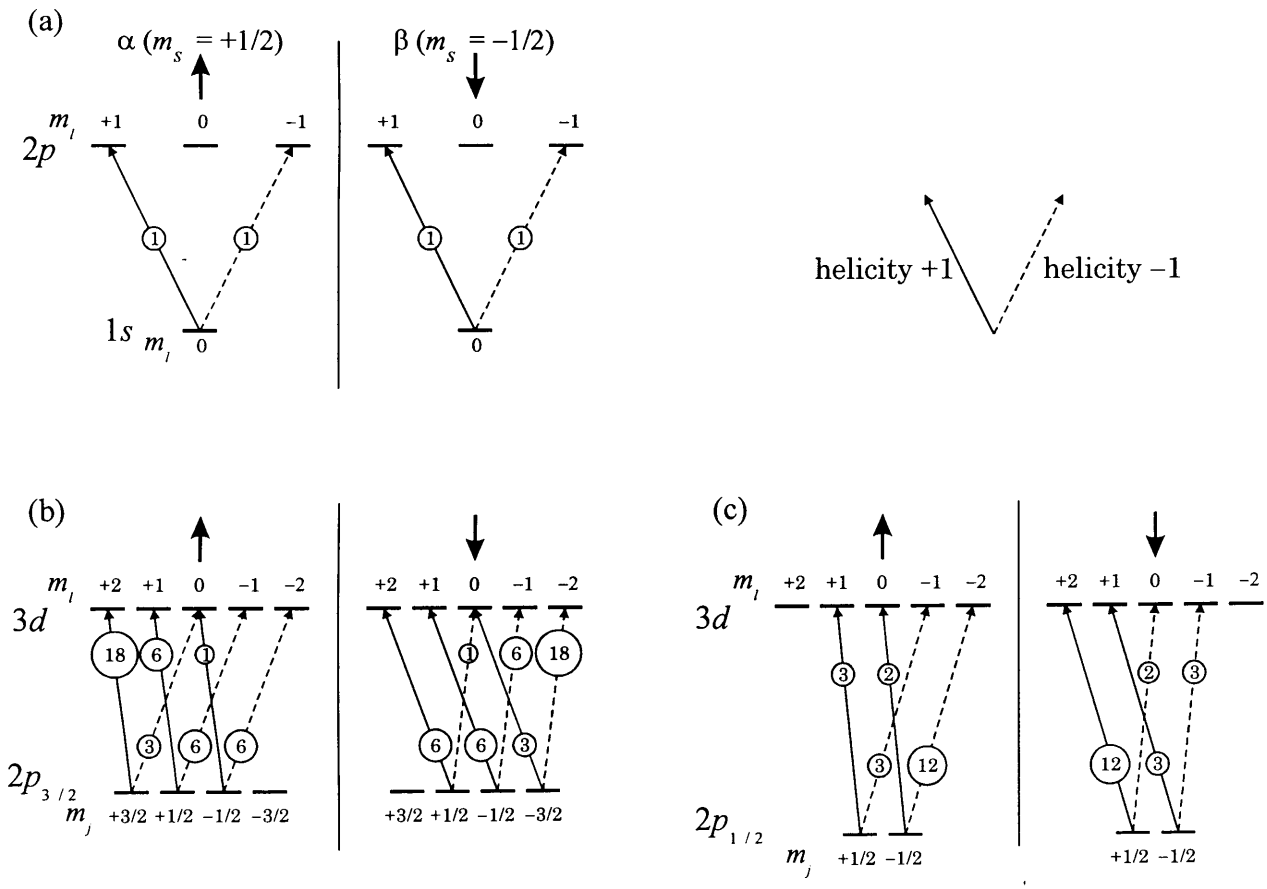

Fig. 2-8. Relative transition probabilities (numbers on the arrows) for the circularly polarized x rays at the (a) K, (b) L_{III} and (c) L_{II} edges. Solid and dashed lines indicate the helicity of +1 and –1, respectively.

2-2-3. Relation between the XMCD signal and the sample magnetic moment

Although the origin of the XMCD effects can be understood qualitatively as described in the previous section, quantitative relationship between the magnetic moments and the XMCD spectra are necessary. In this section I show some simple calculations in order to obtain such a relationship. Hereafter, it is assumed that the sample is magnetized in the $+z$ direction, and thus the "down" (β) spin is majority. Accordingly the absorption coefficient $\mu_{\uparrow\uparrow}$ means the excitation by the "down" photon spin (−1 helicity).

a. *K*-edge absorption

The final states for the *K*-edge absorption are $2p$ levels. Here I define the electron hole number, $h_\alpha^{m_l}$ and $h_\beta^{m_l}$ (corresponding to the α and β spins, respectively), for each $2p$ subshell with magnetic quantum number of m_l. By using the transition probabilities indicated in Fig. 2-8, the relative absorption intensities, $\mu_{\uparrow\uparrow}$ and $\mu_{\uparrow\downarrow}$ can be written by

$$\begin{aligned}
&\mu_{\uparrow\uparrow} = h_\alpha^{-1} + h_\beta^{-1}, \\
&\mu_{\uparrow\downarrow} = h_\alpha^{+1} + h_\beta^{+1}. \\
&\therefore \Delta\mu = \mu_{\uparrow\uparrow} - \mu_{\uparrow\downarrow} = (h_\alpha^{-1} + h_\beta^{-1}) - (h_\alpha^{+1} + h_\beta^{+1}).
\end{aligned} \tag{2-22}$$

Accordingly, if the occupancy for the $m_l = +1$ subshell is different from that for $m_l = -1$ as shown in Fig. 2-9(b), non-zero XMCD signal is observed, which is also given schematically in Fig. 2-9. Since the total orbital angular momentum in the p levels, $\langle L_z \rangle_p$, is expressed by

$$\begin{aligned}
\langle L_z \rangle_p &= [(1 - h_\alpha^{+1}) + (1 - h_\beta^{+1})] - [(1 - h_\alpha^{-1}) + (1 - h_\beta^{-1})] \\
&= -(h_\alpha^{+1} + h_\beta^{+1}) + (h_\alpha^{-1} + h_\beta^{-1}),
\end{aligned} \tag{2-23}$$

the orbital angular momentum of the sample is proportional to the XMCD intensity. Moreover, from a similar calculation of the dipole matrix element for the linearly polarized x rays appearing in eq. (2-14), the relative absorption intensity for the linearly polarized x rays, μ_0, can be given by

$$\mu_0 = h_\alpha^0 + h_\beta^0. \tag{2-24}$$

From eqs. (2-22)–(2-24), the relationship between the normalized XMCD intensity and the total orbital angular momentum of the sample can be obtained;

$$\frac{\mu_{\uparrow\uparrow} - \mu_{\uparrow\downarrow}}{\mu_{\uparrow\uparrow} + \mu_{\uparrow\downarrow} + \mu_0} = \frac{< L_z >_p}{n_h(p)}$$

$$\therefore < L_z >_p = n_h(p) \frac{\Delta\mu}{\mu_{\uparrow\uparrow} + \mu_{\uparrow\downarrow} + \mu_0}, \tag{2-25}$$

where

$$n_h(p) = h_\alpha^{-1} + h_\alpha^0 + h_\alpha^{+1} + h_\beta^{-1} + h_\beta^0 + h_\beta^{+1} \tag{2-26}$$

is the total hole number of the p levels. Unfortunately, the total spin moment of the $2p$ levels cannot be obtained from the XMCD spectra, which is apparent from eq. (2-22).

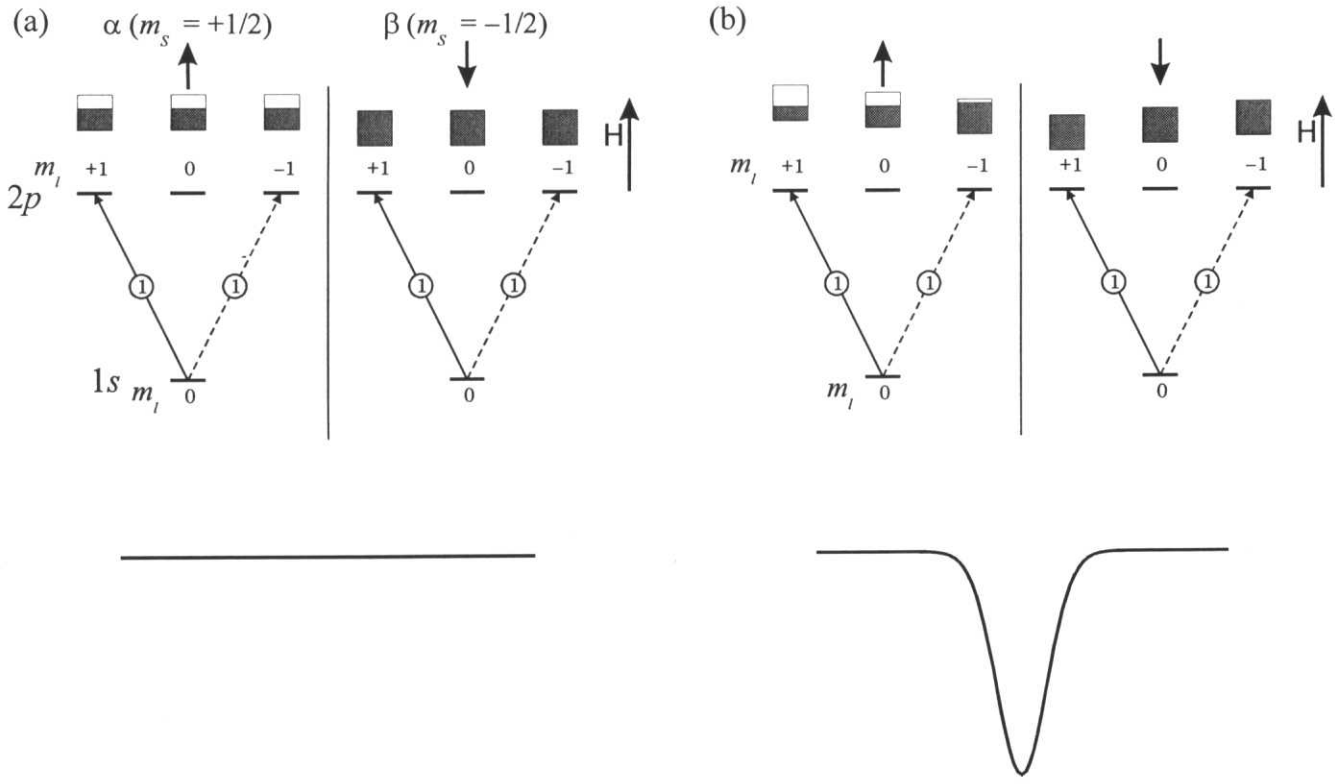

Fig. 2-9. Schematic diagram for the origin of the K-edge XMCD (top) and expected XMCD spectra, $\Delta\mu = \mu_{\uparrow\uparrow} - \mu_{\uparrow\downarrow}$, (bottom), (a) without and (b) with the spin-orbit splitting in the $2p$ shell. The sample is assumed to be magnetized in the $+z$ direction. Solid and dashed arrows indicate the +1 and –1 helicity, respectively, and numbers on them give the transition probabilities.

b. $L_{III,II}$-edge absorption

From similar calculations, the relative absorption intensities, $\mu_{\uparrow\uparrow}$ and $\mu_{\uparrow\downarrow}$ for the $L_{III,II}$ edges can be obtained;

$L_{II}(2p_{1/2})$ excitation :

$$\mu_{\uparrow\uparrow}(L_{II}) = 3h_{\alpha}^{-1} + 12h_{\alpha}^{-2} + 2h_{\beta}^{0} + 3h_{\beta}^{-1},$$
$$\mu_{\uparrow\downarrow}(L_{II}) = 3h_{\alpha}^{+1} + 2h_{\alpha}^{0} + 12h_{\beta}^{+2} + 3h_{\beta}^{+1},$$

$L_{III}(2p_{3/2})$ excitation :

$$\mu_{\uparrow\uparrow}(L_{III}) = 3h_{\alpha}^{0} + 6h_{\alpha}^{-1} + 6h_{\alpha}^{-2} + h_{\beta}^{0} + 6h_{\beta}^{-1} + 18h_{\beta}^{-2},$$
$$\mu_{\uparrow\downarrow}(L_{III}) = 18h_{\alpha}^{+2} + 6h_{\alpha}^{+1} + h_{\alpha}^{0} + 6h_{\beta}^{+2} + 6h_{\beta}^{+1} + 3h_{\beta}^{0}, \qquad (2\text{-}27)$$

where the hole numbers are defined for the $3d$ levels. In the simple case where the occupancy of the $3d$ levels is independent of the magnetic quantum number, m_l, as illustrated in Fig. 2-10(a), the XMCD signal can be related to the spin asymmetry as follows:

$$\begin{aligned}\mu_{\uparrow\uparrow}(L_{II}) - \mu_{\uparrow\downarrow}(L_{II}) &= 3h_{\alpha}^{-1} + 12h_{\alpha}^{-2} + 2h_{\beta}^{0} + 3h_{\beta}^{-1} - (3h_{\alpha}^{+1} + 2h_{\alpha}^{0} + 12h_{\beta}^{+2} + 3h_{\beta}^{+1}) \\ &= 2(h_{\alpha} - h_{\beta}), \\ \mu_{\uparrow\uparrow}(L_{III}) - \mu_{\uparrow\downarrow}(L_{III}) &= 3h_{\alpha}^{0} + 6h_{\alpha}^{-1} + 6h_{\alpha}^{-2} + h_{\beta}^{0} + 6h_{\beta}^{-1} + 18h_{\beta}^{-2} \\ &\quad - (18h_{\alpha}^{+2} + 6h_{\alpha}^{+1} + h_{\alpha}^{0} + 6h_{\beta}^{+2} + 6h_{\beta}^{+1} + 3h_{\beta}^{0}) \\ &= -2(h_{\alpha} - h_{\beta}),\end{aligned} \qquad (2\text{-}28)$$

where

$$h_{\alpha} = h_{\alpha}^{+2} + h_{\alpha}^{+1} + h_{\alpha}^{0} + h_{\alpha}^{-2} + h_{\alpha}^{-2},$$
$$h_{\beta} = h_{\beta}^{+2} + h_{\beta}^{+1} + h_{\beta}^{0} + h_{\beta}^{-1} + h_{\beta}^{-2}. \qquad (2\text{-}29)$$

Since the β spin is majority ($h_{\alpha} > h_{\beta}$), a positive XMCD signal should be observed at the L_{II} edge, while a negative one is expected at the L_{III} edge. Note here that the absolute XMCD intensities are the same for both edges.

In the practical case, where the $3d$ levels have spin-orbit splitting, the XMCD signal becomes asymmetric as shown in Fig. 2-10(b). Although the spin moment cannot be related to the XMCD signal with a simple equation, the total orbital angular momentum is directly related to the sum of the XMCD signals over the L_{III} and L_{II} edges. The obtained equation is

$$\begin{aligned}\Delta\mu(L_{\mathrm{III}})+\Delta\mu(L_{\mathrm{II}}) &= [\mu_{\uparrow\uparrow}(L_{\mathrm{III}})-\mu_{\uparrow\downarrow}(L_{\mathrm{III}})]+[\mu_{\uparrow\uparrow}(L_{\mathrm{II}})-\mu_{\uparrow\downarrow}(L_{\mathrm{II}})] \\ &= (-18h_{\alpha}^{+2}-9h_{\alpha}^{+1}+9h_{\alpha}^{-1}+18h_{\alpha}^{-2}-18h_{\beta}^{+2}-9h_{\beta}^{+1}+9h_{\beta}^{-1}+18h_{\beta}^{-2}) \\ &= -9[2(h_{\alpha}^{+2}+h_{\beta}^{+2})+(h_{\alpha}^{+1}+h_{\beta}^{+1})-(h_{\alpha}^{-1}+h_{\beta}^{-1})-2(h_{\alpha}^{-2}+h_{\beta}^{-2})] \\ &= 9<L_z>_d \end{aligned} \tag{2-30}$$

where $<L_z>_d$ is the total orbital angular momentum in the d levels. In addition, the sum of $\mu_{\uparrow\uparrow}$, $\mu_{\uparrow\downarrow}$ and μ_0 over the L_{III} and L_{II} edges is expressed by

$$\begin{aligned}&[\mu_{\uparrow\uparrow}(L_{\mathrm{III}})+\mu_{\uparrow\downarrow}(L_{\mathrm{III}})]+[\mu_{\uparrow\uparrow}(L_{\mathrm{II}})+\mu_{\uparrow\downarrow}(L_{\mathrm{II}})]+[\mu_0(L_{\mathrm{II}})+\mu_0(L_{\mathrm{II}})] \\ &= 18[(h_{\alpha}^{+2}+h_{\alpha}^{+1}+h_{\alpha}^{0}+h_{\alpha}^{-1}+h_{\alpha}^{-2})+(h_{\beta}^{+2}+h_{\beta}^{+1}+h_{\beta}^{0}+h_{\beta}^{-1}+h_{\beta}^{-2})] \\ &= 18n_h(d), \end{aligned} \tag{2-31}$$

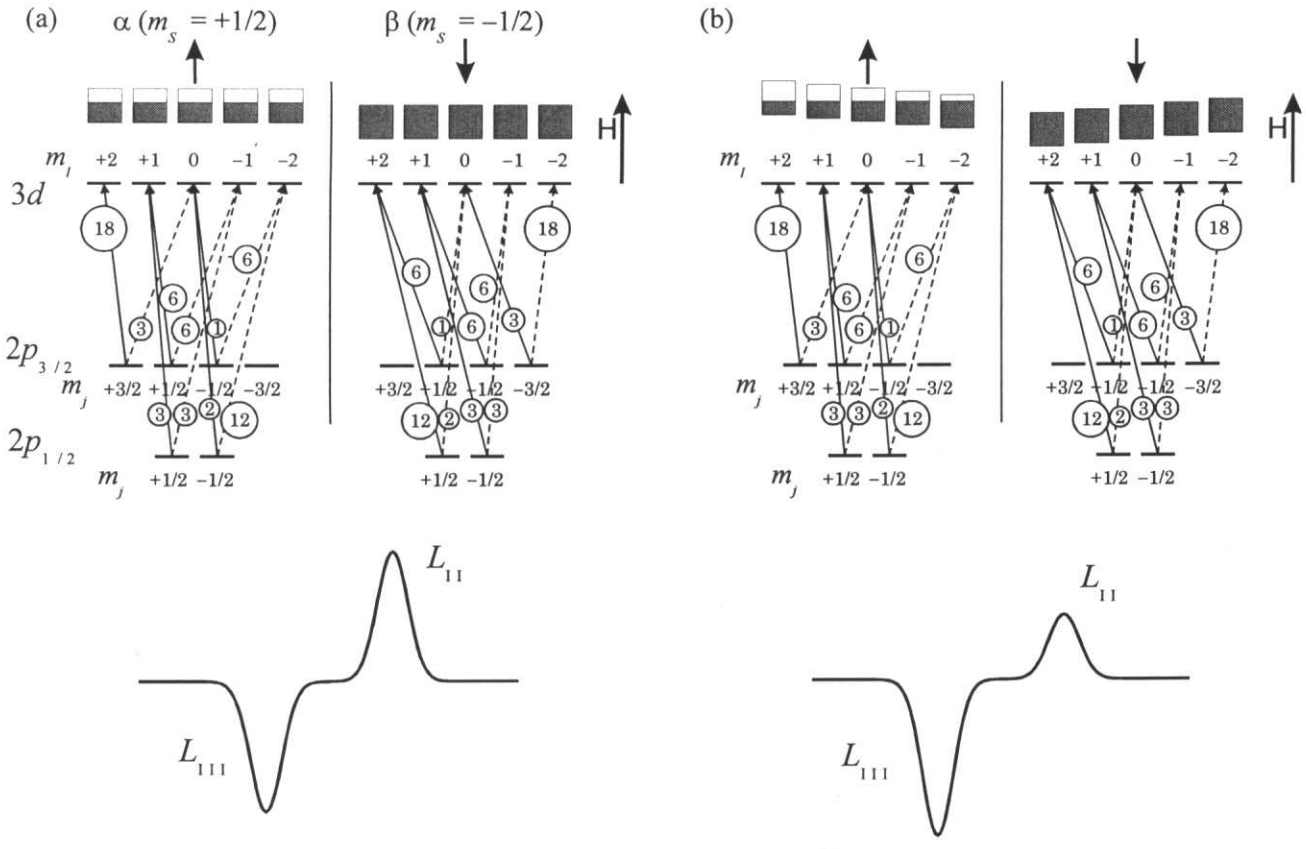

Fig. 2-10. Schematic diagram for the origin of the $L_{\mathrm{III,II}}$-edge XMCD (top) and expected XMCD spectra, $\Delta\mu = \mu_{\uparrow\uparrow} - \mu_{\uparrow\downarrow}$, (bottom), (a) without and (b) with the spin-orbit splitting in the $3d$ shell. The sample is assumed to be magnetized in the $+z$ direction. Numbers on the solid and dashed arrows indicate the transition probabilities for the +1 and –1 helicity, respectively.

where $n_h(d)$ is the total hole number of the d levels. From eqs. (2-30) and (2-31), the relationship between the normalized XMCD intensity and the total orbital angular momentum of the sample can be obtained;

$$\frac{(\mu_{\uparrow\uparrow} - \mu_{\uparrow\downarrow})_{L_{III}+L_{II}}}{(\mu_{\uparrow\uparrow} + \mu_{\uparrow\downarrow} + \mu_0)_{L_{III}+L_{II}}} = \frac{1}{2}\frac{< L_z >_d}{n_h(d)}$$

$$\therefore < L_z >_d = n_h(d)\frac{2(\Delta\mu)_{L_{III}+L_{II}}}{(\mu_{\uparrow\uparrow} + \mu_{\uparrow\downarrow} + \mu_0)_{L_{III}+L_{II}}}. \qquad (2\text{-}32)$$

c. Sum rules

The general rules have been derived which relate the XMCD spectra to the magnetic moments of samples [10,11]. The derived equations are called "sum rules" and widely used in order to analyze the XMCD spectra. The sum rules are given by

$$\frac{\int_{j_+ + j_-} d\omega(\mu_+ - \mu_-)}{\int_{j_+ + j_-} d\omega(\mu_+ + \mu_- + \mu_0)} = \frac{1}{2}\frac{l(l+1) + 2 - c(c+1)}{l(l+1)(4l + 2 - n)} < L_z >,$$

$$\frac{\int_{j_+} d\omega(\mu_+ - \mu_-) - \frac{c+1}{c}\int_{j_-} d\omega(\mu_+ - \mu_-)}{\int_{j_+ + j_-} d\omega(\mu_+ + \mu_- + \mu_0)} = \frac{l(l+1) - 2 - c(c+1)}{3c(4l + 2 - n)} < S_z >$$

$$+ \frac{l(l+1)[l(l+1) + 2c(c+1) + 4] - 3(c-1)^2(c+2)^2}{6lc(l+1)(4l + 2 - n)} < T_z >, \qquad (2\text{-}33)$$

where n is the number of the electrons in the excited shell, and c and l are the azimuthal quantum numbers for the initial and final states, respectively. The additional term $< T_z >$ is called magnetic dipole, which is defined by

$$\mathbf{T} = \sum_i \mathbf{s}_i - 3\mathbf{r}_i(\mathbf{r}_i \cdot \mathbf{s}_i)/r_i^2. \qquad (2\text{-}34)$$

Note here that the spin angular momentum, $< S_z >$, cannot be obtained for the K-edge absorption ($c = 0$ and $l = 1$) because the coefficient for $< S_z >$ in eq. (2-33) has no value for $c = 0$ and $l = 1$. This is consistent with the conclusion described above. The sum rule for $< L_z >$ is, on the other hand, identical to eqs. (2-25) and (2-32). As regards the K-edge orbital sum rule, the consistent result has been also obtained independently [12].

References

[1] D.E. Sayers, E.A. Stern and F.W. Lytle, Phys. Rev. Lett. **27**, 1204 (1971).

[2] E.A. Stern, Phys. Rev. B **10**, 317 (1974).

[3] E.A. Stern, D.E. Sayers and F. W. Lytle, Phys. Rev. B **11**, 4836 (1975).

[4] P.A. Lee and G. Beni, Phys. Rev. B **15**, 2862 (1977).

[5] P.A. Lee and J.B. Pendry, Phys. Rev. B **11**, 2795 (1975).

[6] *X-ray absorption: Principles, Applications, Techniques of EXAFS, SEXAFS and XANES*, edited by D.C. Koningsberger and R. Prins (Wiley, New York, 1988).

[7] A.L. Ankudinov, B. Ravel, J.J. Rehr and S.D. Conradson, Phys. Rev. B **58**, 7565 (1998).

[8] J. Sthör, *NEXAFS Spectroscopy* (Springer, Berlin, 1992).

[9] J. Sthör and Y. Wu, in *New Directions in Research with Third-Generation Soft X-Ray Synchrotron Radiation Sources,* edited by A.C. Schiachter and F.J. Wuilleumier (Kluwer Academic, Netherland, 1994).

[10] B.T. Thole, P. Carra, F. Sette, and G. van der Laan, Phys. Rev. Lett. **68**, 1943 (1992).

[11] P. Carra, B.T. Thole, M. Altarelli, and X. Wang, Phys. Rev. Lett. **70**, 694 (1993).

[12] J. Igarashi and K. Hirai, Phys. Rev. B **50**, 17820 (1994).

Chapter 3

Development of a soft x-ray monochromator

In this chapter, I describe the design, construction and commissioning of a soft x-ray beamline BL-11A at the Photon Factory in High Energy Accelerator Research Organization. A Monk-Gillieson mounting monochromator with a Varied-Line-Spacing (VLS) plane grating was designed following a new concept. In order to obtain pure x-rays with high resolution, a holographic VLS grating was fabricated with aspheric wavefront recording and a novel harmonic-rejection double-mirror system was developed to eliminate the higher diffraction orders. Effects of errors in the recording parameters are also estimated, and the adjustment procedures to compensate for them were proposed. Mechanically ruled and holographic 800-*l*/mm VLS gratings were tested in the new monochromator and the resolving power of ~5000 was obtained in the vicinity of nitrogen *K* edge. It was found that the holographic grating has a higher reflectivity with a lower scattered light level, and that the higher spectral orders are efficiently removed with the double-mirror system.

3-1. Introduction

The performance of a monochromator is determined by the intensity, stability and purity of the monochromatized x rays, as well as the energy resolution. In order to achieve the high performance, many types of grazing incidence monochromators in the soft x-ray region have been developed for the last decades [1–4]. Among them, much attention has been paid to the monochromator equipped with a Varied-Line-Spacing (VLS) grating, whose groove spacing is not uniform but varied as a function of the position on the grating [5–13]. Hettrick *et al.* [5,6] have shown that the Monk-Gillieson mounting monochromator (Fig. 3-1), consisting of a plane VLS grating and a focusing spherical mirror, can provide a stable monochromatic beam with a high resolving power. The most important benefit of this mounting is its simple scanning mechanism, requiring no linear translation of any optical element but only rotation of the grating. Although the scanning mechanism itself is quite simple, its performance mostly depends on the quality of the VLS grating. Efforts should be made, therefore, both in the design and fabrication of the grating to achieve a high performance. One must determine the variation of the groove density (called groove parameters) of the grating properly, and must realize the optimized groove parameters in the manufacturing process.

As for the design of the VLS grating, I introduced a new concept for the optimization of the groove parameter. In the previous studies on the design of the Hettrick-type monochromator [8,9],

they assumed that the grating is illuminated by perfectly focused rays, and considered the grating alone in the optimization process. It is not satisfactory since the rays cannot be focused perfectly by a spherical mirror because of the aberration. In the present paper I proposed an optimization procedure including both a focusing spherical mirror and a VLS grating. It has been shown that the aberrations arising from the spherical mirror are significantly reduced by using the new design concept, compared with the previous methods [5,6,8,9].

Also for the manufacturing of the grating, a new method was developed in order to obtain a high reflectivity and to suppress the scattered light. There are two major techniques to fabricate gratings in the soft x-ray region, *i.e.* mechanical ruling and holographic recording. In the latter one, interference patterns arising from two paths of light are recorded as the grooves of the grating. To the decades of experiences at the Photon Factory, holographic gratings are superior to mechanically ruled ones both in the reflectivity and the scattered light level, owing to the smoothness of the grating surface. VLS gratings have been, however, produced mostly by mechanical ruling because the variation of the groove densities cannot be controlled by the usual holographic method, which uses two spherical wavefronts originating at two point sources. One possible way to solve this problem is the use of aspheric wavefront holographic recording, which can be realized by inserting a spherical mirror between the laser source and the grating substrate. The feasibility of this technique was shown as the great improvement in resolution for a normal incidence monochromator [14], which covers relatively low energy region (< 40 eV). Detailed analytical formulae for this type of grating were derived by Namioka and Koike [15], and recording techniques were proposed by Harada *et al.* [16]. The possibility of applying this method to a VLS grating for a grazing incidence monochromator, *i.e.* the soft x-ray region, was demonstrated by Koike [17]. In the present study, a reasonable resolving power was actually obtained by using a VLS grating with aspheric wavefront holographic recording.

The higher spectral orders (second-, third- and higher-order components of the diffraction) also significantly affect the purity of the light. In order to eliminate such higher spectral orders and obtain the pure x rays, a harmonic-rejection double-mirror system was also installed. The second- and third-order components were diminished to below the detection limit by using the double-mirror system.

In the following sections, I outline, at first, the design of the Hettrick-type soft x-ray monochromator in §3-2. Second, the design and manufacturing of the holographic VLS grating are described in §3-3. The effects of the various errors in fabricating the grating are shown in §3-4, together with the way to compensate for these errors. The results on the performance test of the newly constructed beamline are presented in §3-5. Finally, the design concept and performance of the harmonic-rejection double-mirror system are shown in §3-6.

3-2. Design of the Hettrick-type monochromator

3-2-1. Light path function for the monochromator

Figure 3-1 shows the optical system of the Hettrick-type monochromator. The origin, O, of the Cartesian coordinate system is at the center of the VLS grating, G. The x axis is the normal to the grating surface at O and the y and z axes are perpendicular and parallel to the grooves, respectively. The spherical mirror, M_A, and G are arranged so that the point source, A (corresponding to the center of the entrance slit), O_A (vertex of M_A), O and the focal point, B (center of the exit slit), all lie in the xy plane. The principal ray originating at A is reflected at O_A, diffracted at O and reaches B. The distances between the optical elements are defined as p_A = AO_A, $q_A = O_AO$ and $r_B = OB$, and the radius of M_A is R_A. The angles α, β, and η_A are also defined as shown in Fig. 3-1.

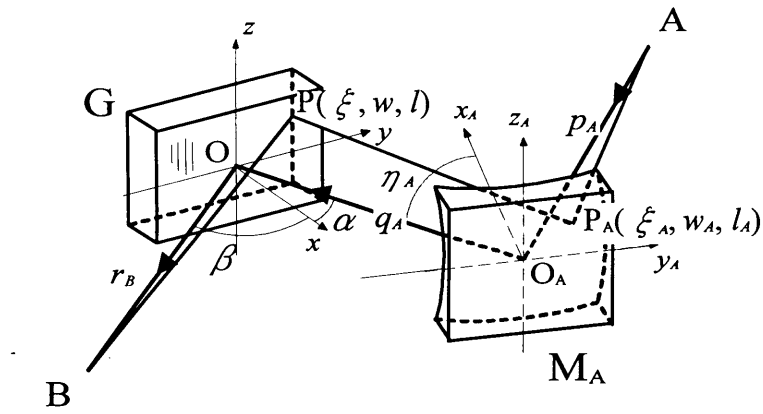

Fig. 3-1. Schematic diagram of the Hettrick-type VLS grating monochromator. Points A and B correspond to the entrance and exit slits, respectively.

For the rays passing through B after being reflected at P_A (ξ_A, w_A, l_A) and diffracted at P (ξ, w, l) on the n th groove from the center of the grating, the light path function, F, is given by

$$F = AP_A + P_AP + PB + nm\lambda, \tag{3-1}$$

where m is the diffraction order (+1 in the present design) and λ is the wavelength of the light. Expanding eq. (1) into a power series in w and l yields

$$\begin{aligned} F = {} & p_A + q_A + r_B \\ & + M_{10}w + \frac{M_{20}w^2 + M_{02}l^2 + M_{30}w^3 + M_{12}wl^2}{2} + \frac{M_{40}w^4 + 2M_{22}w^2l^2 + M_{04}l^4}{8} + \cdots \\ & + \left(n_{10}w + \frac{n_{20}w^2 + n_{02}l^2 + n_{30}w^3 + n_{12}wl^2}{2} + \frac{n_{40}w^4 + 2n_{22}w^2l^2 + n_{04}l^4}{8} + \cdots \right) m\lambda. \end{aligned} \tag{3-2}$$

Some of the coefficients M_{ij} are as follows:

$$M_{10} = -\sin\alpha - \sin\beta,$$

$$M_{20} = \frac{\cos^2\alpha}{r_A} + \frac{\cos^2\beta}{r_B},$$

$$M_{30} = \frac{\sin\alpha\cos^2\alpha}{r_A^2} + \frac{\sin\beta\cos^2\beta}{r_B^2} - \frac{2(A_{10})_A^2 K_A}{R_A}\sin\eta_A,$$

$$M_{40} = \frac{\cos^2\alpha(4\sin^2\alpha - \cos^2\alpha)}{r_A^3} + \frac{\cos^2\beta(4\sin^2\beta - \cos^2\beta)}{r_B^3}$$
$$+ \frac{2(A_{10})_A^2}{R_A} K_A (E_{40})_A \cos\eta_A + \frac{2(A_{10})_A^3}{R_A^2}\left[\frac{\cos\alpha}{r_A\cos\eta_A} - \frac{(A_{10})_A\cos\eta_A}{R_A}\right],$$

... (3-3)

where

$$r_A = q_A + \left(\frac{1}{p_A} - \frac{2\sec\eta_A}{R_A}\right)^{-1},$$

$$(A_{10})_A = -\frac{\cos\alpha}{A_A q_A \cos\eta_A},$$

$$A_A = \frac{1}{p_A} + \frac{1}{q_A} - \frac{2\sec\eta_A}{R_A},$$

$$K_A = \frac{\cos\alpha}{r_A} - \frac{(A_{10})_A}{R_A},$$

$$(E_{40})_A = -\frac{\cos\alpha}{r_A}\left[1 + \tan\eta_A(7\tan\eta_A + 12\tan\alpha)\right] + 3K_A\tan^2\eta_A\left[1 + \frac{6(A_{10})_A q_A}{R_A\cos\alpha}\right], \quad (3\text{-}4)$$

and r_A is the distance between the grating and the focal point of the rays converged by spherical mirror M_A. r_A is negative if the virtual focal point is located behind the grating. The third term in M_{30} and the third and fourth terms in M_{40} arise from taking the spherical mirror into consideration.

One should optimize the groove parameters n_{ij}'s so that the light path function, F, is nearly constant for all w, l and λ. It means that

$$F_{ij} \equiv M_{ij} + \frac{n_{ij} m\lambda}{\lambda_0} \quad (3\text{-}5)$$

should be kept close to zero during the energy scanning. Then I applied this condition to the actual optical system constructed at beamline 11A of the Photon Factory.

3-2-2. Optimization of the groove parameters for the actual monochromator

The schematic layout for the new beamline PF–BL–11A is shown in Fig. 3-2. Synchrotron radiation from a bending magnet is vertically focused on the entrance slit, S_1, by a cylindrical mirror, M_0'. Spherical mirrors, M_1 and M_2, are interchangeable and one of them is selected according to the desired photon energy range. The radii of M_1 and M_2 are determined so that the rays are focused, in the plane of dispersion, on an imaginary point 3 m behind the grating, G. It corresponds to

$$r_A = -r_B = -3 \text{ m}. \tag{3-6}$$

In fact, this relationship is not the optimized one. One can determine r_A so that $F_{20} = 0$ at two energies [6,8] and that the focal length is kept rather constant over a whole energy range. The difference from the optimized value, however, makes little effect on the resolution and, moreover, the relationship ($r_A = -r_B$) plays an important role in the adjustment of the optical components, as discussed in §3-4.

Three gratings can be mounted whose groove densities at their center are planned to be 300, 800, and 1200 *l*/mm. Included angles, $\alpha - \beta$, at G are 176.2° and 173.8°, corresponding to M_1 and M_2, respectively. The parameters of the optical elements are summarized in Table 3-1. Hereafter, I concentrate on an 800-*l*/mm grating, corresponding to $n_{10} = 800$ mm^{-1}, since it covers energy range of 200–1300 eV, which is most important for the studies on the surface chemistry. The groove parameters, n_{ij}'s, were optimized as follows:

1. Determine n_{i0}'s ($i = 2$–4) so that all F_{i0}'s equal to zero at a certain energy when M_2 is used. Here I chose 500 eV as the optimization point, which is about the center of the scanning range.
2. Calculate n_{i0}'s similarly at another energy (1000 eV) when M_1 is used.
3. Take averages of two sets of n_{i0}'s obtained in above two steps.

The optimized values are $n_{20} = -0.53272$ mm^{-2}, $n_{30} = 1.63\times10^{-4}$ mm^{-3} and $n_{40} = -2.15\times10^{-7}$ mm^{-4}.

3-2-3. Evaluation of the resolving power

In order to check the validity of the new design concept, I used the ray-tracing program SRXRAY [18] with some modifications. One can simulate with this program how the light is reflected and diffracted by the mirrors and grating, respectively, and can obtain the simulated image of the light at any point of the monochromator. The source size and divergence of the synchrotron radiation were estimated as $\sigma_x = 1.263$ mm, $\sigma_y = 0.206$ mm, $\sigma'_x = 0.394$ mrad and $\sigma'_y = 0.037$ mrad [19]. To evaluate the resolving power, I adopted the method proposed by Koike and Namioka [11]. They defined the resolving power as $R = \lambda/\Delta\lambda$, where $\Delta\lambda = 2.688 s_\lambda$, and s_λ is the

product of the standard deviation of ray-traced spots in the direction of dispersion and the reciprocal linear dispersion at λ. The entrance slit width was chosen to be 10 μm to emphasize the effect of aberrations.

Figure 3-3 shows the spots diagrams and line profiles at the exit slit in two cases: (a) n_{20}, n_{30} and n_{40} were optimized using the light path function for the grating alone (conventional method); (b) the spherical mirror was taken into consideration. The other n_{ij}'s were set to zero and therefore the grooves are independent of l, corresponding to the straight grooves. The difference between the two methods is obvious and is comes from the aberration of the spherical mirror. For case (a), the estimated resolving power is shown in Fig. 3-4 as a function of the photon energy. It was found that one can obtain the resolving power of more than 5000 for 200–1300 eV if the spherical mirror is chosen properly. The present groove parameters are directly applicable to the mechanically ruled grating with straight grooves.

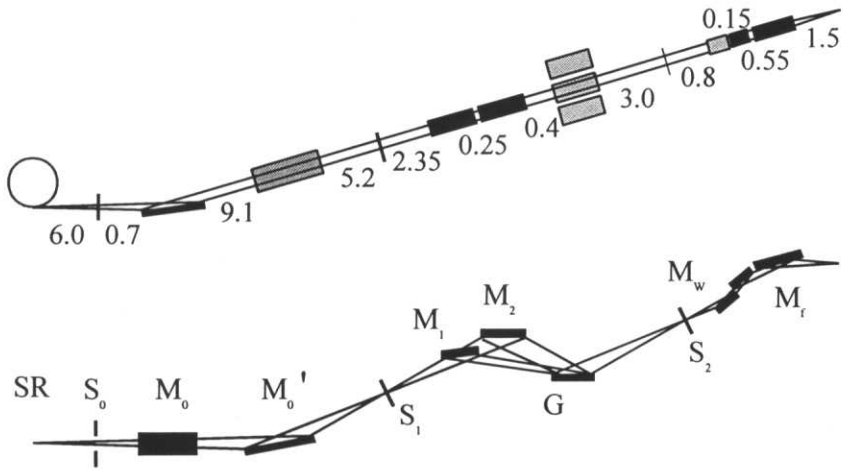

Fig. 3-2. Schematic top view (top) and side view (bottom) of the new grazing incidence monochromator. Distances between the optical components are indicated in m.

Table 3-1. Designed parameters of the optical components in the monochromator.

	Incidence angle [°]	Shape	Radius [m]	Dimensions (l × w × t) [mm]
M_0	88.0	Cylindrical	370.0	1000 × 60 × 50
M_0'	88.0	Cylindrical	224.6	600 × 60 × 50
M_1	88.1	Spherical	86.19	200 × 50 × 30
M_2	86.9	Spherical	54.49	200 × 50 × 30
G		Plane		80 × 30 (ruled area) × 20
M_W	80–88.5	Plane		130 × 80 × 20
M_f	88.0	Toroidal	43.0 (m.), 0.104 (s.)	200 × 50 × 30

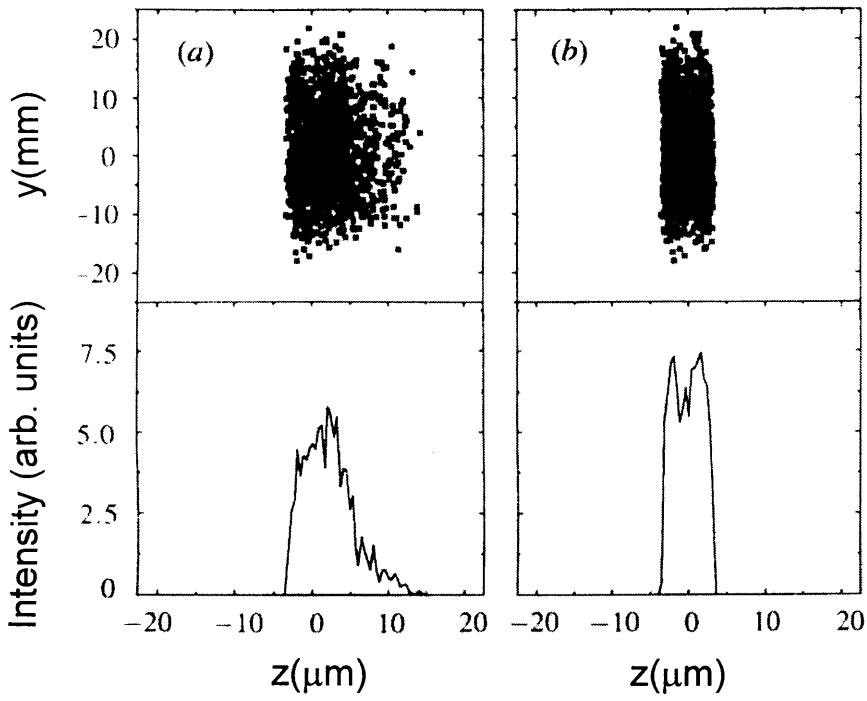

Fig. 3-3. Spot diagrams (top) and line profiles (bottom) of the ray-traced spots at the exit slit for two different design methods: (a) using the light path function for the grating alone and (b) using the light path function including the spherical mirror.

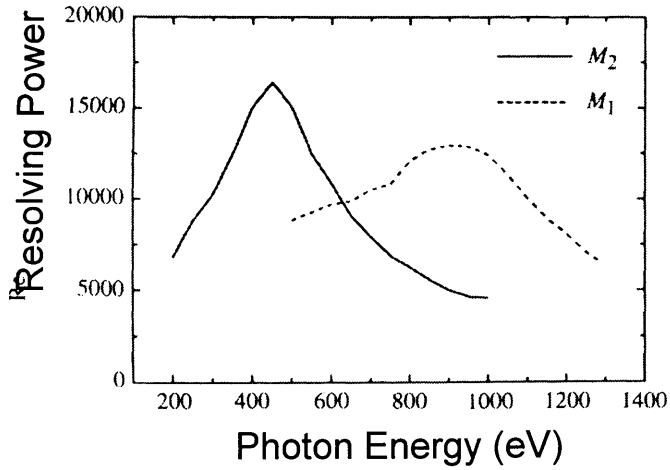

Fig. 3-4. Estimated resolving power for the straight-groove VLS grating with M_2 (solid line) and M_1 (dashed line).

3-3. Fabrication of a holographic VLS grating

3-3-1. Relation between the groove parameters and the recording optics

For the holographic grating, the groove parameters n_{ij}'s appearing in eq. (3-2) are related to the parameters of the recording optics shown in Fig. 3-5. Mc and MD are both spherical mirrors whose radii are R_C and R_D, respectively. The rays generated at sources C and D are reflected by Mc and MD, respectively, and illuminate the grating substrate, G. The *xyz* coordination systems are introduced in the same manner as shown in Fig. 3-1. The substrate and mirrors are arranged so that Oc and OD (vertexes of Mc and MD, respectively) lie in the *xy* plane. The incidence angles γ, δ, η_C and η_D are defined as shown in Fig. 3-5. Note that δ and γ are defined so that $\delta - \gamma$ is larger than zero.

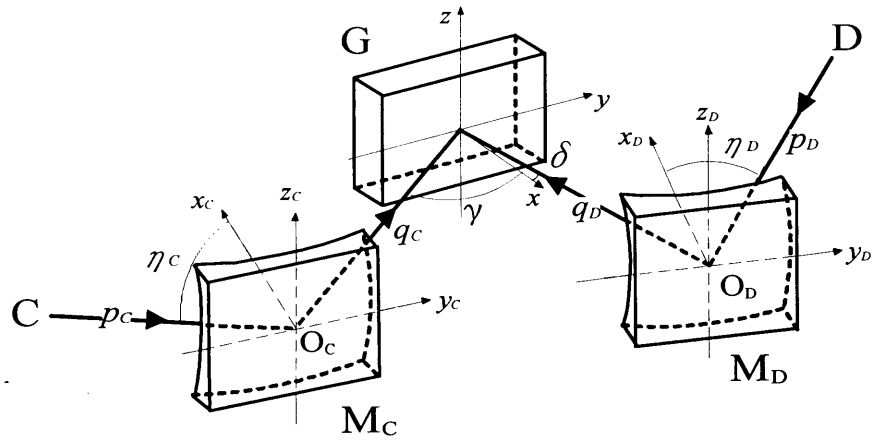

Fig. 3-5. Schematic diagram of the optical system for aspheric wavefront holographic recording.

The groove parameters n_{ij}'s can be expressed as a function of R_C, R_D, p_C, p_D, q_C, q_D, γ, δ, η_C and η_D, based on the derivations in Ref. 15. Here parameters h_{ij}'s are introduced to make the relationship simple:

$$h_{ij} \equiv n_{ij} / \lambda_0, \tag{3-7}$$

where λ_0 is the wavelength of light used for the holographic recording. The obtained equations are:

$$h_{10} = \sin\delta - \sin\gamma,$$

$$h_{20} = \frac{\cos^2\gamma}{r_C} - \frac{\cos^2\delta}{r_D},$$

$$h_{30} = \frac{\sin\gamma\cos^2\gamma}{r_C^2} - \frac{\sin\delta\cos^2\delta}{r_D^2} - \frac{2(A_{10})_C^2 K_C}{R_C}\sin\eta_C + \frac{2(A_{10})_D^2 K_D}{R_D}\sin\eta_D,$$

$$h_{40} = \frac{\cos^2\gamma(4\sin^2\gamma - \cos^2\gamma)}{r_C^3} - \frac{\cos^2\delta(4\sin^2\delta - \cos^2\delta)}{r_D^3}$$
$$+ \frac{2(A_{10})_C^2}{R_C} K_C (E_{40})_C \cos\eta_C + \frac{2(A_{10})_C^3}{R_C^2}\left[\frac{\cos\gamma}{r_C\cos\eta_C} - \frac{(A_{10})_C\cos\eta_C}{R_C}\right]$$
$$- \frac{2(A_{10})_D^2}{R_D} K_D (E_{40})_D \cos\eta_D - \frac{2(A_{10})_D^3}{R_D^2}\left[\frac{\cos\delta}{r_D\cos\eta_D} - \frac{(A_{10})_D\cos\eta_D}{R_D}\right],$$

... (3-8)

where

$$r_C = q_C + \left(\frac{1}{p_C} - \frac{2\sec\eta_C}{R_C}\right)^{-1},$$

$$(A_{10})_C = -\frac{\cos\gamma}{A_C q_C \cos\eta_C},$$

$$A_C = \frac{1}{p_C} + \frac{1}{q_C} - \frac{2\sec\eta_C}{R_C},$$

$$K_C = \frac{\cos\gamma}{r_C} - \frac{(A_{10})_C}{R_C},$$

$$(E_{40})_C = -\frac{\cos\gamma}{r_C}\left[1 + \tan\eta_C(7\tan\eta_C + 12\tan\gamma)\right] + 3K_C\tan^2\eta_C\left[1 + \frac{6(A_{10})_C q_C}{R_C\cos\gamma}\right], \quad (3\text{-}9)$$

and r_D, $(A_{10})_D$, A_D, K_D, and $(E_{40})_D$ are defined by eq. (3-9), substituting C and γ for D and δ, respectively.

3-3-2. Design of the recording optics for an 800-*l*/mm holographic VLS grating

I determined the parameters of the aspheric wavefront holographic recording optics using the groove parameters, n_{i0}'s (i = 1–4), optimized in §3-2-2. Spherical mirror M$_D$ was omitted (corresponding to $R_D = \infty$) to make the recording optics simple and to reduce the errors in the optical alignments. I solved only four equations for n_{10}, n_{20}, n_{30} and n_{40}, choosing γ, δ, r_D (= p_D + q_D) and η_C as the optimization parameters. Obtained recording parameters are p_C = 1.35 m, q_C = 0.55 m, r_D = 2.509 m, γ = −42.756°, δ = −19.002°, η_C = 34.360° and R_C = 5.0 m. The parameters other than γ, δ, r_D and η_C were chosen so that they are of practical size without making n_{ij}'s ($j \neq 0$) too large. The groove parameters calculated from these recording parameters are listed in Table 3-2(b).

Figure 3-6 shows the calculated groove shapes of the holographic grating whose groove parameters are listed in Table 3-2(b). It can be seen that the grooves are almost straight, being bent by only about 1 mrad at most. The difference between the groove spacing at the center ($l = 0$ mm) of the grating and at near the edge ($l \sim \pm 15$ mm) is less than 0.3 Å (about 0.0024 % of the groove spacing). One no longer need to be anxious about the groove shapes of the holographic grating, but only have to take care of the gradation of the groove densities along the w axis (the centerline of the grating). This corresponds to the fact that all n_{ij}'s other than n_{i0}'s are reasonably small.

Table 3-2. Groove parameters n_{ij}'s for the VLS gratings: (a) the straight-groove grating, (b) holographic one ideally optimized including n_{40} and (c) holographic one presently produced.

	(a)	(b)	(c)
n_{10}	800.0 mm^{-1}	800.0 mm^{-1}	800.0 mm^{-1}
n_{20}	-0.53272 mm^{-2}	-0.53272 mm^{-2}	-0.53272 mm^{-2}
n_{30}	1.63×10^{-4} mm^{-3}	1.63×10^{-4} mm^{-3}	1.63×10^{-4} mm^{-3}
n_{40}	-2.15×10^{-7} mm^{-4}	-2.15×10^{-7} mm^{-4}	3.81×10^{-7} mm^{-4}
n_{02}	0 mm^{-2}	-0.144 mm^{-2}	-0.119 mm^{-2}
n_{12}	0 mm^{-3}	8.76×10^{-5} mm^{-3}	-3.14×10^{-5} mm^{-3}
n_{22}	0 mm^{-4}	5.27×10^{-8} mm^{-4}	3.38×10^{-7} mm^{-4}
n_{04}	0 mm^{-4}	-9.33×10^{-8} mm^{-4}	4.68×10^{-7} mm^{-4}

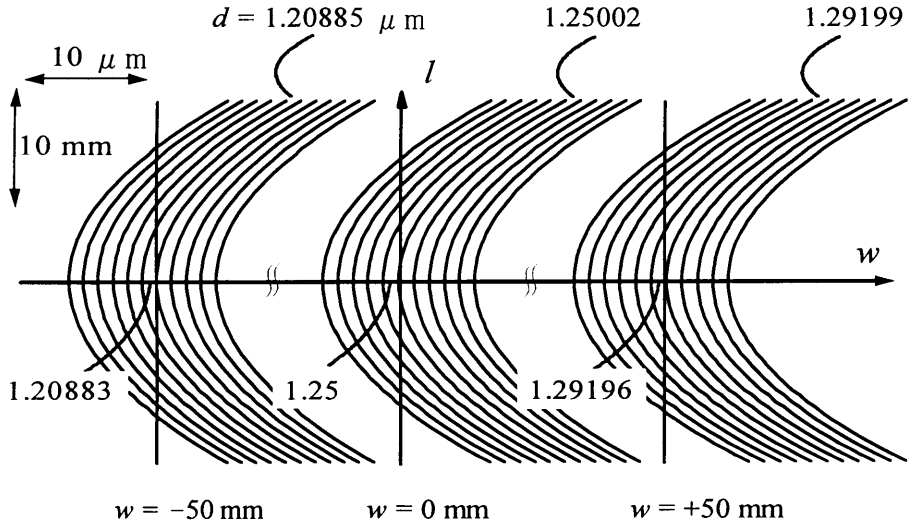

Fig. 3-6. Groove shapes for a holographic grating calculated using the groove parameters shown in Table 3-2(b). Note that the magnifications along the w and l axes are not the same.

Unfortunately, the recording parameters determined above cannot be adopted since the dimension of the available optical bench for the holographic recording was about 1 m × 2 m. Under this restriction of the space, I could not find any recording parameters which realize the optimized n_{i0}'s (i = 1–4). Only the first three n_{i0}'s (i = 1–3) could become optimized as listed in Table 3-2(c), using the following recording parameters: p_D = 0.90 m, q_D = 0.30 m, r_C (= p_C + q_C) = 1.814 m, γ = −48.335°, δ = −23.189°, η_D = 20.934° and R_D = 5.0 m, where Mc was omitted.

The calculated resolving powers are shown in Fig. 3-7 for the holographic VLS gratings whose groove parameters are listed in Table 3-2(b) and (c), together with that for a mechanically ruled grating with the straight groove [Table 3-2(a)]. It was shown that the holographic VLS grating can provide the resolving power as high as that for the mechanically ruled one, if all n_{i0}'s (i = 1–4) are optimized. The resolving power is decreased by ~20 % at most for the presently produced holographic grating whose groove parameter n_{40} is not optimized.

3-3-3. Fabrication and evaluation of the holographic grating

For the fabrication of the holographic grating, the spherical mirror, M_D, was produced and its radius was measured. The recording parameters should be re-calculated using the measured radius. In the present case, it was not necessary because the radius, (4.999 ± 0.010) m, was the same as the designed one, 5.0 m, within the error bar. However, this procedure is essential when the spherical mirror is not precisely produced, as is often the case. All the optical elements for the holographic recording were aligned with the geometrical errors of less than 2 mm for distances and 0.5° for angles. A quartz substrate (120 mm × 60 mm × 20 mm) with the surface rms roughness of less than 5 Å was prepared for the fabrication of the grating. Laminar-shaped grooves were ruled on the blank with aspheric wavefront holographic recording described above,

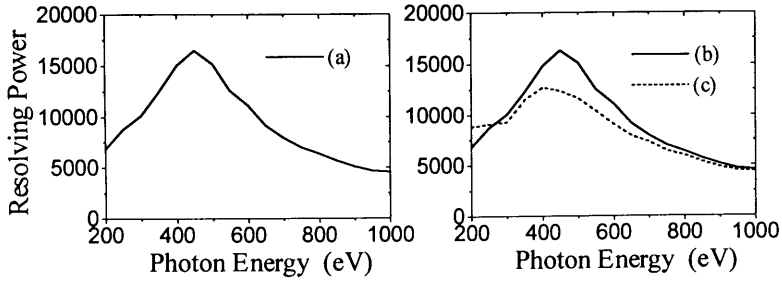

Fig. 3-7. Evaluated resolving power as a function of photon energy for the (a) straight-groove grating, (b) holographic one ideally optimized including n_{40} and (c) holographic one presently produced.

and with a successive ion-etching procedure. The ruled grating was then coated with a gold layer of ~35 nm thickness.

The groove profiles of the present holographic VLS grating were measured by two different methods. Figure 3-8 shows the three parts of the grating surface for w = +35, 0 and −35 mm. These profiles were measured by a contact probe, whose diameter was 0.2 μm. A more precise measurement was carried out to obtain a three-dimensional surface profile by an atomic force microscope (Fig. 3-9). It is apparent from Fig. 3-8 that the groove density decreases with increasing w. The groove depth is estimated to be (8±1) nm while the designed value is 7 nm. Suppose that the grating surface of the plateau part is not deteriorated during the ion-etching procedure, as this is the case, it is very likely that the effective surfaces of both the plateau and valley parts have the roughness of 5 Å in rms.

To evaluate the groove parameters of the presently produced holographic grating, the groove densities were measured at different nine points along the centerline (l = 0) of the grating, as listed in Table 3-3. The groove density was obtained by measuring the diffraction angles of a 6328 Å light (He-Ne laser) at each point on the grating. The uncertainty of the groove density was ~ ±0.1 *l*/mm. I obtained n_{10} = (800.69 ± 0.03) m^{-1} and n_{20} = (−0.533 ± 0.002) m^{-2}, from the least squares fitting for these groove densities. The other groove parameters such as n_{30} and n_{40} could not be evaluated properly because the uncertainty of these parameters was too large. I performed a ray-tracing simulation using the obtained groove parameters and estimated the shift of the focal length to be (+2 ± 8) mm at 400 eV.

Table 3-3. Groove densities of the present holographic grating measured at the centerline of the grating.

w (mm)	−35.72	−26.69	−17.75	−8.78	+0.09	+9.31	+18.22	+27.23	+36.23
Groove density (l/mm)	819.0	814.0	809.1	804.4	799.7	794.8	790.1	785.5	780.9

Fig. 3-8. Groove profiles of the present holographic grating measured by a contact probe at (a) $w = +35$ mm, (b) $w = 0$ mm and (c) $w = -35$ mm.

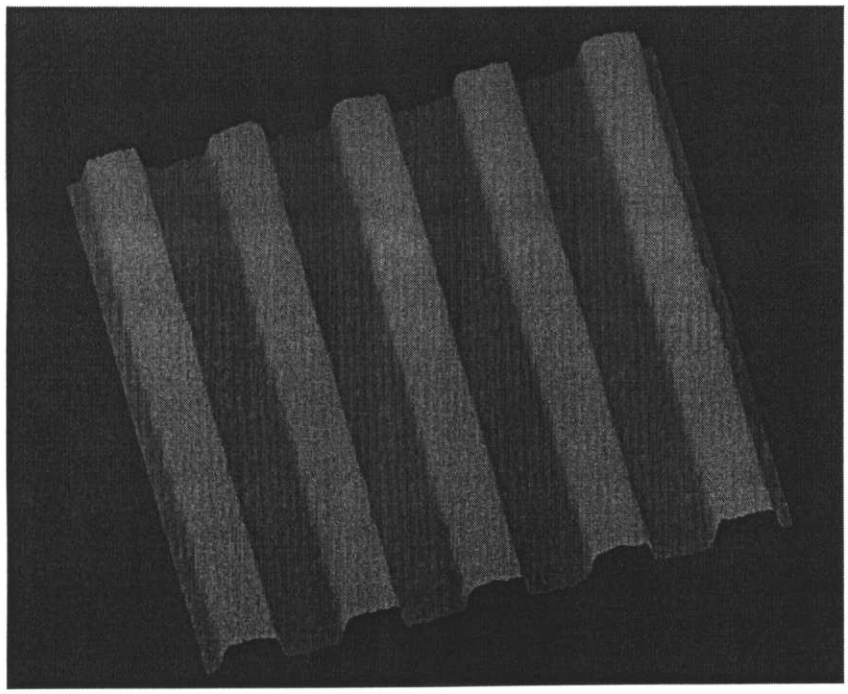

Fig. 3-9. Atomic force microscope image of the holographic VLS grating.

3-4. Effects of errors and their compensation

3-4-1. Errors in the recording optics

The effects of the errors in the parameters for holographic recording are shown in Fig. 3-10, indicating that the precision described in §3-3-3 (2 mm for distances and 0.5° for angles) might not be sufficient. Some of these errors were, however, reduced in the recording process because the groove density of the grating was measured at its center and the optical elements were adjusted repeatedly so that the groove density was as close to 800 *l*/mm as possible. Moreover, the recording optics can be re-aligned to make a more precise VLS grating by measuring the groove parameters, especially n_{20}, iteratively.

The degradation of the resolving power is mostly due to the shift of the focal length, *i.e.*, the change in n_{20}, as shown in Fig. 3-11 (top) for δ and p_D as examples. On the other hand, the errors in the recording parameters make slight changes in n_{30} and n_{40}, resulting in little effect on the resolving power. In fact, for instance, n_{30} becomes smaller than the optimized value by only 1 % even if δ is larger than the designed angle by 0.5°. Accordingly, one can compensate for these errors to some degree by translating the exit slit as shown in Fig. 3-11. However, since the shift of the focal length depends on the photon energy, the exit slit may be translated during the energy scan, if one wish the ultimate resolving power. Another compensation method can be adopted, where no translation of the exit slit is necessary during the energy scan [20]. I will describe it at the end of the following section.

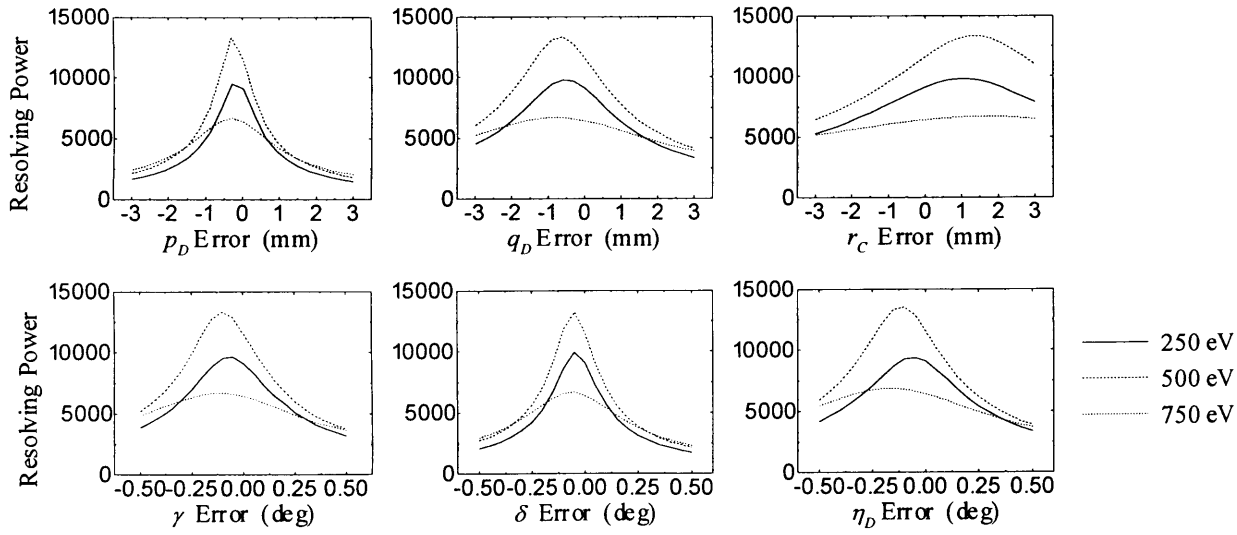

Fig. 3-10. Effects of errors in the recording parameters on the resolving power at three typical energies when M_2 is used.

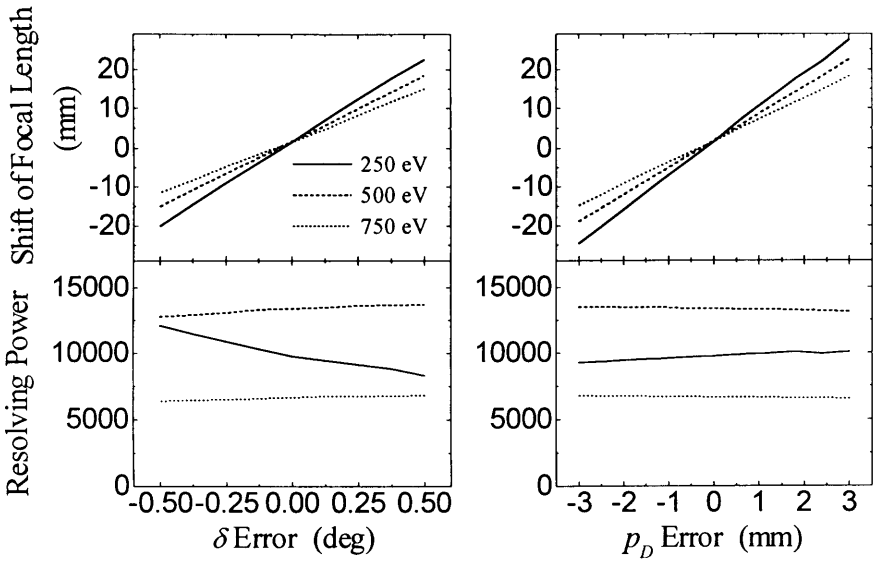

Fig. 3-11. Compensation for the errors in δ and p_D: Shift of the focal length (top) and resolving power when the exit slit is translated to the focal point (bottom).

3-4-2. Errors in the radii of the spherical mirrors M_1 and M_2

Another possible error exists in the radius of the spherical mirror in the monochromator. The effects of the error in R_2 (radius of M_2) are shown in Fig. 3-12(a). As indicated in Fig. 3-12(b), the reduction of the resolving power is due to the change of r_A, which is determined by R_2 as indicated in eq. (3-4). In order to compensate for this error, r_A should be returned to its designed value, $-r_B$ (–3 m in the present case), by changing η_A, p_A and q_A. Note that the principal ray must be kept to illuminate the center of the grating. The concept of the compensation is schematically depicted in Fig. 3-13. When the compensation is carried out, the resolving power is almost perfectly restored as shown in Fig 3-12(c).

One must, however, estimate the actual value of r_A to carry out this compensation. It should be recalled that r_A represents the distance between the grating and the focal point of the rays converged by the spherical mirror M_A. Accordingly, rays are focused on the point separated by $|r_A|$ from the grating, when the grating is used as a plane mirror, *i.e.* the incidence and emission angles are set to be the same (the reflected rays in this condition are called "zeroth-order" rays). The zeroth-order rays are, therefore, focused on the exit slit when r_A equals $-r_B$, since the distance between the grating and the exit slit is r_B. The reason why I adopted the relationship $r_A = -r_B$ is now clarified: one can confirm that the error in the radius of M_A is properly compensated, when the zeroth-order rays are found to be focused on the exit slit.

Let me here describe the possibility of a compensation for the error in n_{20} by changing r_A. It has been shown that the focal length shift can be kept rather constant, as long as the relationship between r_A and r_B ($r_A = -r_B$ in the present case) is not changed [20]. It means that if one translates the exit slit, for instance, to the downstream (therefore r_B becomes larger) in order to compensate for the error in n_{20}, one must make $|r_A|$ larger by adjusting M_A. This procedure causes, however, more focal length shift to the downstream, so that one must repeat the above adjustments of the exit slit and M_A. Although the required amounts of the translation of the exit slit and adjustment of M_A can be easily calculated and no repeatedly adjustments are necessary, the problem is the amount of the exit slit translation. This compensation requires a few times longer translation than those indicated in Fig. 3-11. Since the long translation of the exit slit costs so much even if the slit movement during the energy scan is not necessary, it is important to fabricate the VLS grating with precise groove parameters.

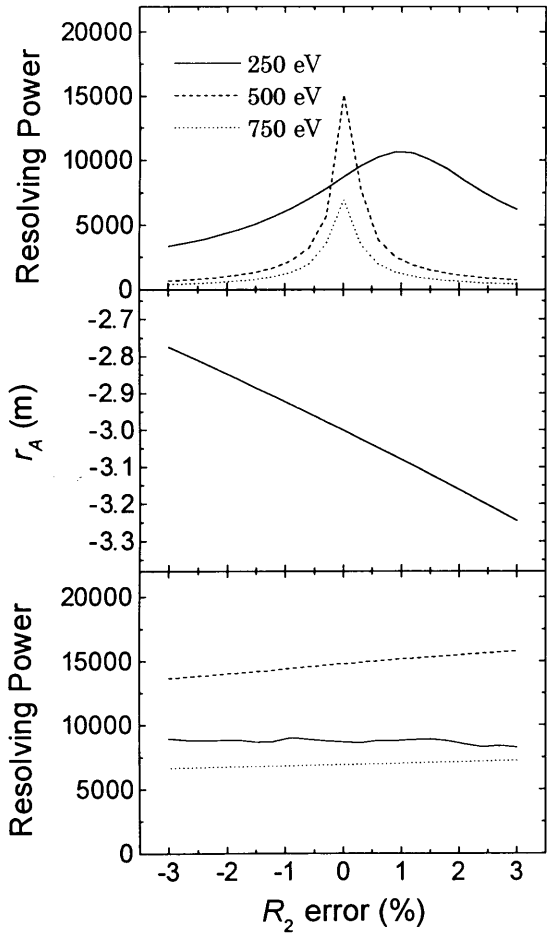

Fig. 3-12. Effects of errors in R_2 (Radius of M_2) and their compensation: (a) decrease in the resolving power, (b) variation of r_A and (c) resolving power after proper compensation.

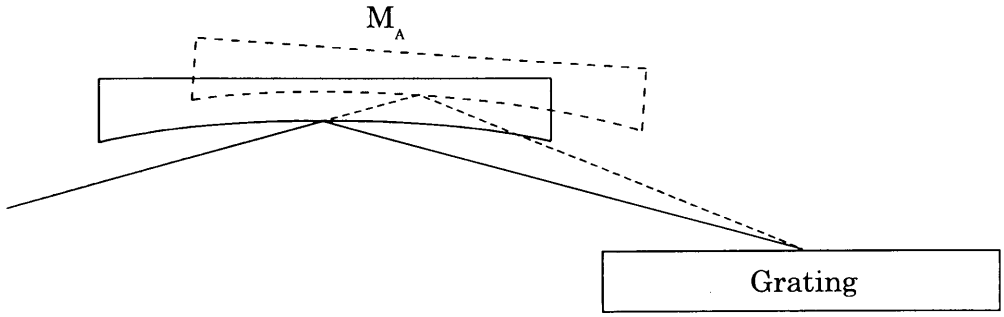

Fig. 3-13. Concept of the compensation for the error in the radius of the spherical mirror M_A.

3-4-3. Alignment of the beamline components

It is essential to align precisely the optical components in the beamline, especially those installed between the entrance and exit slits, for attaining the designed performance. It is also important to compensate for the errors such as those in the radii of the spherical mirrors and in the groove parameters of the grating, as described in the previous section. All the optical elements in the beamline were aligned using an ordinary surveying instrument equipped with a laser light source. Errors of alignments were less than 0.1 mm for height and 2 mm for distance between each component. The tilting angles of the slits, and the rolling angles of the spherical mirrors and the grating were adjusted with the precision of 0.06° and 0.03°, respectively. The ray-tracing simulation (not shown) indicated that these errors are negligible or can be compensated with the following adjustments.

The adjustments consist of two steps: the first step uses the zeroth-order rays and the second one uses the diffracted rays. The purpose of the first step is to make r_A equal $-r_B$ to compensate for the error in the radius of the spherical mirror, M_i (i = 1 or 2), and those in the alignments of the optical elements. The relation, $r_A = -r_B$, can be satisfied by changing η_A (incidence angle of M_i), keeping the principal ray to illuminate the center of the grating with an appropriate translation of M_i along the incident rays. The amounts of the rotation and translation to compensate for 3 % error in the radius of M_2 are about 0.1° and 10 mm, respectively. To assure that $r_A = -r_B$ is satisfied, it must be checked that the zeroth-order rays are focused on the exit slit. Figure 3-14 shows the schematic view of the paths of the zeroth-order rays when they are focused on the upstream of the exit slit, S_2, *i.e.* $|r_A| < r_B$. It can be seen that the rays which pass through the aperture, S_0, at the higher position (solid line) arrive at the lower position of S_2. Accordingly, for the different vertical position of S_0, the maximum transmission intensity of the zeroth-order rays is observed at the downstream of S_2 at a different rotation angle of the grating, G (see Fig. 3-15).

Thus, one can recognize that $r_A = -r_B$ is satisfied when the peak of the zeroth-order reflection appears at the same angle of G regardless of the vertical position of S_0. The incidence angle of M_2 was adjusted within 0.002°, which dose not affect the resolving power significantly.

The second step comprises the adjustment for the grating yawing angle (rotation around the surface normal), and the tilting (rotation around the direction of the light) and translation of the exit slit, S_2. The yawing angle was adjusted so that the diffracted rays illuminate the same horizontal position on S_2 as the zeroth-order rays. The uncertainty of the yawing angle was estimated to be about 1°, which again dose not affect the resolution seriously. Errors in the grating yawing angle as well as those in the rolling angles of all the optical components can be partly compensated by adjusting the tilting angle of S_2. One can also compensate for the errors in the groove parameters, mainly in n_{20}, by translating S_2 to the focal point of the diffracted rays (see § 3-4-1). Both these adjustments were performed essentially in the same manner as for the first step. When a certain absorption peak, *e.g.* $1s \rightarrow \pi^*$ resonance of molecular nitrogen, appears at the same diffraction angle regardless of the vertical position of S_0, it can be recognized that the diffracted rays are focused on S_2. The translation of S_2 could be adjusted with the error of less than 2 mm, at the photon energy of about 400 eV. The focal length was longer than the designed value by ~15 mm for the present grating. To adjust the tilting angle of S_2, another aperture was used to restrict the horizontal acceptance, by which either the right or left part of the rays can be chosen. Thus the slit tilting angle could be adjusted with the error of less than 0.03°, so that the absorption peak appeared at the same diffraction angle regardless of whichever part of the rays are used.

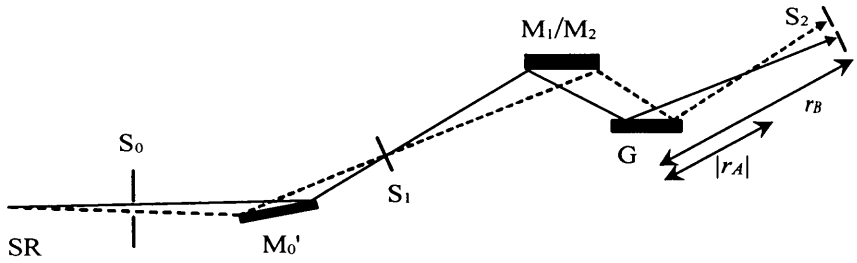

Fig. 3-14. Schematic view of the light paths for the zeroth-order rays pass through S_0 at the higher position (solid line) and lower position (dashed line).

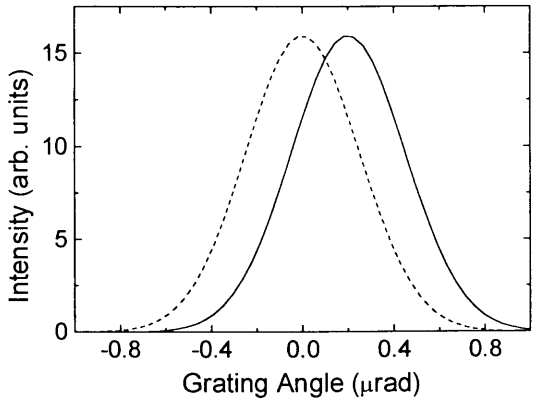

Fig. 3-15. Zeroth-order transmission intensity measured at the downstream of the exit slit as a function of the grating angle for the upper (solid line) and lower (dashed line) part of the rays. The shift of the peak position indicates that the zeroth-order rays are focused on the upstream of the exit slit.

3-5. Performance of the new beamline

3-5-1. Resolving power

To evaluate the resolving power of the monochromator, N *K*-edge absorption spectra of N_2 were measured. Figure 3-16(a) shows the total ion yield spectrum of N_2 recorded around 400 eV using the first-order light ($m = +1$) with the combination of the mechanically ruled 800-*l*/mm grating and the spherical mirror M_2. The entrance- and exit-slit widths were 15 and 8 μm, and the horizontal and vertical acceptances were 2 and 0.2 mrad, respectively. The photon flux obtained under this condition was about 5×10^7 photons/s. The resolution was estimated by fitting the data with a convoluted profile of a Gaussian and Lorentzian functions. The Lorentzian peak width Γ was taken as 117 meV of the proposed lifetime broadening for the N_2 $1s \rightarrow \pi^*$ resonance [21]. A resolving power $R = \lambda/\Delta\lambda$ of ~6900 was obtained, where $\Delta\lambda$ is a FWHM of the Gaussian function.

As for the holographic grating, the resolving power was estimated to be ~4500 as shown in Fig. 3-16(b), though the slit widths were narrower than those for the mechanically rule one. The exit-slit width and vertical acceptance were 5 μm and 0.1 mrad, respectively, while the entrance-slit width was unchanged. There may be three reasons for this lower resolution. The first possible one is that the adjustments were not perfect. It was, however, confirmed by the ray-tracing

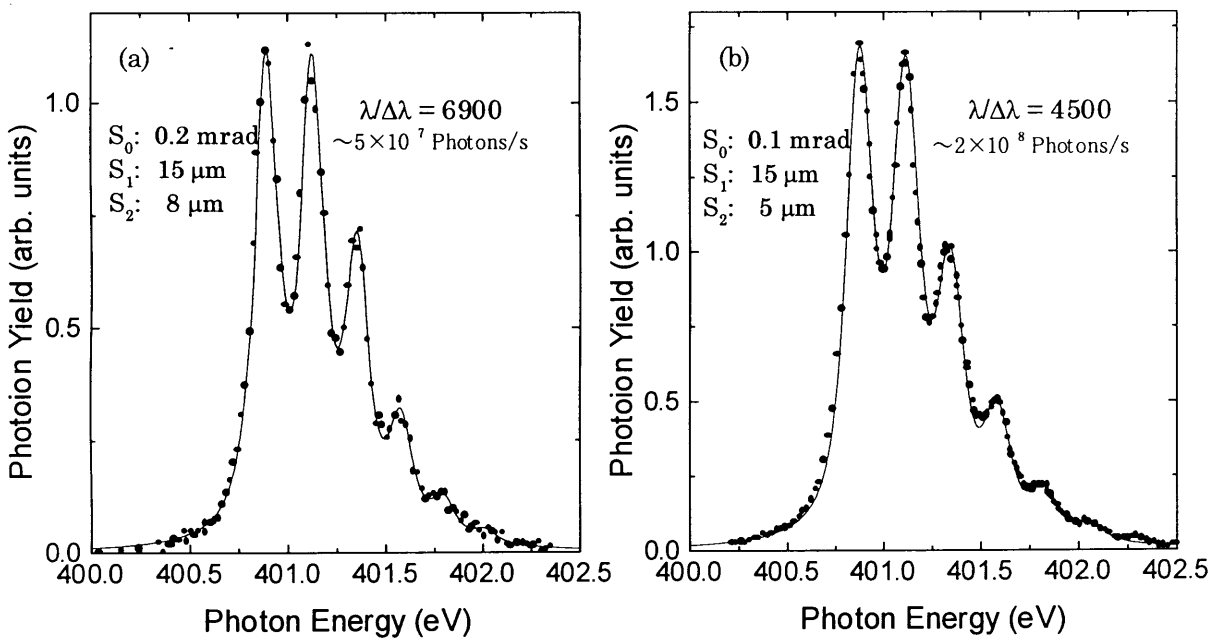

Fig. 3-16. N_2 $1s \rightarrow \pi^*$ resonance absorption spectra taken by the total ion yield detection with the (a) mechanically ruled and (b) holographic gratings. S_0, S_1 and S_2 denote the vertical acceptance and entrance- and exit-slit widths, respectively.

simulation that the resolving power can be kept to ~15000, even if the exit slit is translated by 2

mm or tilted by 0.03° from the desired position or angle, respectively. The second reason is the figure errors in the mirrors and grating. In fact, the ray-trace results showed that the resolving power is reduced to ~6000 if the grating has a 0.2 arcsec slope error, which is plausible for the present holographic grating. The third one is the mechanical vibration of the optical bench for the grating. When the holographic grating is used, a fairly larger oscillation was observed in the intensity of the zeroth-order rays measured after the exit slit, compared the mechanically ruled grating. This indicates that the mechanical vibration is enhanced for the holographic grating.

3-5-2. Photon flux and scattered light level

Figure 3-17 shows the photon flux distribution curves from the monochromator obtained with two gratings combined with M_2. They were measured by a Au-coated mesh calibrated with a photodiode. The vertical acceptance was 0.2 mrad and both the entrance- and exit-slit widths were 100 μm. The resolving power at these conditions varies from ~1500 (at 200 eV) to ~500 (at 1000 eV) and it is ~800 at 500eV. For the holographic grating, the photo current approaches to zero with the increase in the photon energy beyond 1300 eV. This indicates that the scattered light level for the present holographic grating is very low, owing to the surface smoothness. On the contrary, the scattered light level for the mechanically ruled grating is much higher, and the photon flux is fairly lower over a whole energy range, compared to the holographic one.

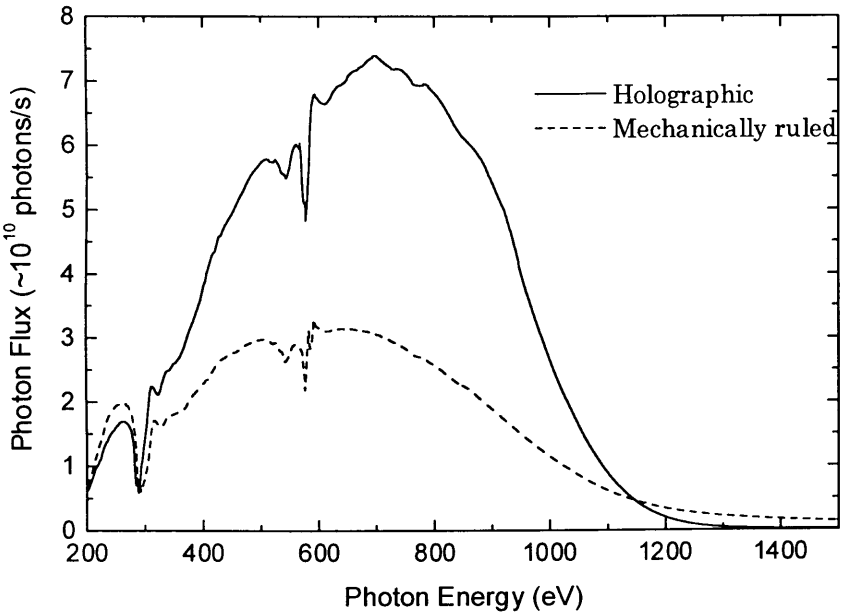

Fig. 3-17. Photon flux distribution at PF-BL-11A with the holographic (solid line) and mechanically ruled (dashed line) gratings combined with M_2.

Figure 3-18 shows the photon flux distribution in the high-energy region obtained with a combination of the holographic grating and the spherical mirror M_1. The slit conditions were the same as those mentioned in the previous paragraph. The resolving power is ~750 at 750 eV while it is ~500 at 1500 eV. Again the photon intensity above ~2000 eV is almost zero, indicating that the scattered light level is quite low even in the high-energy region.

3-5-3. Degree of linear polarization

In order to determine the degree of linear polarization for the beamline, the angle-resolved photoion spectra [22] were measured for the N *K*-edge absorption of N_2. In the previous study [22], angular distribution asymmetries of photofragments were clearly observed by using the linearly polarized light, based on the following principle. For randomly oriented molecules with cylindrical symmetry, the molecular orientation along the direction Ω_m is described by an orientation parameter β_m:

$$\frac{d\sigma(\hbar\omega)}{d\Omega_m} = \frac{\sigma(\hbar\omega)}{4\pi}[1 + \beta_m(\hbar\omega)P_2(\cos\theta_m)], \tag{3-10}$$

where θ_m is the angle between the molecular axis and the electric vector of linearly polarized light, and $P_2(\cos\theta_m)$ is the second Legendre polynomial. The orientation parameter is expressed as

$$\beta_m = \frac{2[D_\sigma^2(\hbar\omega) - D_\pi^2(\hbar\omega)]}{D_\sigma^2(\hbar\omega) + 2D_\pi^2(\hbar\omega)}, \tag{3-11}$$

where D_σ^2 and D_π^2 are the photoabsorption strengths for molecular orientation along (σ) and perpendicular to (π) the electric vector of the light, respectively. They derived the orientation parameter with the angle-resolved photoion spectroscopy, reasonably assuming that the molecular orientation induced by the *K*-shell photoabsorption holds during the subsequent Auger decay leading to the fragment ions [22]. This assumption means that $\theta_m = 0°$ for an ion detector placed in the horizontal direction, while $\theta_m = 90°$ for the vertical direction, because the electric vector was in the horizontal plane. The orientation parameter was reported to be $\beta_m = -1$ at the discrete π^* resonance position.

In the present measurements, I can assume the orientation parameter $\beta_m = -1$ at the π^* resonance, according to their result. Therefore photoion should be observed only in the vertical direction if the electric vector is completely in the horizontal plane (100% polarization). Figure 3-19 shows the photoion intensities detected in the vertical and horizontal directions. It can be seen

that only small signal is observed at the π* resonance, in the horizontal direction. Assuming that the acceptance of the ion detector is 10°, the degree of linear polarization was estimated to be ~95%, from the intensity ratio of the two spectra.

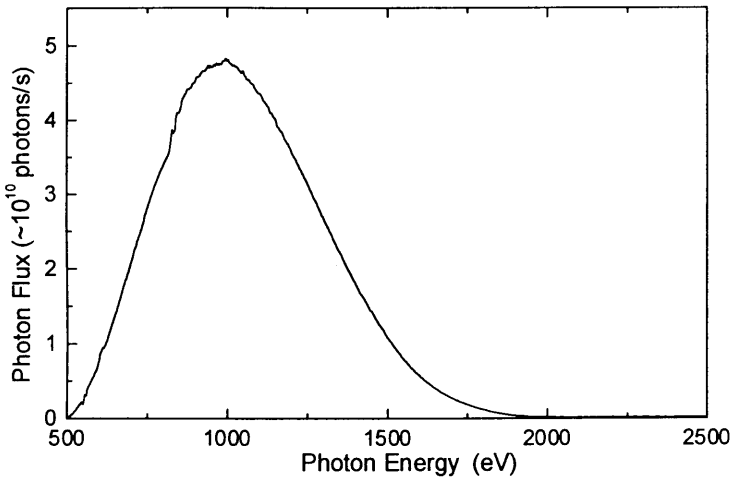

Fig. 3-18. Photon flux distribution obtained with a combination of the holographic grating and the spherical mirror M_1.

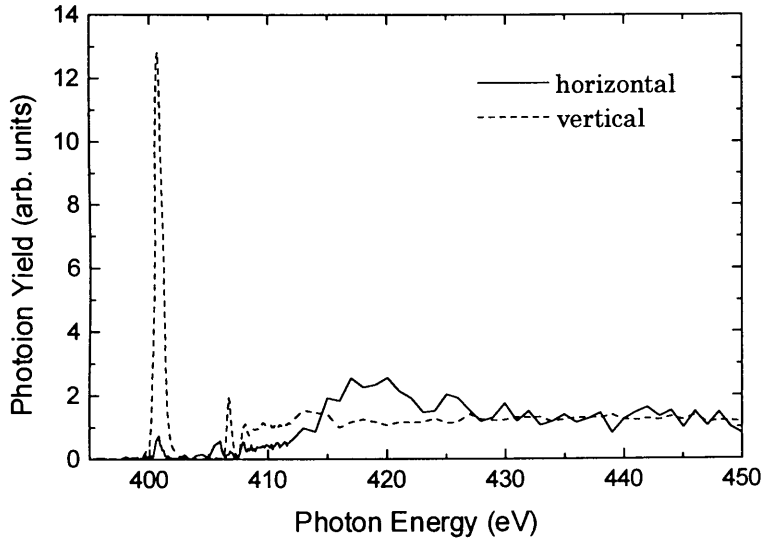

Fig. 3-19. N_2 $1s \rightarrow \pi^*$ absorption spectra taken with the total ion yield detectors placed in the vertical (solid line) and horizontal (dashed line) direction. The spectra are normalized so that the intensities at the high-energy region (430–450 eV) becomes the same.

3-6. Double-mirror system for the harmonic rejection

3-6-1. Concept of the harmonic-rejection system

The higher spectral orders can be effectively eliminated by using an appropriate mirror at a proper angle as a low-energy pass filter. For the present purpose, silicon was chosen as a material of the harmonic-rejection mirror because it has a sharp cut-off property and no absorption edges in a wide energy range of 100–1800 eV. The reflectivity curves for a Si mirror at some glancing angles are shown in Fig. 3-20.

The installed double-mirror system, Mw, is schematically illustrated in Fig. 3-21. Two 130-mm long Si plane mirrors are arranged so that they are parallel to each other and the distance between their surfaces is 4 mm. The mirrors are rotated around the axis at the symmetry center keeping their relative position unchanged. The important features of this system are that the rotation is controlled by a sine-arm mechanism driven by a stepping motor and that the output-beam position is approximately kept fixed during the rotation as shown in Fig. 3-21. This allows the simultaneous rotation of the mirrors with the energy scan, which is essential for the wide-energy scan as the EXAFS measurements. At each energy, the incidence angles of the mirrors are set so that the first order rays are reflected well and higher orders are rejected. The mirrors can be also removed away from the light path, though the exit beam position changes by ~8 mm.

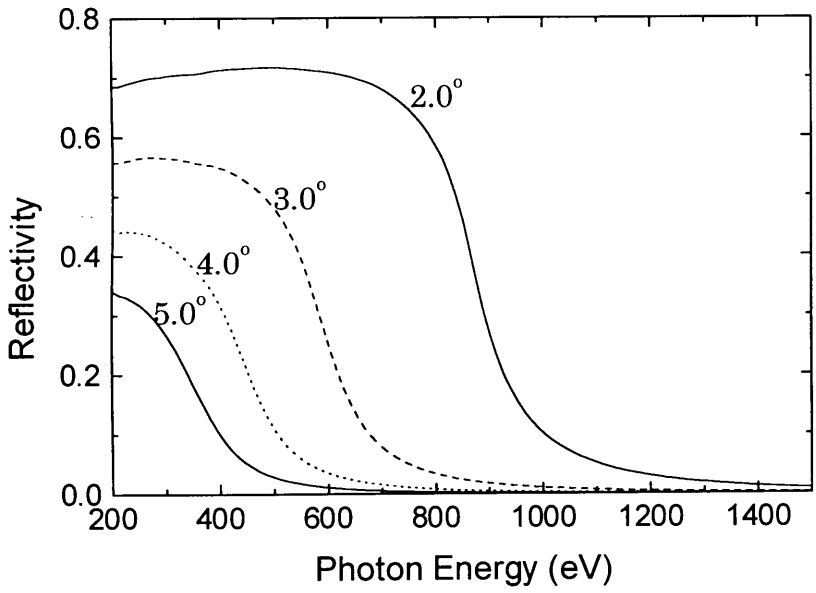

Fig. 3-20. Reflectivity of a Si-mirror as a function of the photon energy at the glancing angles of 2, 3, 4 and 5°.

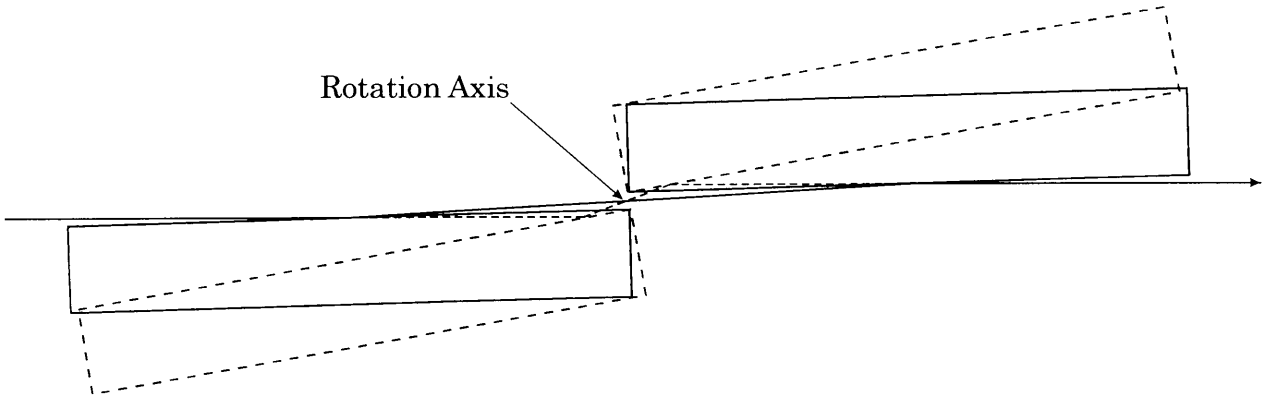

Fig. 3-21. Schematic diagram of the double mirror system Mw, illustrated at the glancing angle of 1.5 and 10°.

3-6-2. Performance of the double-mirror system

The incidence-angle dependence of the photon-flux distribution curves is shown in Fig. 3-22. It can be seen that, for instance at the glancing angle of 3.5°, the intensity is reduced to ~1/6 at 400 eV compared to that without Mw, while it becomes ~1/3000 at 800 eV. Therefore the second order (800 eV) rays at 400 eV can be suppressed to ~1/500 by inserting Mw at the glancing angle of 3.5°. An empirical relation between the glancing angle θ_m and the photon energy was determined from the reflectivity measurements:

$$\theta_m[\mathrm{deg}] = 1.22698 + 3.86309\exp\left(\frac{200 - E[\mathrm{eV}]}{275.53212}\right). \quad (3\text{-}12)$$

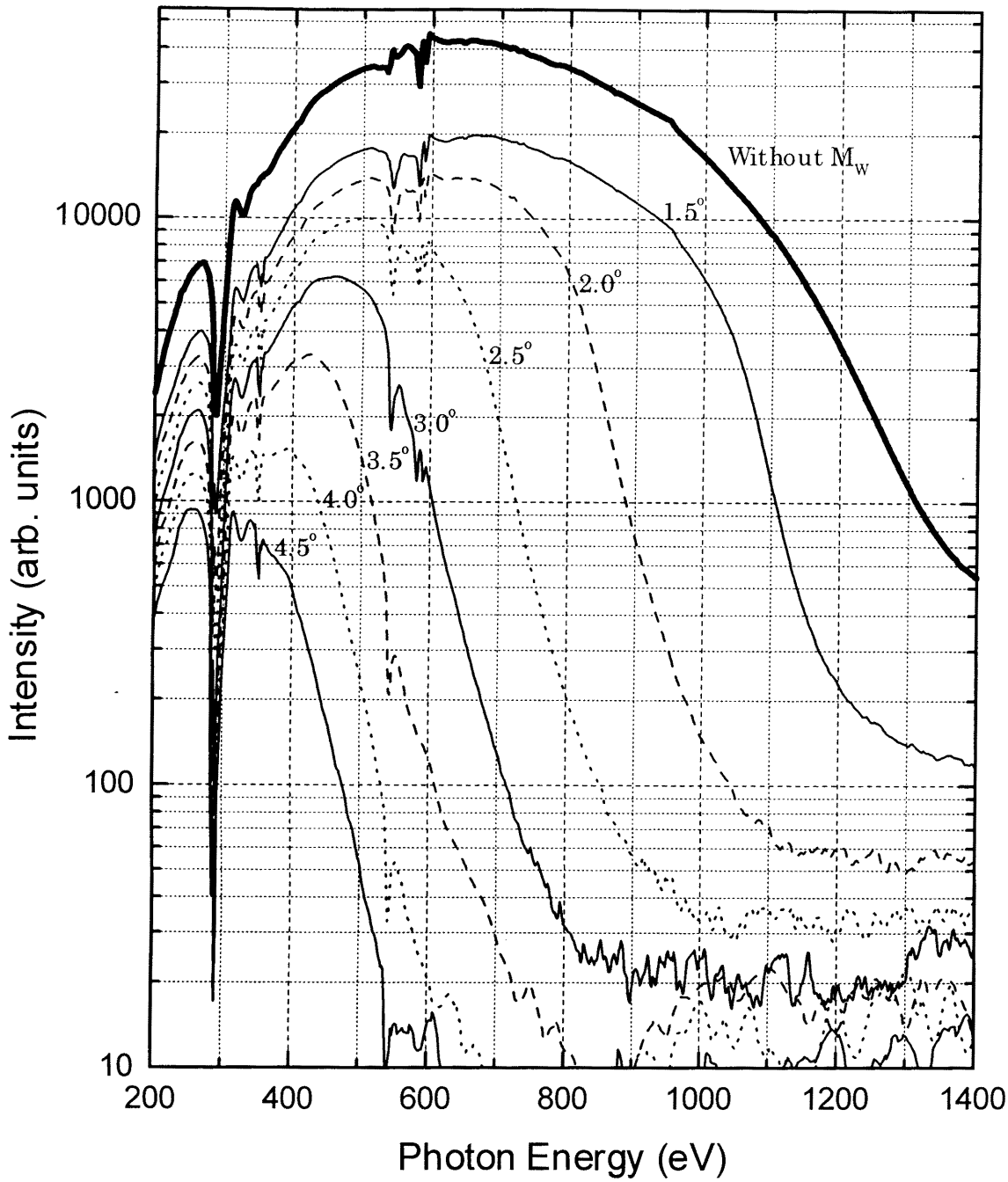

Fig. 3-22. Incidence-angle dependence of the photon-flux distribution with Si double-mirror system. The holographic grating and the spherical mirror M_2 were used. Note that the intensities are indicated in a logarithmic scale.

Figure 3-23 shows the photon-flux distribution when Mw is used at the glancing angle calculated from eq. (3-12), together with that when Mw is not inserted. Although the photon flux is reduced in the whole energy range, the prominent decreases can be seen at ~290 and ~530 eV, which are at the absorption edges of carbon and oxygen, respectively. These structures are attributed to the contamination on the Si mirrors, since Si is more reactive than the coating materials of other mirrors (Pt for Mo and Au for all other mirrors).

The harmonic-rejection property of the double-mirror system was checked by measuring the total-electron yield spectra for a Ni plate (Fig. 3-24). Without Mw, the Ni L edges are clearly seen at 420-440 eV, due to the contamination of the second order diffraction. On the contrary, no absorption structure can be seen in the same energy range when the double-mirror system is used, indicating that the higher spectral orders are efficiently removed.

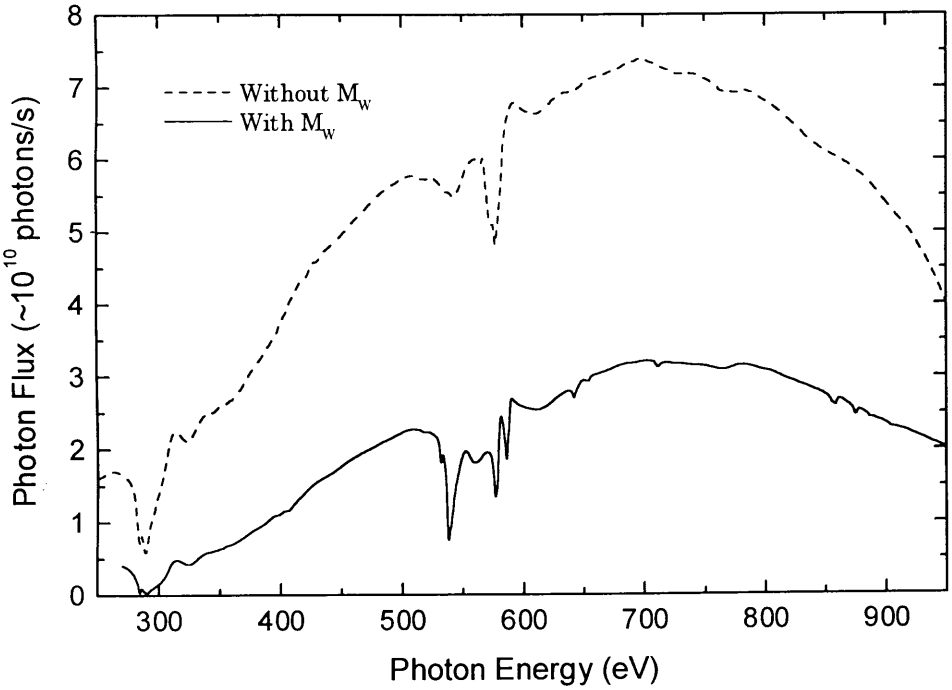

Fig. 3-23. Photon flux distribution obtained with Mw (solid line) at the glancing angles determined by eq. (3-12), together with that measured without Mw (dashed line).

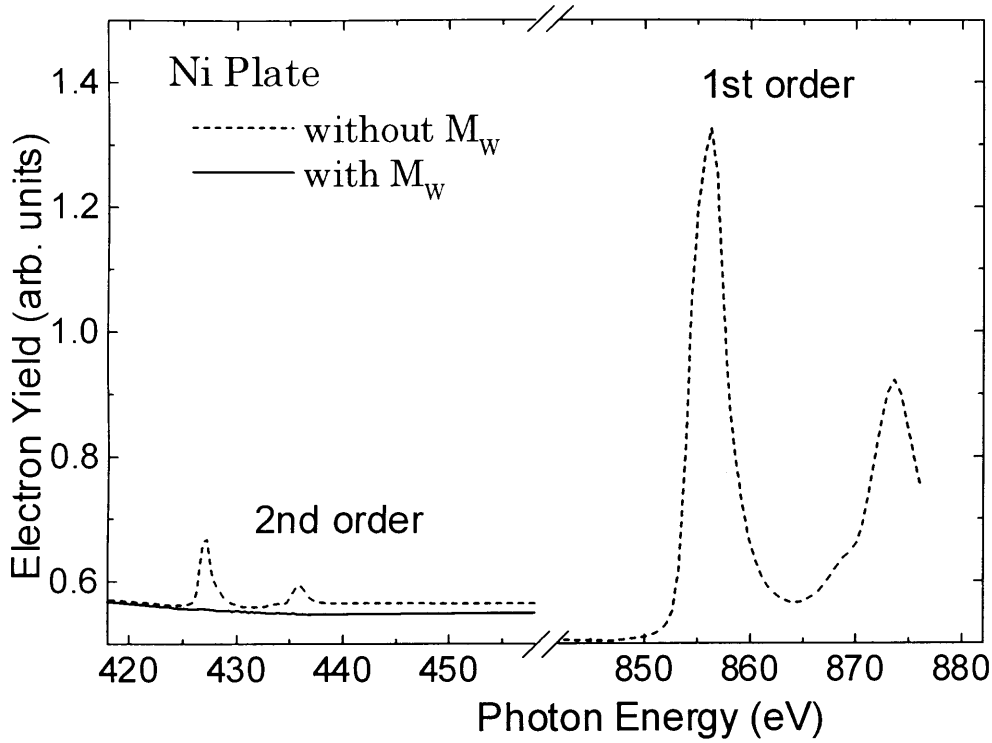

Fig. 3-24. Absorption spectra for a Ni plate obtained in the total electron yield mode with (solid line) and without (dashed line) the double-mirror system Mw.

3-6-3. Effects of the light purity

The purity of the monochromatized x rays is essential especially for the absorption measurements of dilute samples such as surface adsorbates. Figure 3-25(a) shows the photon-flux curve (I_0) and normalized partial electron yield spectrum (I/I_0) for atomic oxygen adsorbed on Ni(100), recorded by using the mechanically ruled grating and M_2 without Mw. Two sharp structure appearing in the I_0 curve at 575 and 585 eV are attributed to the absorption by Cr on the optical elements in the beamline. On the other hand, the higher spectral orders and the scattered rays are not reduced at these energies. Since the quantum yield depends on the photon energy and its dependence for I is different from that for I_0, the obtained intensity of I is not uniformly reduced as that of I_0 at these energies. This results in the ghost structures in the I/I_0 spectrum as shown in Fig. 3-25(a). In such a dilute sample whose signal-to-background ratio is typically 1/5 or less (note that the background are subtracted in the I/I_0 spectra in Fig. 3-25), this structure is never negligible.

In contrast, no artificial structures can be seen in the normalized absorption spectrum, I/I_0, in Fig. 3-25(b), which was taken with the holographic grating and Mw, in spite of the sharp structures at 575 and 585 eV in I_0. It was indicated that the quite high-purity light can be obtained with the holographic grating and Mw, owing to the low scattered light level and efficient reduction of the higher spectral orders.

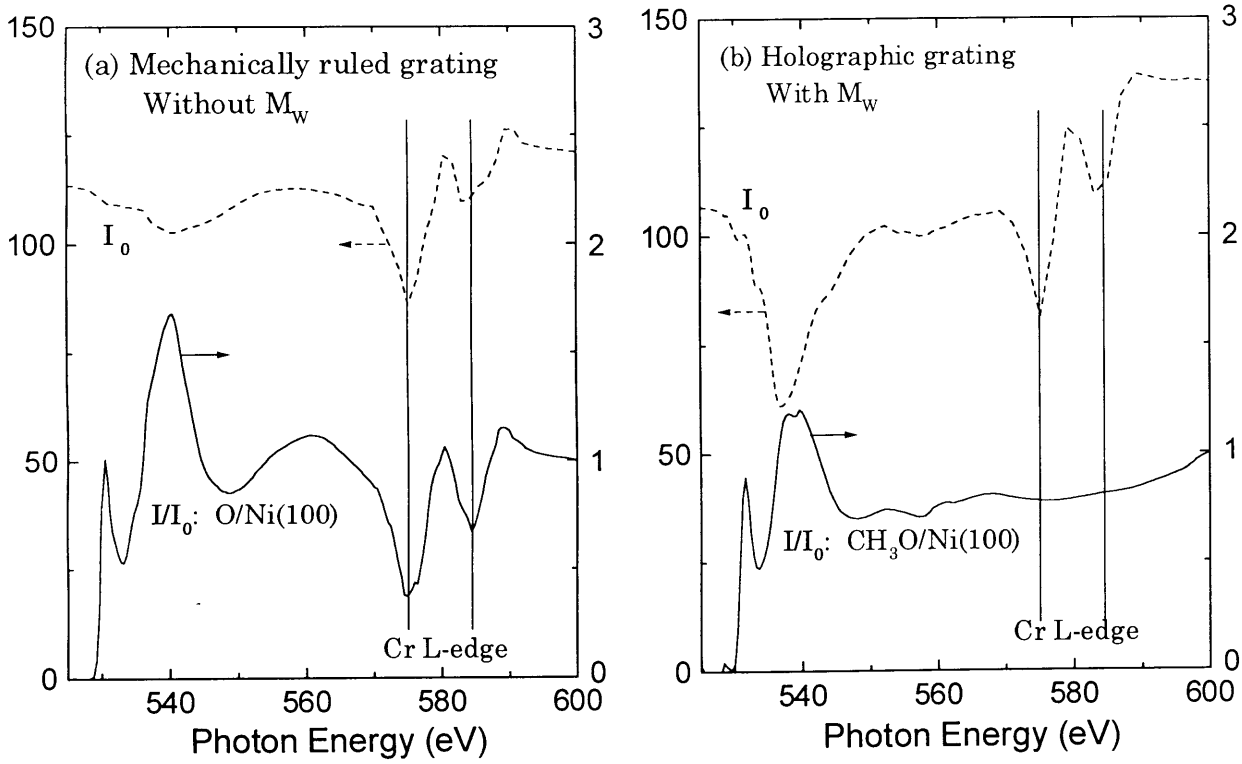

Fig. 3-25. Photon flux curves (I_0) and normalized partial electron yield spectra (I/I_0) for surface adsorbates, taken by using (a) mechanically ruled grating without Mw and (b) holographic grating with Mw. The spectra (I/I_0) are shown after the subtraction of the backgrounds and normalization at 600 eV.

3-7. Summary

I designed a Hettrick-type soft x-ray grazing incidence monochromator by using the light path function including the focusing spherical mirror as well as the VLS grating. It was indicated that the aberration arising from the spherical mirror is efficiently removed with the new design method and the resolving power of >5000 can be obtained. A holographic VLS grating was designed with aspheric wave-front holographic recording. It was found that the grooves are almost straight and that only the gradation of the groove densities along the centerline of the grating should be considered. Effects of errors in the recording parameters of the grating and the radius of the spherical mirror in the monochromator were estimated and possible ways to compensate for them were proposed.

An 800-*l*/mm holographic VLS grating as well as a mechanically ruled one were fabricated and tested in the newly constructed monochromator at a bending magnet source of the Photon Factory. After the proper alignments of the optical elements, the resolving powers of ~4500 and ~6900 were obtained for the holographic and mechanically ruled gratings, respectively. It was shown that the present holographic grating provides higher photon flux with a lower scattered light level compared to the mechanically ruled one. The monochromatized light can be obtained up to ~1800 eV with the holographic grating by exchanging the spherical mirror M_2 to M_1. The linear polarization factor was estimated to be ~95% from the angle dependence of the photo-ion intensity for the $1s \rightarrow \pi^*$ resonance absorption of molecular nitrogen.

A harmonic-rejection double-mirror system, Mw, was installed, where the incidence angles of the plane mirrors can be changed simultaneously with the energy scan. The higher spectral orders were efficiently removed with Mw by keeping the incidence angle properly during the energy scan. The quality of the partial electron yield spectra for the surface adsorbate was improved with the combination of the holographic grating and the double-mirror system, owing to the reduction of the scattered light and higher spectral orders.

References

[1] H. Petersen, C. Jung, C. Hellwig, W.B. Peatman and W. Gudat, Rev. Sci. Instrum. **66**, 1 (1995).

[2] C.T. Chen, Nucl. Instrum. Meth. A **256**, 595 (1987).

[3] E. Ishiguro, M. Suzuki, J. Yamazaki, E. Nakamura, K. Sakai, O. Matsudo, N. Mizutani, K. Fukui and M. Watanabe, Rev. Sci. Instrum. **60**, 2105 (1995).

[4] H.A. Padmore, Rev. Sci. Instrum. **60**, 1608 (1989).

[5] M.C. Hettrick, Nucl. Instrum. Meth. A **266**, 404 (1988).

[6] M.C. Hettrick, J.H. Underwood, P.J. Batson and M.J. Eckart, Appl. Opt. **27**, 220 (1988).

[7] M. Itou, T. Harada and T. Kita, Appl. Opt. **28**, 146 (1989).

[8] W. R. McKinny, Rev. Sci. Instrum. **63**, 1410 (1992).

[9] T.A. Callcott, W.L. O'Brien, J.J. Jia and Q.Y. Dong, Nucl. Instrum. Meth. A **319**, 128 (1992).

[10] M. Koike, R. Beguiristain, J.H. Underwood and T. Namioka, Nucl. Instrum. Meth. A **347**, 273 (1994).

[11] M. Koike and T. Namioka, Rev. Sci. Instrum. **66**, 2144 (1995).

[12] M. Koike and T. Namioka, J. Electron Spectrosc. Relat. Phenom. **80**, 303 (1996).

[13] J.J. Jia, J.H. Underwood, E.M. Gullikson, T.A. Callcott and R.C.C. Perera, J. Electron Spectrosc. Relat. Phenom. **80**, 509 (1996).

[14] H. Noda, Y. Harada and M. Koike, Appl. Opt. **28**, 4375 (1989).

[15] T. Namioka and M. Koike, Appl. Opt. **34**, 2180 (1995).

[16] Y. Harada, M. Koike and H. Noda, Shimadzu Hyoron, **44**, 83 (1988). (In Japanese.)

[17] M. Koike, Hoshako, **8**, 509 (1995). (In Japanese.)

[18] Y. Muramatsu, Y. Ohishi and H. Maezawa, KEK Internal **87-10**, National Laboratory for High Energy Physics, Tsukuba, Ibaraki 305, Japan (1988). (In Japanese.)

[19] M. Katoh and Y. Hori, KEK Report **92**, National Laboratory for High Energy Physics, Tsukuba, Ibaraki 305, Japan (1993). (In Japanese.)

[20] Y. Yan and A. Yagishita, KEK Report **95-9**, National Laboratory for High Energy Physics, Tsukuba, Ibaraki 305, Japan (1995).

[21] M. Watanabe, A. Toyoshima, Y. Azuma, T. Hayaishi, Y. Yan and A. Yagishita, Proc. SPIE **3150**, 58 (1997).

[22] A. Yagishita, H. Maezawa, M. Ukai and E. Shigemasa, Phys. Rev. Lett. **62**, 36 (1989).

Chapter 4

Oxygen *K*-edge x-ray-absorption fine-structure study of surface methoxy species formed on Cu(111) and Ni(111)

In this chapter, I describe the XAFS study of the atomic and electronic structures of the methoxy (CH_3O) adsorbate formed on Cu(111) and Ni(111). The XAFS measurements including NEXAFS (near-edge x-ray-absorption fine structure) and SEXAFS (surface extended x-ray-absorption fine structure) were performed at the newly constructed beamline. Thanks to the improved resolving power, it was shown that the C-O axis of the methoxy adsorbate is nearly perpendicular to the surface, which is different from the previous NEXAFS result. The C-O bond length of the species was also roughly estimated using the σ^*(C-O) resonance. A new peak was observed in the NEXAFS region also owing to the high resolution, and it was assigned to the transition from the O1*s* core to the 2*e* level of the methoxy species. It was found that the transition is noticeably stronger on Ni(111) than on Cu(111), indicating that the methoxy adsorbate on Cu(111) is more anionic. The adsorption site and O-Cu distance of the methoxy species on Cu(111) were determined from the SEXAFS analyses.

4-1. Introduction.

Much attention has been paid to the reactions of methanol with transition metal surfaces because of their importance in catalytic oxidation and methanol synthesis. On many metal surfaces such as Cu [1–13], Ni [6,14–24], Pt [25–27] and Pd [28,29], the formation of the rather stable methoxy intermediate has been found. As regards Cu(111), the methoxy species has been investigated using Fourier-transform reflection-absorption infrared spectroscopy[1], ultraviolet photoemission spectroscopy (UPS) [2,3], high-resolution electron energy loss spectroscopy (HREELS) [2], NEXAFS [3] and x-ray photoelectron diffraction (XPD) [4–6]. It was found that the methoxy species is formed by dosing the oxygen-precovered Cu(111) surface with methanol. All these experiments except for NEXAFS showed that the C-O axis of the methoxy species is perpendicular to the surface.

Figure 4-1 shows the previous NEXAFS data [3]. The tilt angle of the C-O axis was determined to be 28±10° from the surface normal, by analyzing the polarization dependence of the O1$s\rightarrow\sigma^*$(C-O) transition. On the contrary, the UPS data, which were also shown in the same paper, indicated the perpendicular C-O axis. They concluded that the orientation of the methoxy species could not be estimated properly with NEXAFS because of the superposition of higher-energy (~540 eV) resonances to the O1s$\rightarrow\sigma^*$(C-O) transition. Moreover, due to a poor energy

resolving power of the monochromator, the pre-edge features in the NEXAFS spectra were not clearly seen and they attributed the weak shoulder to the onset of the transition to continuum states (step structure). The pre-edge region is, however, important to discuss the chemical bonds between the adsorbate and substrate, and more careful investigation is necessary. The detailed surface structure of this system was investigated by XPD [5,6]. It was revealed that the oxygen atom locates on a "fcc" threefold follow site with the O-Cu distance of 1.97±0.04 Å and that the O-C bond length is 1.42 (–0.03/+0.10) Å. Here, "fcc" implies the threefold hollow site directly above the third-layer Cu atom.

The methoxy species on Ni(111) has been studied by UPS [14,16], temperature-programmed desorption (TPD) [14,17–19], HREELS [15], Fourier-transform infrared spectroscopy (FTIR) [20] and XPD [6,21]. It was found that methanol adsorbs molecularly below 140 K and is decomposed into a methoxy intermediate around 160 K. Some of these studies [6,14,16,21] concluded that the C-O axis of the methoxy species is perpendicular to the surface, while the others [15,20] indicated that it is tilted from the surface normal. The XPD studies [6,21] showed that the O-Ni and C-O distances are 1.93±0.04 Å and 1.44±0.05 Å, respectively, and that the oxygen atom adsorbs on the "fcc" threefold hollow site.

In the present study, higher-resolution O *K*-edge NEXAFS spectra were recorded for CH_3O on Cu(111), in order to re-analyze the orientation and to obtain more information about the electronic structure. The first NEXAFS measurements for CH_3O/Ni(111) were also performed and the results were compared with those for CH_3O/Cu(111). The orientation of the methoxy adsorbate was determined and the different chemical interactions of CH_3O with Cu and Ni were comparatively discussed. Moreover, O *K*-edge EXAFS of CH_3O/Cu(111) was measured and analyzed to determine the surface local structure and compared to the previous XPD studies.

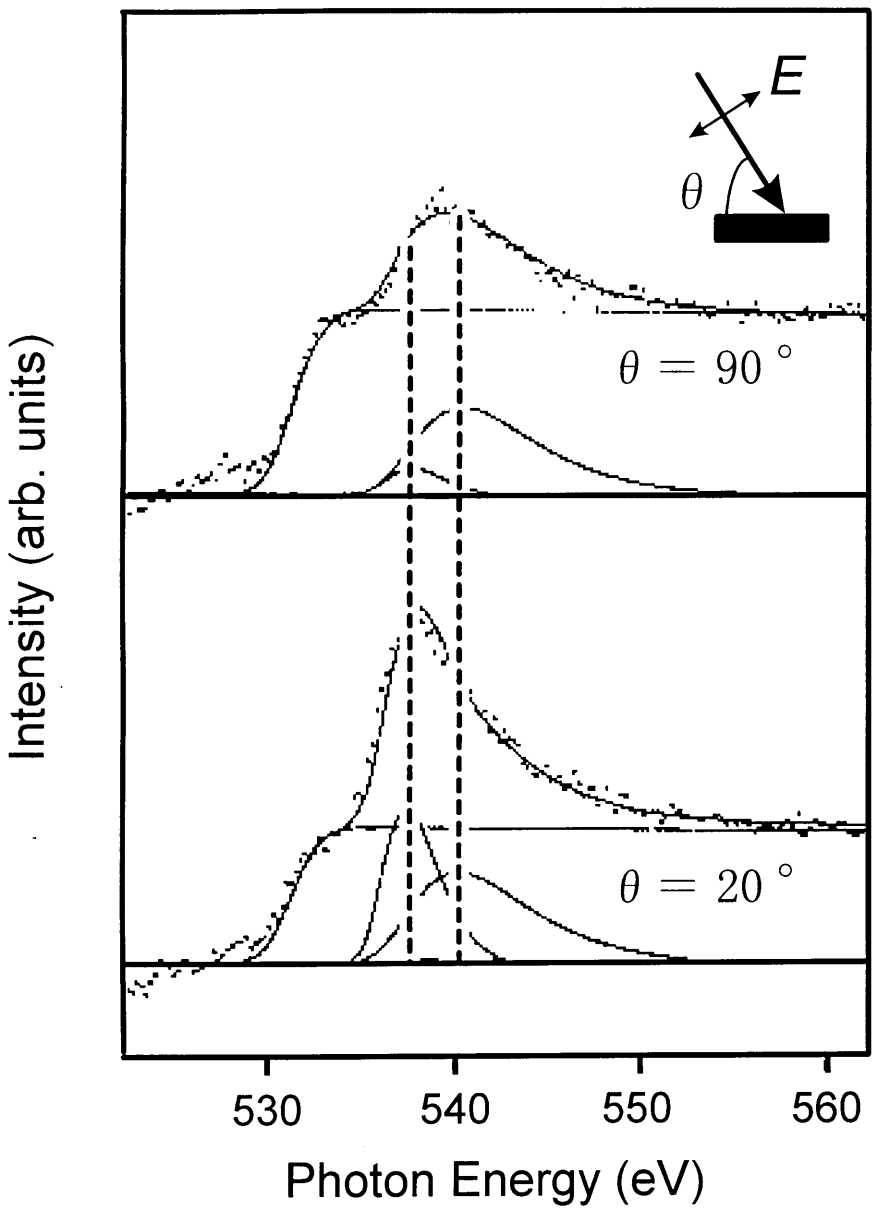

Fig. 4-1. Previous NEXAFS spectra of the methoxy species adsorbed on Cu(111) taken at the normal ($\theta = 90°$) and grazing ($\theta = 20°$) x-ray incidence angles.

4-2. Experimental

4-2-1. Experimental setup for the XAFS measurements

All the experiments were performed at the new beamline BL-11A, whose developments are described in the previous chapter. To obtain pure soft x-rays from 500 to 920 eV, I chose the combination of the holographic grating, the spherical mirror M_2 and the harmonic-rejection double-mirror system. The vertical acceptance and the entrance- and exit-slit widths were 0.2 mrad, 100 μm and 100 μm, respectively, providing a resolving power of 500–800 and a photon flux of $>10^{10}$ photons/s (see Fig. 3-23).

The geometry for the XAFS measurements is schematically illustrated in Fig. 4-2. A single crystal (3 mm thick and 12 mm in diameter) was mounted on the cryostat with a 0.4 mm-ϕ wire of the same material as the single crystal. Oxygen K-edge partial electron yield XAFS spectra were taken with a detector consisting of an 18-mm diameter microchannel plate (MCP) and two Au-coated W grids, which was placed just below the sample. A retarding voltage of –420 V was applied to the second grid (closer to the MCP), while the first one was grounded. Incidence angles θ of x-rays were 90° (normal incidence; an electric-field vector **E** parallel to the surface), 55° and 30° for the NEXAFS experiments, while those were 90° and 30° for the SEXAFS measurements.

For the spectral normalization, the electron yield spectra of the clean surface at the same incidence angles were separately measured for the same energy region in a similar manner and were used as I_0. The calibration of the absolute photon energy was conducted with the accuracy of 0.5 eV by measuring a total ion yield spectrum of gaseous oxygen, assuming that the O1$s\rightarrow\pi^*$ resonance appears at 532.0 eV. The relative photon energy was calibrated with the precision of 0.1 eV using absorption structures of oxygen contamination on mirrors, appearing in the transmission function measured by a Au-coated W mesh placed at the upstream of the sample.

4-2-2. Sample preparation

A Cu(111) single crystal was cleaned in an ultrahigh vacuum (UHV) chamber (base pressure less than 1×10^{-8} Pa) with successive cycles of Ar^+ bombardment, O_2 treatment and annealing at 900 K. Sample annealing was performed by electron bombardment from the rear side of the crystal and the temperature was monitored with a chromel-alumel thermocouple. The cleanliness and order of the surface were confirmed by NEXAFS, XPS (x-ray photoemission spectroscopy) and LEED (low-energy electron diffraction). The surface was then dosed with oxygen at room temperature, followed by methanol exposure at 200 K. Excess methanol and water produced by surface chemical reaction were, if any, removed by subsequent heating to 250 K. To avoid the

electron-stimulated decomposition of methanol or the methoxy species, the sample heating was performed by an UHV-compatible infrared heater.

A clean Ni(111) single crystal surface was prepared in a similar manner to Cu(111). In order to form methoxy species, two different methods were found to be applicable. According to the previous literatures [14–21], a clean Ni(111) crystal was dosed with methanol at <140 K, and the sample was subsequently heated to 160–240 K, this leading to CH_3O/Ni(111). An alternative way is to dose the clean surface with methanol at 200 K. Both methods were found to provide identical O *K*-edge NEXAFS spectra. In addition, multilayer methanol was formed on Ni(111) as a reference, by dosing the surface with methanol at 140 K.

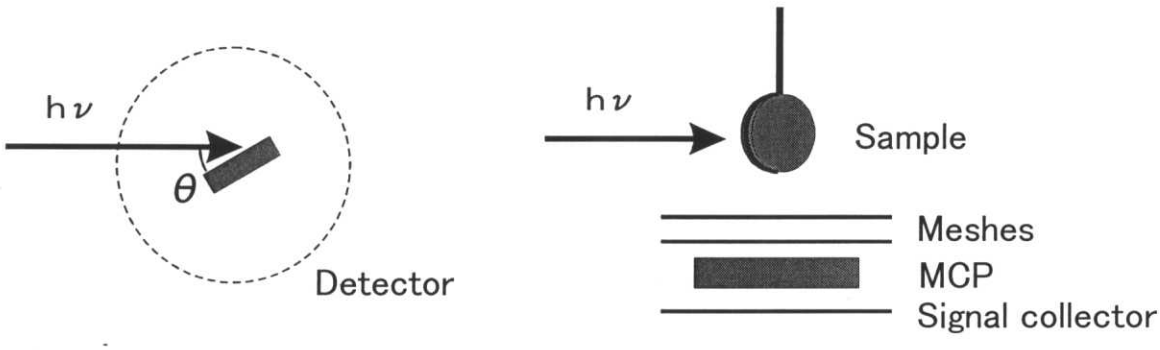

Fig. 4-2. Schematic top view (left) and side view (right) of the experimental setup for the XAFS measurements.

4-3. Results and discussion

4-3-1. NEXAFS

Figure 4-3(a) shows the NEXAFS spectra taken after dosing Cu(111) with 200 L (1×10^{-6} Torr, 200 s) molecular oxygen at room temperature. After subsequent dosing with 1 L (5×10^{-8} Torr, 20 s) methanol at 200 K followed by heating the sample to 250 K, the spectra are changed as shown in Fig. 4-3(b). Sharp peaks are observed at 529.8 and 533.3 eV for O/Cu(111) in the grazing incidence configuration (θ = 30°), while they almost completely disappear according to the formation of the methoxy species. This implies that atomic oxygen is removed from the surface. This finding was also supported by the O1*s* XPS; a single peak was observed for CH_3O/Cu(111) at a higher binding energy by 1.2 eV than O/Cu(111). The edge jump (O-*K* electron yield intensity at the high-energy region, which is proportional to the amount of oxygen) for the methoxy species (b) is about two times of magnitude larger than that for the atomic oxygen (a). This suggests that the following reaction occurrs on the Cu(111) surface:

$$2CH_3OH + O\ (ad) \rightarrow 2CH_3O\ (ad) + H_2O.$$

It has been reported that this reaction also occurs on the Cu(110) surface [13].

The polarization-dependent NEXAFS spectra for the methoxy species on Cu(111) and Ni(111) are shown in Fig. 4-4, together with the normal-incidence spectrum for multilayer methanol. The methoxy adsorbate and multilayer methanol on Ni(111) were obtained by dosing the surface with 2 L (5×10^{-8} Torr, 40 s) and 3 L (5×10^{-8} Torr, 60 s) methanol at 200 and 140 K, respectively. Since no polarization dependence was observed for multilayer methanol, only the normal incidence spectrum is shown. There are three prominent peaks labeled A, B and C, in the NEXAFS spectra for the methoxy species both on Cu(111) and Ni(111). These peaks appear at about 531.5, 536.5, and 538.5 eV for CH_3O/Cu(111) [Fig. 4-4(a)], while they are observed at about 531.5, 537.5, and 540.5 eV for CH_3O/Ni(111) [Fig. 4-4(b)]. The lowest-energy peak (A) is worthwhile discussing in detail because it has not been observed clearly in the previous NEXAFS study [3] on Cu(111), as shown in Fig. 4-1. Since the previous spectra were taken with a lower energy resolution, the feature appeared only as a broad shoulder. One may assign peak A to the π^* resonance from other species such as formaldehyde and CO. The σ^* resonance of these species should, however, appear at higher photon energies than any peak observed in the spectra for the methoxy adsorbate; for instance, the σ^* resonance of CO appears at ~550 eV [30]. The other possible origin of this peak may be the atomic oxygen remaining on the surface. It should be noted, however, that the peaks observed for O/Cu(111) are prominent in the grazing incidence configuration (θ = 30°) as can

be seen in Fig. 4-3, while peak A is enhanced at normal incidence. The first peak can be thus attributed to the methoxy adsorbate.

According to the previous molecular-orbital (MO) calculations for the methoxy species [2,31–34], the highest occupied molecular orbitals $2e$ of the methoxy anion is largely of oxygen p-type lone pair mixed with some C-O antibonding π^*, as illustrated in Fig. 4-5. If the methoxy species were completely anionic on the surfaces, the $2e$ orbitals would be filled and no transition to this level could be observed at all. The effective electron population of the $2e$ orbitals for the methoxy species on Cu(111) was, however, calculated to be 3.6 [2], indicating that the 2e orbitals are not fully occupied. Thus the peak is consequently attributed to the transition of $O1s \rightarrow 2e$. According to this interpretation, it is quite natural that this peak was not observed for multilayer methanol [Fig. 4-4(c)] since molecular methanol has no such unfilled orbital. It should be noted

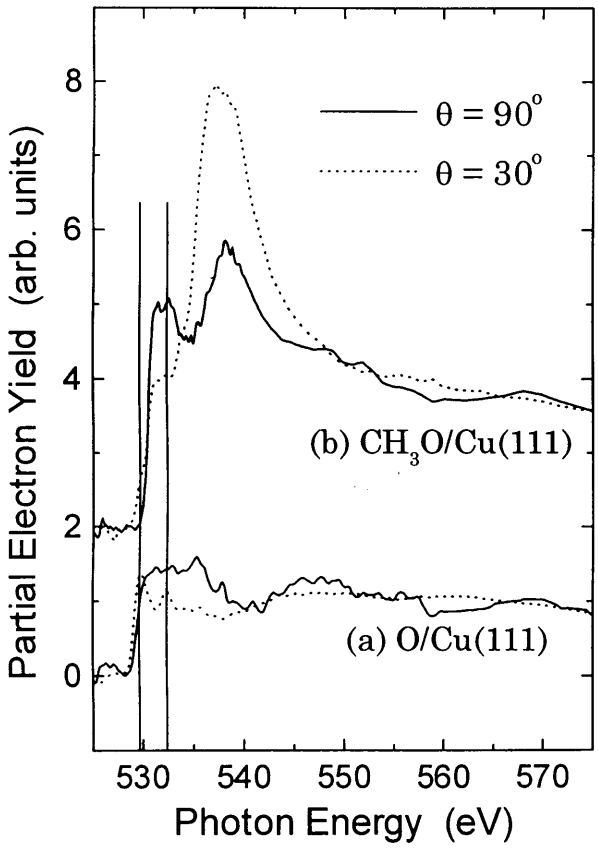

Fig. 4-3. O K-edge NEXAFS spectra taken after (a) dosing Cu(111) with 200 L oxygen at room temperature and (b) subsequent dosing with 1 L methanol at 200 K followed by eating to 250 K. Two lines are inserted at 529.8 and 533.3 eV.

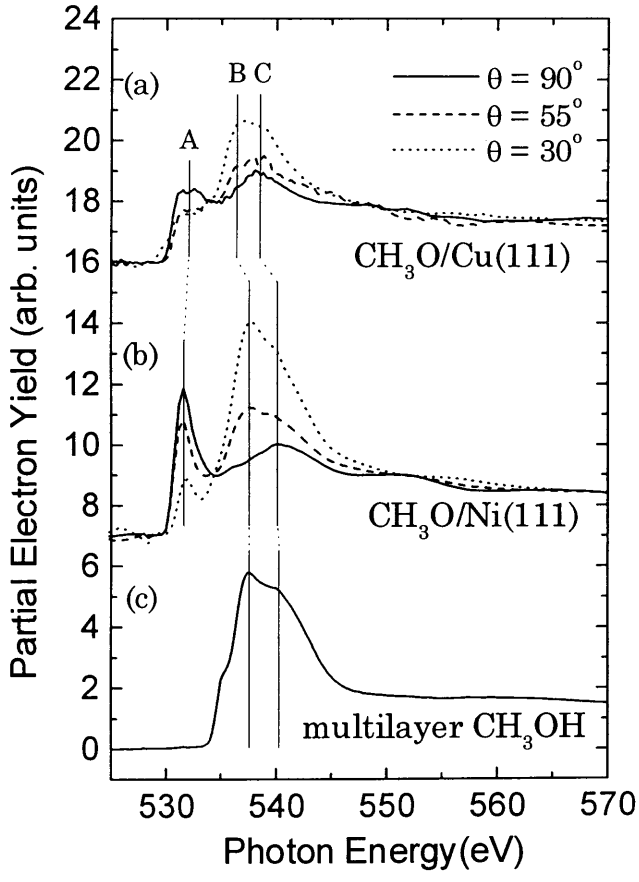

Fig. 4-4. Polarization-dependent O K-edge NEXAFS spectra for (a) CH_3O/Cu(111) and (b) CH_3O/Ni(111) together with (c) the normal-incidence spectrum for multilayer methanol on Ni(111). The spectra were normalized with the edge jumps.

that the $1s \rightarrow 2e$ resonance is more prominent on Ni(111) than Cu(111). This implies that the vacancy of the $2e$ orbitals of the methoxy species is larger on Ni(111) compared to Cu(111). Namely, more covalent bonding is formed between oxygen and Ni(111) due to the stronger $2e$-$3d$ interaction, while the methoxy adsorbate is more anionic on Cu(111). This consequence is consistent with the previous calculations; on Ni(111) the bonding of methoxy to the surface is characterized as a combination of the ionic and covalent bonds [34], while it is almost ionic on Cu(111) [2]. Moreover, a similar tendency, *i.e.* the stronger π-type ($2e$-$3d$ in the present study) interaction for Ni compared to Cu, is also implied in the previous NEXAFS works for the molecular SO_2 adsorbed on Ni and Cu surfaces [35,36]. This trend can be explained with the high density of state around the Fermi level for the Ni $3d$ band, in contrast to the case of Cu. Since such d electrons in shallow levels interact significantly with the adsorbates, the π-type covalent bonding is enhanced on Ni compared to Cu. Unfortunately, in the present study, the amount of charge transfer could not be estimated due to the lack of reference chemical species whose vacancy of the $2e$ orbitals is known.

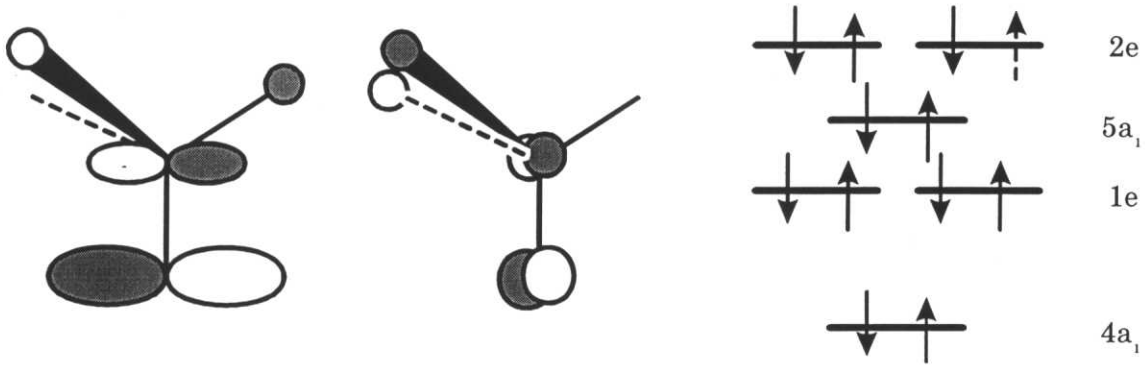

Fig. 4-5. Schematic energy diagram for the methoxy species (right) and molecular orbital views of the degenerated $2e$ orbitals (left) [2,31–33].

The second peak (B) can be assigned to the transition from O1s to the $6a_1$ orbital, which has mainly σ^*(C-O) character. The third one (C) may come from the transition to the $3e$ and $7a_1$ levels, possibly superimposed with multiple scattering events [3,9,10]. The superposition of the extra peak to the σ^* resonance is a common feature of the NEXAFS spectra for the methoxy adsorbate on Cu(111) and Ni(111) [Figs. 4-4(a) and 4-4(b)] as well as on the Cu(100) surface [9,10], even for multilayer methanol [Fig. 4-4(c)].

In order to obtain the orientation angle of the methoxy species on Cu(111) and Ni(111), the polarization dependence of the NEXAFS spectra was analyzed. Each spectrum was deconvoluted with asymmetric Gaussian functions and an error function, corresponding to the step structure [30]. The fitting results are depicted in Fig. 4-6. Deconvoluted peaks are located at 531.3, 536.2 and 538.5 eV for CH_3O/Cu(111) and at 531.7, 537.3 and 540.5 eV for CH_3O/Ni(111). The σ^*(C-O) resonance (O1s→6a_1 transition) can be separated from the third peak (C) thanks to the higher energy resolution in the present spectra. The σ^* resonance disappears almost completely in the normal incidence spectrum ($\theta = 90°$) for both on Cu(111) and Ni(111), suggesting that the methoxy species adsorbs with its C-O axis perpendicular to the surfaces.

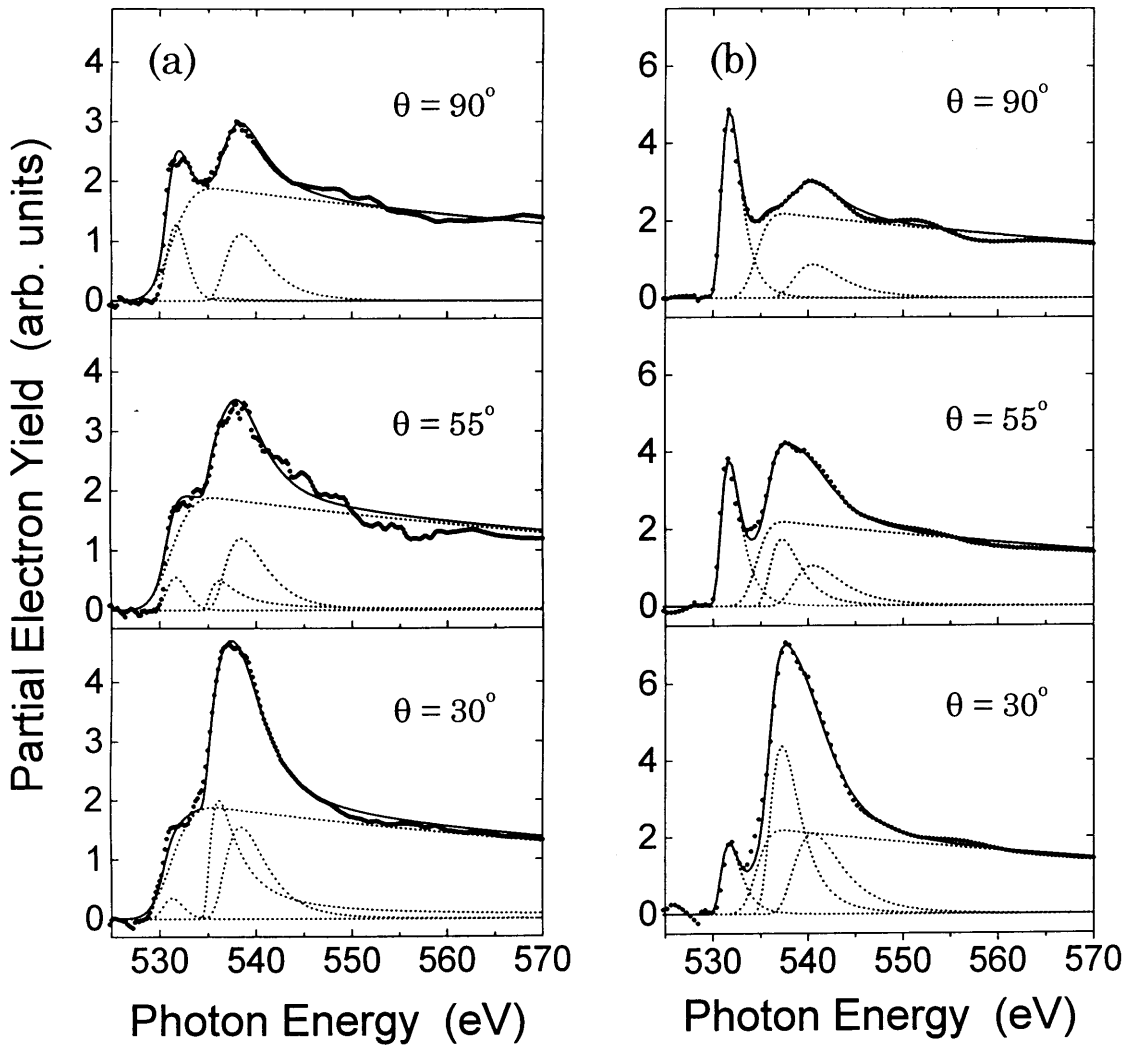

Fig. 4-6. Curve fittings for the polarization-dependent NEXAFS spectra of (a) CH_3O/Cu(111) and (b) CH_3O/Ni(111). Three asymmetric Gaussian functions and an error function were used in the fitting procedure for each spectrum.

The polarization dependence of the $2e$ and $\sigma^*(6a_1)$ resonance intensities for CH_3O/Cu(111) are shown in Fig. 4-7, together with the calculated relative intensities for the cases that the C-O axis is tilted by 0, 10 and 20° from surface normal. In the calculation of the intensities, it was assumed that the transition moment for the $2e$ and σ^* resonances are perpendicular and parallel to the C-O axis, respectively, neglecting the modification of the MO characters upon adsorption. Large errors in the intensities of the $2e$ resonance could not be avoided due to the overlapping of the step function. Moreover, the $2e$ orbital could be influenced by the Cu surface, the orbital participates in the direct chemical bonding with the substrate because as noted above. On the other hand, the σ^*(C-O) orbital tends to be rather localized within the C-O bond region and be affected only slightly by the substrate. Accordingly, using the results concerning the σ^* resonance, the orientation angle of the C-O axis can be estimated to be 0±20° from the surface normal. In a similar manner, the angle of the molecular axis of the methoxy adsorbate on Ni(111) was determined to be also 0±20°. Note here that, in principle, the tilt angle of 0° cannot be obtained when the molecule is wagging or randomly oriented around the surface normal, as discussed in §2-1-2. In other word, the molecule is oriented to the surface normal without any wagging, if the measured polarization dependence curve matches to the calculated one for the perpendicular molecule. The obtained angles have, however, some uncertainties in practice. Thus the present result, 0±20°, should be interpreted that the C-O axis of the methoxy species is likely oriented around normal to the surface and it can be tilted from or wagging around the surface normal by about 0–20°.

The C-O distance in the methoxy adsorbate can be roughly estimated from the peak position of the σ^*(C-O) resonance [30,39], as described in §2-1-2. In the present study, the σ^* transition for CH_3O/Cu(111) was found to peak at a lower energy by 1.2 eV than that for multilayer methanol. This indicates that the C-O distance of the methoxy adsorbate is slightly longer than that of solid methanol (1.43 Å [40]). Assuming a linearity between the resonance energy and the bond length verified for several molecules containing C-O bonds [30,39], the C-O distance was estimated to be 1.46±0.05 Å. On the contrary, the σ^*(C-O) resonance for CH_3O/Ni(111) appears at almost the same energy as that for multilayer methanol, indicating the C-O distance of 1.43±0.05 Å. Here the error of 0.05 Å was estimated from the uncertainty in the empirical relationship between the bond length and the peak position of the σ^*(C-O) resonance [30]. As for the bond-length difference between the methoxy species on Cu(111) and Ni(111), the uncertainty is likely to be rather small, since the same species (CH_3O) are compared. Although the error may arise from the chemical shift and/or relaxation effects, the $1s\rightarrow 2e$ peak position should be shifted if such effects are significant [30]. The $1s\rightarrow 2e$ transition was, however, observed at almost the same energy on both surfaces. Accordingly, the C-O distances of the methoxy species on Cu(111) and Ni(111) seem to be different from each other. The bond-length difference, if it really exists, is in

accordance with the charge transfer to the $2e$ orbital: since the occupancy of the $2e$ level, which has some antibonding character, is noticeably larger on Cu(111) than Ni(111), it is reasonable that the C-O distance of the methoxy adsorbate on Cu(111) is longer than that on Ni(111). The results of the NEXAFS analyses are summarized in Table 4-1.

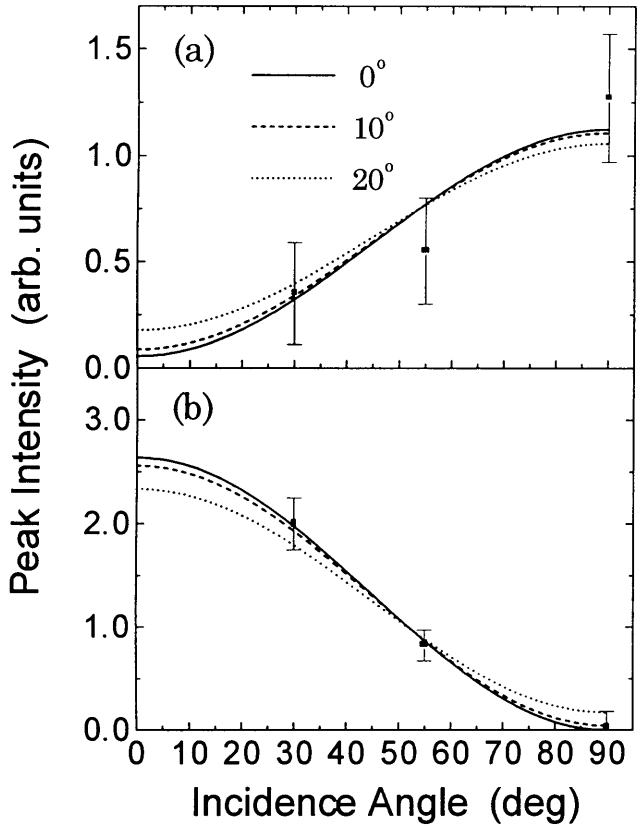

Fig. 4-7. (a) Polarization dependence of the O1s→$2e$ transition intensity of the methoxy adsorbate and (b) that of the σ^*(C-O) resonance ($1s$→$6a_1$), together with the calculated dependence for tilt angles of 0, 10 and 20°.

Table 4-1. Summary of the O *K*-edge NEXAFS analyses for the methoxy species on Cu(111) and Ni(111) together with those of multilayer CH_3OH.

	CH_3O/Cu(111)	CH_3O/Ni(111)	multilayer CH_3OH
Peak position (eV)			
Peak A (1s→2e)	531.3	531.7	
Peak B (1s→σ*)	536.2	537.3	537.4
Peak C	538.5	540.5	540.6
Occupancy of the 2*e* orbital	larger	smaller	
C-O bond length (Å)	1.46±0.05	1.43±0.05	(1.43 [40])
C-O axis orientation	perpendicular	perpendicular	random

4-3-2. SEXAFS for CH_3O/Cu(111)

Figure 4-8 shows the O *K*-edge EXAFS spectra for CH_3O/Cu(111) taken at the x-ray incidence angles of 90° and 30°. The EXAFS spectra can be measured up to ~920 eV, at which a strong Cu *L*-edge absorption occurs. Extraction of the EXAFS function $k\chi(k)$ (k is the wavenumber of the photoelectron) was carried out following the well-established procedures: pre- and post-edge background subtraction and subsequent normalization assuming the constant atomic absorption coefficients [41,42]. Figures 4-9 and 4-10 show extracted EXAFS functions and their Fourier transforms (Δk_{FT} = 2.35–9.90 Å^{-1}), respectively. The main peak around 1.8 Å in Fig. 4-9 arises from the nearest-neighbor Cu atoms. The curve-fitting analyses in k space were carried out after Fourier filtering of the peak (ΔR = 1.25–2.25 Å) and subsequent inverse Fourier transformation, using a theoretical standard given by FEFF6 [43]. In the present analysis, anharmonic correction term in the phase part has been neglected and Gaussian distribution for the O-Cu bond was assumed. We obtained the O-Cu bond length R of 2.00±0.03 Å and the edge energy E_0 of 536.6 eV, while the EXAFS Debye-Waller factor C_2 was 6.5×10^{-3} Å^2.

The ratio of the effective coordination numbers $N^*(\theta)$ between 90 and 30°, $N^*(90°)/N^*(30°)$, was resultantly obtained as 0.71±0.08. The ratio is compared with the calculated values for typical adsorption geometries assuming no lateral movements of the first-layer Cu atoms: 0.670 for the threefold hollow site, 0.422 for the bridge, and 0.000 for the atop. It can be concluded that the oxygen atom locates on the threefold hollow site. The lateral displacement of the first-layer Cu

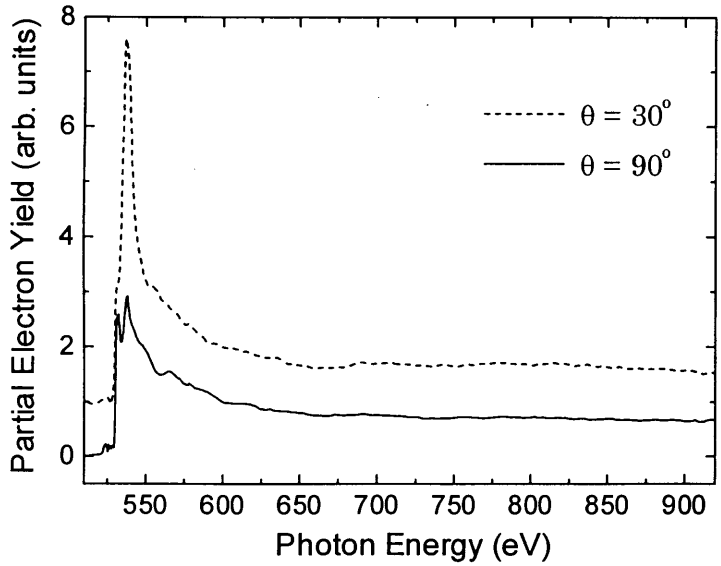

Fig. 4-8. O *K*-edge EXAFS spectra of CH_3O/Cu(111) taken at 30 and 90° x-ray incidence angles.

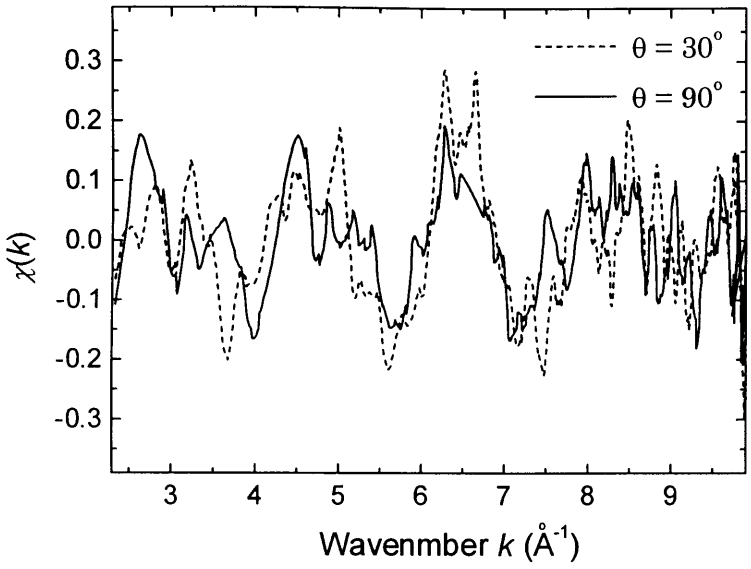

Fig. 4-9. O *K*-edge EXAFS oscillation functions $k\chi(k)$ of CH_3O/Cu(111).

atom was estimated from the ratio of $N^*(\theta)$ to be 0.03±0.05 Å. Note that the amplitude reduction factor S_0^2 was estimated to be 0.69 for 90° and 0.65 for 30°, which are typical values for the O *K*-edge EXAFS. This indicates the reasonable analyses for the normalization procedure.

Although the signal-to-noise (S/N) ratio of the obtained EXAFS data is not quite high, I tried to obtain more information about the adsorption site. Figure 4-11(a) gives simulated EXAFS spectra for the "fcc" hollow site adsorption of the methoxy species, while those for the "hcp" hollow are shown in Fig. 4-11(b). The clear difference between these two adsorption sites can be found in the grazing incidence spectra. A significant peak should be observed at ~3.4 Å in the Fourier transform, if the methoxy species locates on the "fcc" hollow site. On the other hand, the expected peak position for the "hcp" adsorption is not ~3.4 Å but ~4.0 Å. In the Fourier transform of the measured EXAFS (Fig. 4-10), two peaks can be observed at ~3.5 and ~4.1 Å. This may suggest the co-existence of both the "fcc" and "hcp" hollow adsorption. It is, however, difficult to conclude which site is (or mixture of them are) occupied, since the S/N ratio of the data is not so good.

The surface structure of the methoxy adsorbate on Cu(111) obtained from the SEXAFS and NEXAFS results is schematically shown in Fig. 4-12.

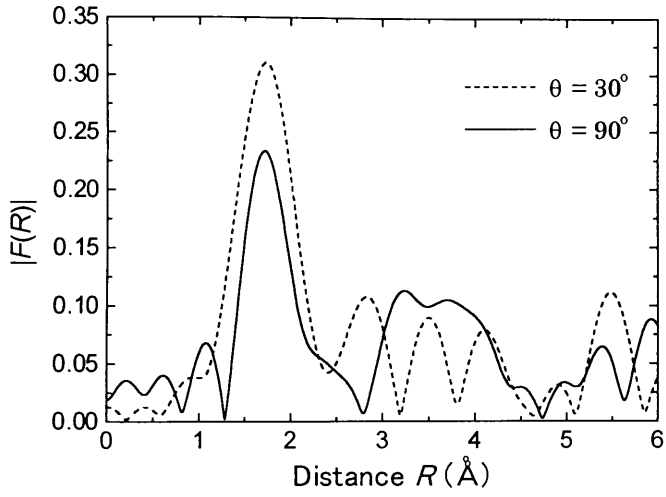

Fig. 4-10. Fourier transforms of $k\chi(k)$ for $CH_3O/Cu(111)$ shown in Fig. 4-10.

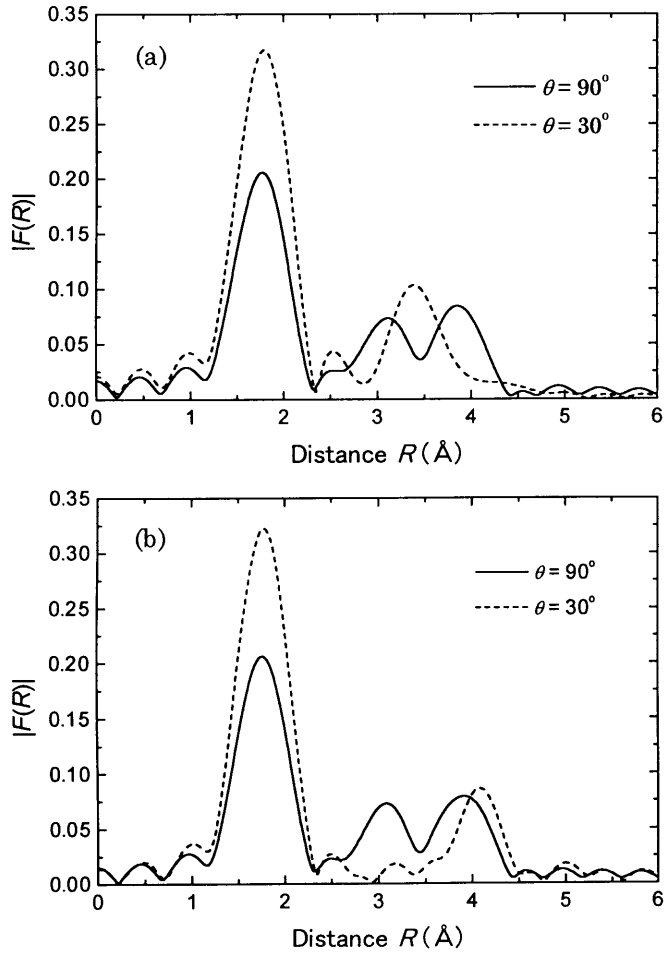

Fig. 4-11. Fourier transforms of simulated $k\chi(k)$ for $CH_3O/Cu(111)$ adsorbed at (a) "fcc" and (b) "hcp" hollow sites.

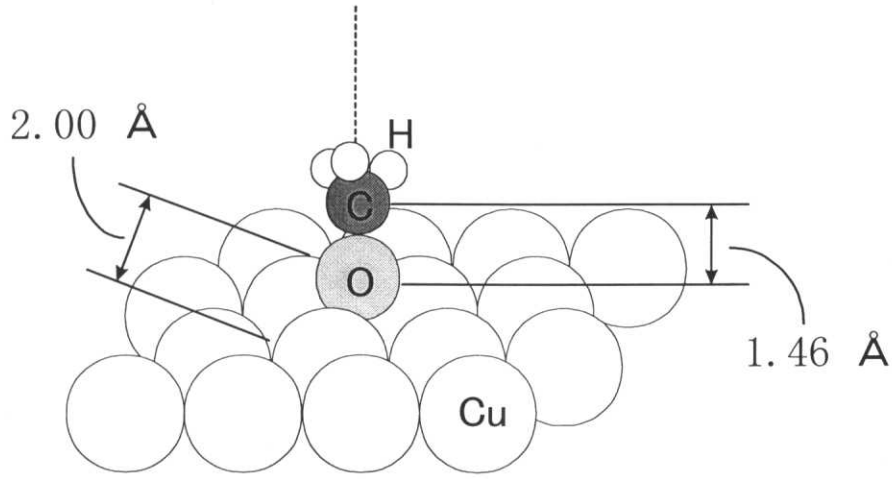

Fig. 4-12. Schematic view of the surface structure model for CH_3O/Cu(111).

4-3-3. Comparison with the previous works

The obtained orientation of the methoxy species on Cu(111) is in good agreement with previous experiments [1-6] except for the NEXAFS study [3]. The previous NEXAFS analysis concluded that the C-O axis is inclined by 28±10°, while FT-RAIRS [1], UPS [2,3], HREELS [2] and XPD [4-6], as well as the present study, indicated the perpendicular C-O axis. The contradiction between the previous and present NEXAFS studies may come from the difference in the spectral resolution. As regards Ni(111), the present work indicated that the C-O axis of the methoxy adsorbate is also perpendicular to the surface, which is consistent with the previous UPS [14,16] and XPD [6,21] studies. Although the vibrational spectroscopies (HREELS [15] and FTIR [20]) implied the tilted methoxy species, it has been suggested by a study of a fully deuterated methoxy species on Mo(110) [44] that the vibrational data on Ni(111) could be interpreted by assuming the perpendicular methoxy species.

The structural parameters obtained for CH_3O/Cu(111) and CH_3O/Ni(111) are summarized in Table 4-2, together with those determined from the XPD measurements. The O-Cu and C-O distances were determined by XPD [5,6] to be 1.97±0.04 Å and 1.42(–0.03/+0.10) Å, respectively, which are close to the values obtained here (2.00±0.03 Å and 1.46±0.05 Å). The XPD work also showed that the oxygen atom locates on the "fcc" hollow site, which is consistent with the present result, though the coexistence of the "hcp" hollow site may be suggested by the present SEXAFS data. No significant lateral distortion was detected both by XPD and the present work. The threefold hollow site adsorption and the perpendicular orientation of the C-O axis also correspond with the *ab initio* calculations [2,31,32,38]. The obtained C-O bond length

(1.43±0.05 Å) is also almost identical to the one determined by XPD measurements (1.44±0.04 Å) [6,21].

Table 4-2. Summary of the structural parameters for the methoxy species on Cu(111) (upper columns) and Ni(111) (lower columns) obtained from the XAFS and XPD [5,6,21] measurements.

	XAFS	XPD
O-Metal distance	2.00±0.03	1.97±0.04
	–	1.93±0.04
Adsorption site	Hollow	"fcc" hollow
	–	"fcc" hollow
Lateral distortion of first metal layer	0.03±0.05	0.01±0.05
	–	0.10±0.06
C-O distance	1.46±0.05	1.42(–0.03/+0.10)
	1.43±0.05	1.44±0.05
C-O orientation	Perpendicular	Perpendicular
	Perpendicular	Perpendicular

4-4. Summary

The O *K*-edge XAFS apectra for the methoxy adsorbate on Cu(111) and Ni(111) were measured with the newly developed soft x-ray beamline. It was demonstrated that higher resolution NEXAFS measurements can determine the orientation of the methoxy species properly on both the Cu(111) and Ni(111) surfaces and provide further information for the electronic structure of the species. The geometrical parameters of the species obtained from XPD [5,6,21] were successfully checked with the SEXAFS measurements.

The formation of the methoxy species on the oxygen-precovered Cu(111) and clean Ni(111) surfaces has been observed and the surface structures of the species were determined. The transition from the O1*s* core to the partially filled 2*e* levels having some C-O π^* character was observed in the NEXAFS spectra for the methoxy adsorbate, suggesting that the species is not completely anionic. It was also suggested, from a comparison between the methoxy species on Cu(111) and Ni(111), that the species is more anionic on the Cu(111) surface than on Ni(111). The polarization-dependent NEXAFS spectra showed that the C-O axis of the methoxy adsorbate is almost perpendicular to the surface on both Cu(111) and Ni(111). The C-O distances of the methoxy species on Cu(111) and Ni(111) were roughly estimated to be 1.46±0.05 Å and 1.43±0.05 Å, respectively. The difference in the bond length can be related to that in the occupancy of the 2*e* orbital, which has some antibonding character. From the analysis of the EXAFS spectra for CH_3O/Cu(111), it was found that the oxygen atom in the methoxy species locates on the threefold hollow site and the distance between oxygen and the nearest-neighbor Cu atom is 2.00±0.03 Å. No significant lateral distortion of the surface Cu atoms was detected.

References

[1] M.A. Chesters and E.M. McCash, Spectrochim. Acta A **43**, 1625 (1987).

[2] M. Witko, K. Hermann, D. Ricken, W. Stenzel, H. Conrad, and A.M. Bradshaw, Chem. Phys. **177**, 363 (1993).

[3] D.E. Ricken, J. Somers, A.W. Robinson, and A.M. Bradshaw, Faraday Discuss. Chem. Soc. **89**, 291 (1990).

[4] A.V. de Carvalho, M.C. Asensio, and D.P. Woodruff, Surf. Sci. **273**, 381 (1992).

[5] Ph. Hofmann, K.-M. Schindler, S. Bao, V. Fritzsche, D.E. Ricken, A.M. Bradshaw, and D.P. Woodruff, Surf. Sci. **304**, 74 (1994).

[6] O. Schaff, G. Hess, V. Fernandez, K.-M. Schindler, A. Theobald, Ph. Hofmann, A. M. Bradshaw, V. Fritzsche, R. Davis, and D.P. Woodruff, J. Electron Spectrosc. Relat. Phenom. **75**, 117 (1995).

[7] B.A. Sexton, Surf. Sci. **88**, 299 (1979).

[8] R. Ryberg, Phys. Rev. B **31**, 2545 (1985).

[9] D.A. Outka, R.J. Madix and J. Stöhr, Surf. Sci. **164**, 235 (1985).

[10] T. Lindner, J. Somers, A.M. Bradshaw, A.L.D. Kilcoyne, and D.P. Woodruff, Surf. Sci. **203**, 333 (1988).

[11] J.P. Camplin and E.M. McCash, Surf. Sci. **360**, 229 (1996).

[12] E. Holub-Krappe, K.C. Prince, K. Horn, and D.P. Woodruff, Surf. Sci. **173**, 176 (1986).

[13] F.M. Leibsle, S.M. Francis, R.Davis, N. Xiang, S. Haq, and M. Bowker, Phys. Rev. Lett. **72**, 2569 (1994).

[14] G.W. Rubloff and J.E. Demuth, J. Vac. Sci. Technol. **14**, 419 (1977).

[15] J.E. Demuth and H. Ibach, Chem. Phys. Lett. **60**, 395 (1979).

[16] J.L. Erskine and A. M. Bradshaw, Chem. Phys. Lett. **72**, 260 (1980).

[17] S.M. Gates, J.N. Russel, Jr., and J.T. Yates, Jr., Surf. Sci. **146**, 199 (1984); *ibid.* **159**, 233 (1984).

[18] J.T. Yates, Jr., J.N. Russel, Jr., and S.M. Gates, *Chemistry and Physics of Solid Surfaces VI*, Vol. 5, edited by R. Vanselow and R. Howe (Springer, Berlin, 1986) Chapter 10.

[19] J. N. Russell, Jr., I. Chorkendorff, and J.T. Yates, Jr., Surf. Sci. **183**, 316 (1987).

[20] R. Zenobi, J. Xu, J.T. Yates, Jr., B.N.J. Persson, and A.I. Volokitin, Chem. Phys. Lett. **208**, 414 (1993).

[21] O. Schaff, G. Hess, V. Fritzsche, V. Fernandez, K.-M. Schindler, A. Theobald, Ph. Hofmann, A. M. Bradshaw, R. Davis, and D.P. Woodruff, Surf. Sci. **331-333**, 201 (1995).

[22] F.L. Baudais, A. J. Borschke, J.D. Fedyk, and M.J. Dignam, Surf. Sci. **100**, 210 (1980).

[23] S. Johnson and R.J. Madix, Surf. Sci. **103**, 361 (1981).

[24] H.E. Dastoor, P. Gardner, and D.A. King, Chem. Phys. Lett. **209**, 493 (1993).

[25] B.A. Sexton, Surf. Sci. **102**, 271 (1981).

[26] J. Wang and R.I. Masel, Surf. Sci. **243**, 199 (1991).

[27] J. Wang, M.A. DeAngelis, D. Zaikos, M. Setiadi, and R. I. Masel, Surf. Sci. **318**, 307 (1994).

[28] J.L. Davis and M.A. Barteau, Surf. Sci. **187**, 387 (1987).

[29] J.L. Davis and M.A. Barteau, Surf. Sci. **235**, 235 (1990).

[30] J. Sthör, *NEXAFS Spectroscopy* (Springer, Berlin, 1992).

[31] K Herfmann and C. Meyer, Surf. Sci. **277**, 377 (1992).

[32] J.A. Rodriguez, Surf. Sci. **273**, 385 (1992)

[33] D. Zeroka and R. Hoffmann, Langmuir **2**, 553 (1986).

[34] H. Yang, J.L. Whitten, and C.M. Friend, Surf. Sci. **313**, 295 (1994).

[35] T. Yokoyama, S. Terada, S. Yagi, A. Imanishi, S. Takenaka, Y. Kitajima and T. Ohta, Surf. Sci. **324**, 25 (1995).

[36] N. Pangher, H.M. Köppe, J. Feldhaus and J. Hasse, Phys. Rev. Lett. **71**, 4365 (1993).

[37] J. A. Rodriguez and C. T. Campbell, Surf. Sci. **194**, 475 (1988).

[38] K. Herfmann and C. Meyer, Surf. Sci. **269/270**, 326 (1992).

[39] J. Stöhr, J.L. Gland, W. Eberhardt, D. Outka, R.J. Madix, F. Sette, R.J. Koestner, and U. Doebler, Phys. Rev. Lett. **51**, 2414 (1983).

[40] K.J. Tauer and W.N. Lipscomb, Acta Cryst. **5**, 606 (1952).

[41] *X-ray absorption: Principles, Applications, Techniques of EXAFS, SEXAFS and XANES*, edited by D.C. Koningsberger and R. Prins (Wiley, New York, 1988).

[42] T. Yokoyama, H. Hamamatsu, and T. Ohta, EXAFS Analysis Program EXAFSH Version 2.1 (University of Tokyo, 1994).

[43] J.J. Rehr, R.C. Albers, and S.I. Zabinsky, Phys. Rev. Lett. **69**, 3397 (1992).

[44] P.Uvdal, M.K. Weldon, and C.M. Friend, Phys. Rev. B **50**, 12258 (1994).

Chapter 5

O *K*- and Co *L*-edge x-ray magnetic circular dichroism study of CO- and O-adsorbed ultrathin Co films

The application of XMCD to surface adsorbates is described in this chapter. O *K*-edge x-ray magnetic circular dichroism (XMCD) were observed for molecular CO and atomic O adsorbed on *fcc* Co thin films grown epitaxially on Cu(100). In the case of CO adsorption, the XMCD spectrum suggested an antiparallel alignment of the O orbital moment with Co. On the contrary, a simple c(2×2) adsorption state of atomic O on the Co(100) film was found to be induced a parallel orbital moment. The XMCD intensity is attenuated and diminished as the oxidation proceeds. These observations were compared with a theoretical prediction and a possible interpretation for the experimental findings was proposed. Origins of such a difference between molecular CO and atomic O are discussed.

5-1. Introduction

Surface magnetism has recently attracted great interest in solid state physics as described in §1-1. Magnetic properties of ultrathin metal films have widely been investigated in order to discover and understand significant differences of those magnetism from corresponding bulk ones. Moreover, it has been found that the surface magnetism is significantly affected by the adsorption of atoms and molecules [1–9]. Investigations of the adsorption effects on magnetic films are important to understand the mechanism of magnetic modification in the surfaces of real magnetic materials.

It has been reported that oxygen adsorption on Fe surfaces leads to slight enhancement of the Fe magnetization probably due to an expansion of the Fe-Fe distances upon the O adsorption [1,2]. On the other hand, in the case of thin Ni films grown on Cu(100), significant suppression of Ni magnetization was found even in the physisorbed state of molecular oxygen, and the Ni magnetization is drastically quenched in the atomic O adsorbed state [3]. More drastic changes have been observed in the magnetism of Mn ultrathin films grown on Fe and Co films [4,5]. In the case of 0.5 ML Mn evaporated on a 15 ML Co film grown on a Cu(100) single crystal, the Mn magnetization was found to be reversed by the oxygen exposure, resulting in the antiferromagnetic order between Mn and Co, while the ferromagnetic order is kept in the Mn layer itself [4]. A similar effect was observed for 0.1 ML Mn/Fe/MgO(100) [5]. Another effect of the atomic or molecular adsorption is a rotation of a magnetic easy axis [6,7]. It was revealed that the easy axes of magnetization for Ni/Cu(100) and Co/Cu(110) thin films are rotated by 90° with the adsorption of

H and CO, respectively.

The adsorption of CO on Co films has been studied by spin-polarized photoemission spectroscopy [8]. Although no direct information on the surface magnetization seems to have been obtained, no splitting of the CO 5σ levels indicates substantial quenching of the local magnetic moments at the surface. The atomic O adsorption has also been investigated by means of spin-polarized photoemission and magnetic circular dichroism in the angular distribution [9]. This study showed that the asymmetry of the magnetic dichroism spectra is partly reduced by atomic oxygen. Very recently, semiempirical tight-binding calculations have been performed to understand the chemisorption effects of molecular CO and atomic O on the magnetization of Co [10]. It was concluded that CO is a good magnetization killer in the case of atop adsorption, while atomic oxygen does not essentially affect the Co magnetization. It was also indicated that molecular CO couples antiferromagnetically with Co while the O magnetization is ferromagnetic.

In order to obtain direct information on the magnetization of adsorbates experimentally, the x-ray magnetic circular dichroism (XMCD) technique is one of the most suitable methods since the technique is element specific and the magnetization only from the adsorbates could be extracted. For this reason, artificial bimetal epitaxial layers have widely been investigated to distinguish the magnetization of each metal. It is, however, much more difficult to accumulate reliable XMCD signals from submonolayer adsorbates especially for light elements. This is because the XMCD intensity of *K* edges is essentially weaker than those of other edges like $L_{III,II}$ and $M_{V,IV}$. Although some O *K*-edge XMCD spectra of bulk materials such as CrO_2 [11] and Mn perovskite compounds [12] have been reported, no *K*-edge XMCD data have been published for submonolayer adsorbates of light elements to my knowledge.

In the present study, an attempt was made to measure O *K*-edge surface XMCD for molecular CO and atomic O adsorbed on thin *fcc* Co films grown on Cu(100) by using the newly developed soft x-ray beamline. Adsorption of CO and O, as well as subsequent stepwise oxidation, was investigated to clarify the change of the magnetization of adsorbate and Co films. The obtained XMCD spectra for molecular CO and atomic O are discussed by comparing with the theoretical prediction [10].

This chapter is organized in a following manner. In §5-2, experimental details are given for the XMCD spectroscopic measurements as well as the sample preparation. The process of improvements in the experimental setup is also described to clarify why the present measuring system was adopted. §5-3 describes the experimental results of the O *K*- and Co *L*-edge XMCD and NEXAFS measurements for the molecular CO and atomic O adsorption on the Co ultrathin film. Observed differences between the molecular CO and atomic O adsorption are discussed in §5-4 by referring to the theoretical results [10]. Concluding remarks are briefly given in §5-5.

5-2. Experimental

5-2-1. Utilization of the circularly polarized x rays

O *K*- and Co $L_{III,II}$-edge XMCD and NEXAFS spectra were taken at the new beamline PF-BL-11A. The circularly polarized x-rays can be obtained by taking the upper or lower part of the radiation from the storage ring. It can be attained by simply shifting the vertical aperture S_0 as shown in Fig. 5-1(a). In such a situation, however, around one edge of the grating is illuminated by the x rays, resulting in unstable and weak output intensity [see Fig. 5-2(a)]. Instead, I thought up another method, where the cylindrical mirror M_0' is properly adjusted so that the circularly polarized rays pass the center of the monochromator as illustrated in Fig. 5-1(b). M_0' should be shifted upward by ~3.2 mm, and rotated downward by ~0.007° to accept 0.4 mrad upper part of the radiation. The stability and intensity of the circularly polarized x rays were significantly improved with this adjustment as shown in Fig. 5-2(b). Because of the necessity of the M_0' adjustment, it takes about half an hour to reverse the helicity of the x rays. Therefore it is not practical to obtain the XMCD spectra by reversing the helicity, and another method (reversing the sample magnetization) was adopted.

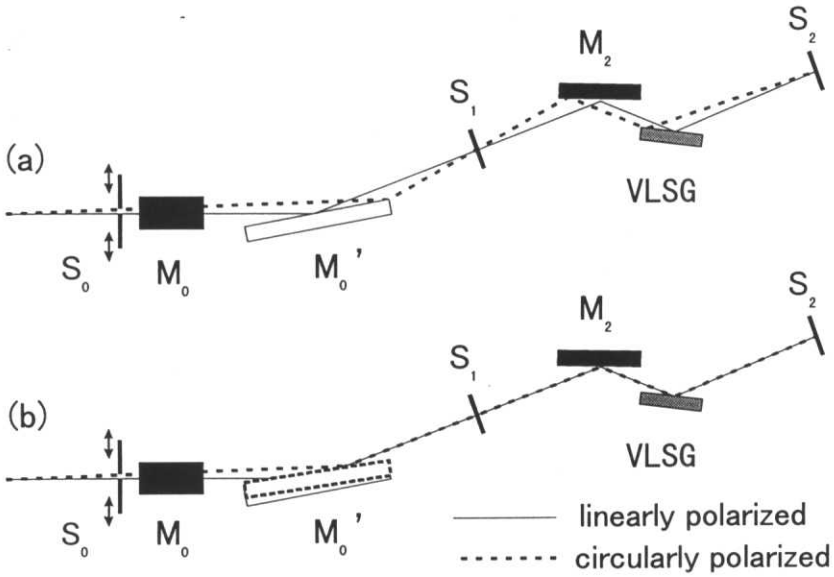

Fig. 5-1. Schematic diagram of the beamline for utilizing the circularly polarized x rays, with (a) fixed and (b) adjusted M_0'. Solid and dashed lines denotes the linearly and circularly polarized x rays, respectively.

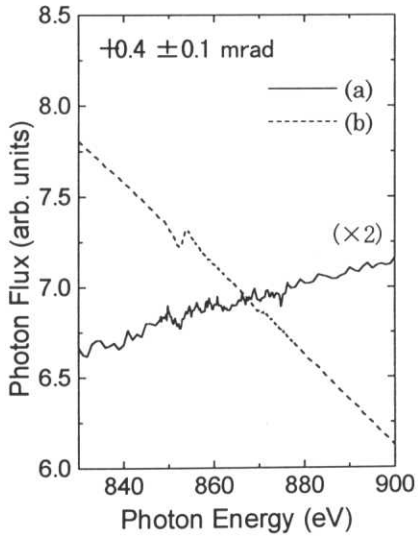

Fig. 5-2. Intensity of the circularly polarized x rays with (a) fixed and (b) adjusted M_0'.

5-2-2. Signal detection and sample magnetization methods

The standard detection method for the XMCD measurements of thin films is sample current (SC) detection, where the sample is electrically isolated and the leak current induced by the electron emission from the sample is measured as illustrated in Fig. 5-3. This is a kind of the total electron yield detection (see §2-1-3). It is, however, almost impossible to obtain the weak signal from surface adsorbates such as molecular CO and atomic O with the SC detection. An alternative detection technique is to utilize a microchannel plate (MCP) detector, which is also adopted for the XAFS measurements as described in §4-2-1. This detection method, however, is seriously affected by the magnetic field because of the restricted acceptance angle of the detector. Moreover, the detector cannot be placed symmetrically with respect to the reversal of the magnetic field, resulting in a significant dependence of the counting rate on the magnetic field direction.

Figure 5-5 shows the detection-method dependence of the Ni *L*-edge XMCD spectra taken by reversing the magnetic field generated by a Permalloy coil depicted in Fig. 5-4. All the spectra were therefore recorded in the magnetic field arising from the residual magnetization of the coil. The Ni thick film (~50 ML) grown on a Cu(100) single crystal was measured in the normal incidence configuration (θ = 90°), where no XMCD signal should be observed [13]. It was found that the absolute signal intensity is significantly affected by the direction of the magnetic field and that the XMCD spectrum (right panel of Fig. 5-5) has some ghost structures if the MCP detector is used with no retarding voltage [designated as (b)]. As the applied retarding voltage increases, the intensity difference between two spectra becomes smaller, resulting in the weaker ghost signals. It suggests that the low energy electrons are more significantly affected by the magnetic field than high energy ones. Almost the same spectra as those for the SC detection can be obtained with the –700 V retarding voltage after the background-subtraction and the normalization, though the absolute intensity still significantly depends on the magnetization direction.

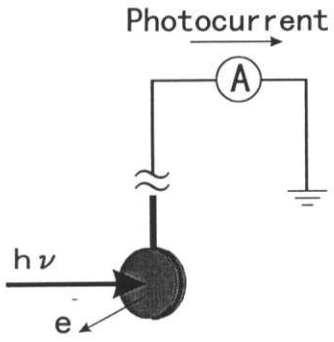

Fig. 5-3. Schematic diagram for the sample current (SC) detection.

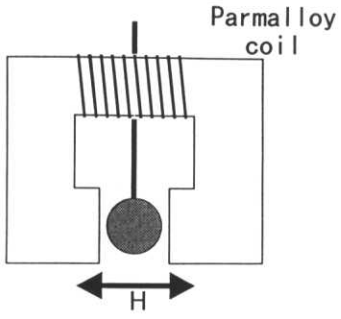

Fig. 5-4. Schematic view of the sample and the Permalloy coil.

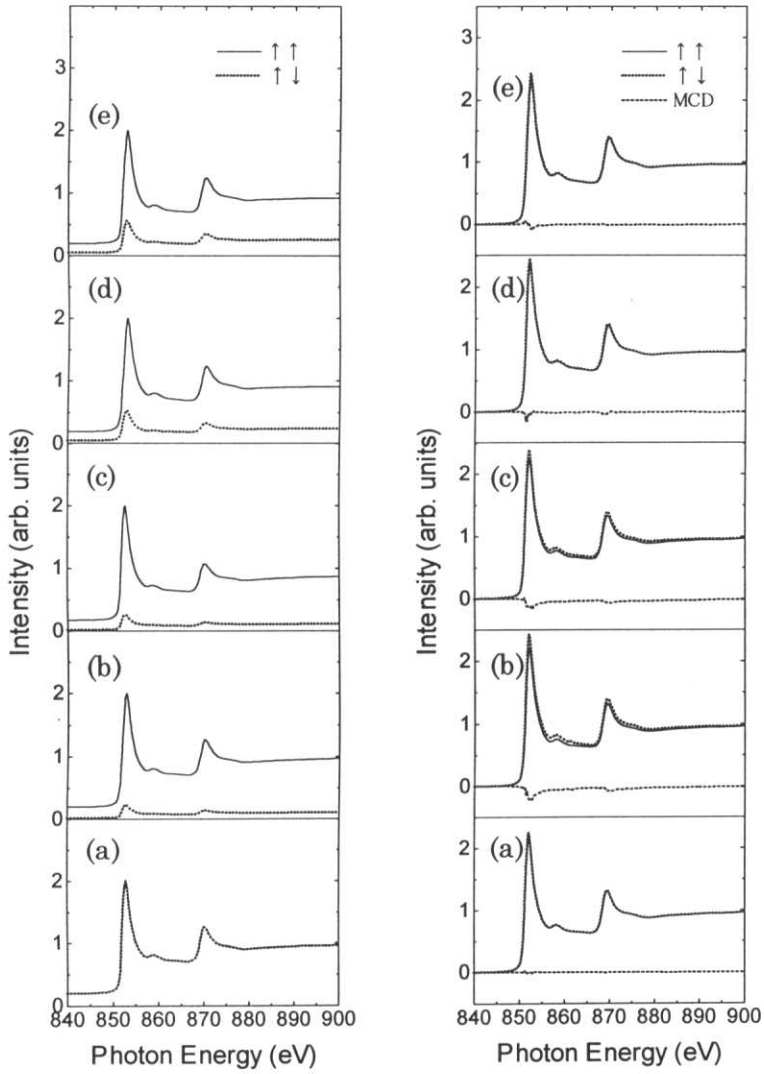

Fig. 5-5. Ni *L*-edge XMCD spectra for the thick Ni film in the normal incidence configuration obtained before (left) and after (right) the background subtraction. The data were taken with (a) sample current (SC) detection and microchannel plate (MCP) detector applying retarding voltages of (b) 0, (c) –100, (d) –500 and (e) –700 V. The sample was magnetized with a Permalloy coil.

Figure 5-7 shows the normal incidence Ni *L*-edge XMCD spectra of a 6 ML Ni film on Cu(100) taken by magnetizing the sample with a current pulse through a Cu coil, as illustrated in Fig. 5-6. No magnetic field remained, in this case, during the measurements except for that arising form the residual magnetization of the sample itself. Both the SC and MCP (with retarding voltage of –600 V) detection methods yield no MCD signals, which is consistent with the previous works [13,14]. Note that the absolute intensities of the spectra are almost the same regardless of the direction of the sample magnetization even with the MCD detection, owing to the weakness of the magnetic field around the detector.

Figure 5-8 shows the Ni *L*-edge XMCD spectra of a 10 ML Ni film on Cu(100) recorded in the normal incidence configuration with the same methods as Fig. 5-7. For this thickness, a clear XMCD signal should be observed [13,14]. It is indicated that the partial electron yield detection with the MCP detector provides the same spectra as those obtained by the SC detection. However, it should be also noted that this magnetization technique is available only for the XMCD measurements of the ferromagnetic sample such as Fe, Co and Ni films.

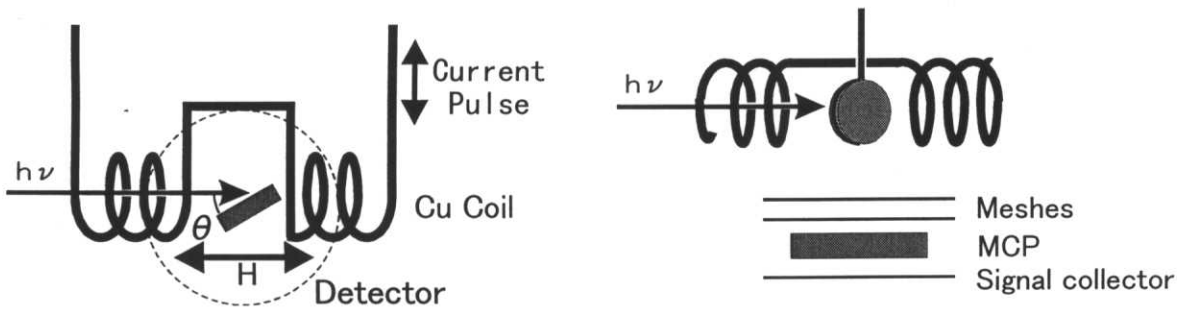

Fig. 5-6. Schematic top (left) and side (right) views for the XMCD measurements with a Cu coil.

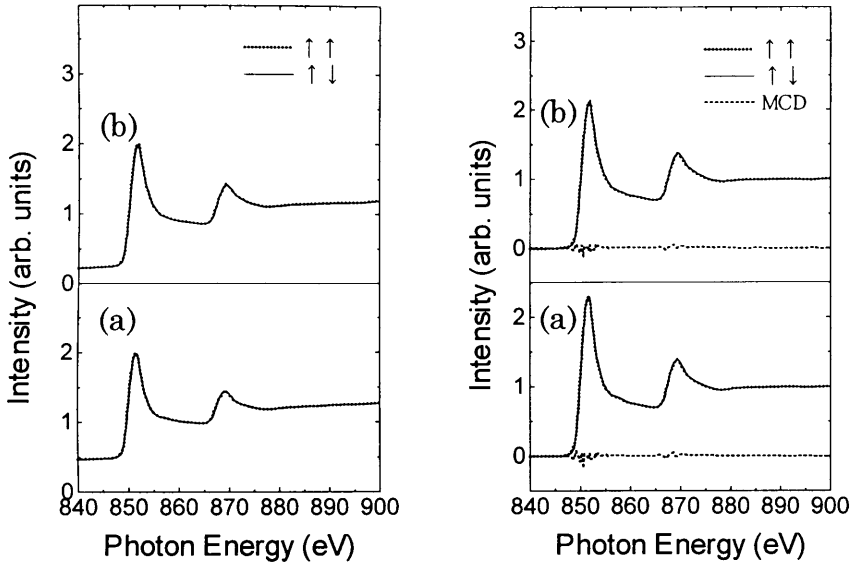

Fig. 5-7. Ni L-edge XMCD spectra for the 6 ML Ni film in the normal incidence configuration obtained before (left) and after (right) the background subtraction. The data were taken with (a) SC and (b) MCP applying a retarding voltage of –600 V.

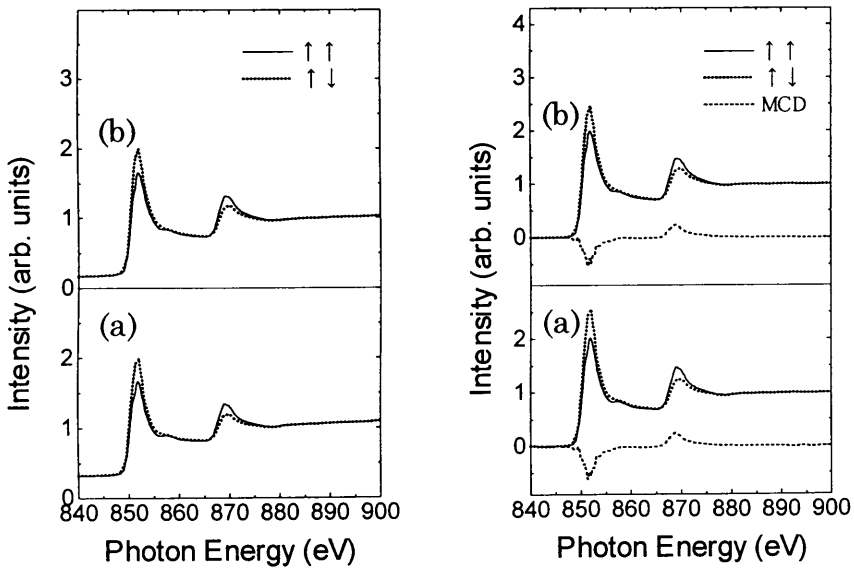

Fig. 5-8. Ni L-edge XMCD spectra for the 10 ML Ni film in the normal incidence configuration obtained before (left) and after (right) the background subtraction. The data were taken with (a) SC detection and (b) MCP applying a retarding voltage of –600 V.

5-2-3. XMCD and NEXAFS measurements

The circularly polarized x rays were obtained by using the upper or lower part of the orbit plane (+0.4 mrad and –0.2 mrad, respectively, and ±0.1 mrad width). The difference between the acceptance angles comes from the mechanical limitation for the movements of S_0, which is not essential. The circular polarization factor was resultantly estimated to be P_c = 0.6 and 0.4, respectively for the upper and lower part, by the method described in §5-3. Both the entrance- and exit-slit widths were 100 μm, providing the x-ray intensities of $1–2\times10^{10}$ photons/s as indicated in Fig. 5-9 for the upper part, and the resolution was 500–800. About two times higher photon flux was obtained for the lower part, while the resolution was, of course, the same as that for the upper part. The experimental setup for the measurements are schematically depicted already in Fig. 5-6. All the spectra were recorded in the partial electron yield mode using a detector consisting of a 25-mm diameter microchannel plate (MCP) and two Au-coated W grids, which was placed just below the sample. Retarding voltages (–400 and –500 V for O *K* and Co *L* edges, respectively) were applied to the second grid (closer to the MCP) while the first one was grounded. For the NEXAFS measurements, incidence angles θ of x rays were 90° (normal incidence), 55° and 30°. The XMCD spectra were obtained by reversing the direction of the sample magnetization, leaving the helicity of the incident x rays unchanged. The samples were mounted in a Cu coil and were magnetized along the incident x rays by a current pulse. The pulse currents were large enough to reach the saturation of magnetization of the Co films, and the remanent magnetization was examined. Since *fcc* Co films investigated here are known to be magnetized along the surface plane [14–16], only the grazing-incidence (θ = 30°) XMCD spectra were recorded. Although angular dependence of the XMCD spectra might be important to discuss the magnetic moments quantitatively [17,18], the main issue in the present investigation is to observe O *K*-edge XMCD spectra of submonolayer adsorbates which required a long accumulation period, and no angular dependence was examined. Typical accumulation time for each data point was 10 s for Co $L_{III,II}$-edge XMCD and O *K*-edge NEXAFS, and 200 s for O *K*-edge XMCD.

In order to obtain reliable XMCD data, it is essential to avoid the effects of the energy shift between two spectra, $\mu_{\uparrow\uparrow}$ and $\mu_{\uparrow\downarrow}$. Therefore the relative photon energy of each spectrum was carefully calibrated with the precision of <0.01 eV using absorption structures of oxygen contamination on mirrors, appearing in the transmission function measured by a Au-coated W mesh placed at the upstream of the sample.

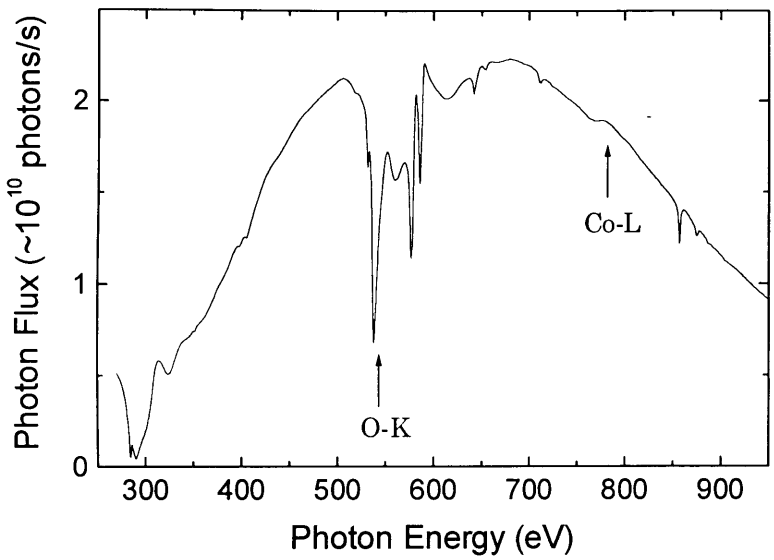

Fig. 5-9. Photon flux distribution of the circularly polarized x-rays obtained from the upper part of the orbit plane (+0.4 mrad, ±0.1 mrad width). Both the entrance- and exit-slit widths were 100 μm.

5-2-4. Sample preparation

The *fcc* Co films were prepared on a Cu(100) single crystal according to the following procedure. The Cu substrate was cleaned in an ultrahigh vacuum (UHV) chamber by successive cycles of Ar^+ bombardment and annealing at 900 K. Sample annealing was performed by electron bombardment from the rear side of the crystal and the temperature was monitored with a chromel-alumel thermocouple. The cleanliness and order of the surface were confirmed by NEXAFS and RHEED (reflection high-energy electron diffraction). The *fcc* Co film was grown at room temperature by evaporation from a resistively heated Co wire. Thickness of the film was monitored by the *in situ* observation of the RHEED oscillations and confirmed also by the Co $L_{III,II}$-edge jumps after the preparation. The typical deposition rate was 0.1–0.2 ML/min [ML (monolayer) is defined as the number of Co atoms with respect to the surface Cu atoms]. In these conditions, the Co film is known to grow epitaxially in the thickness region of from, at least, 2 ML to >10 ML [19–22]. The Co thickness was 4 and 2.4 ML for the CO and O adsorption experiments, respectively.

For the CO adsorption experiments, the 4 ML *fcc* Co film grown on Cu(100) was exposed to 1 L CO (2×10^{-8} Torr for 50 s) and then cooled to 200 K. During the following XMCD and NEXAFS measurements, the sample temperature was kept constant at 200 K. The temperature of 200 K

was chosen to exclude the possibilities of gradual water adsorption at lower temperatures and of decomposition and desorption of CO at higher temperatures.

As regards the O adsorption experiments, a c(2×2)O/Co/Cu(100) overlayer (stage I) was at first prepared according to the literature [23]. The 2.4 ML Co film was dosed with 0.2 L (5×10^{-9} Torr for 40 s) oxygen at room temperature and heated to 410 K. Unfortunately, no LEED optics were installed at the present chamber to detect the c(2×2) superstructure. Additional dosage with 0.2 L oxygen, however, did not increase the O coverage verified by O *K*-edge jumps. The previous study [23] found a plateau of the O coverage as a function of dosage around the c(2×2)O region, indicating that the present surface prepared by the 0.2 L oxygen exposure may correspond to the c(2×2)O/Co overlayer. The c(2×2)O/Co overlayer was subsequently dosed with a much greater amount of oxygen [further 10 L (2×10^{-7} Torr for 50 s)] at room temperature (stage II). The sample was consequently dosed with 120 L oxygen at 423 K (stage III) to yield a complete Co oxide film. These three oxidation stages I, II, and III were investigated by measuring O *K*- and Co $L_{III,II}$-edge XMCD and NEXAFS at room temperature.

5-3. Results

5-3-1. Molecular CO adsorption

The incidence-angle dependence of the O *K*-edge NEXAFS spectra for adsorbed CO is given in Fig. 5-10. These spectra were obtained by the following procedures: division of the oxygen-adsorbed spectra with the clean ones, subsequent subtraction of the pre-edge linear baseline, and final normalization with the edge jump at 570 eV. Since no reference spectra are available, the coverage of CO could not be estimated. Angle dependence of the NEXAFS spectra clearly exemplifies that the CO molecule is at least qualitatively standing up on the Co surface. The π^* resonance at ~533 eV is enhanced at normal x-ray incidence, while the σ^* resonance is enhanced at grazing incidence.

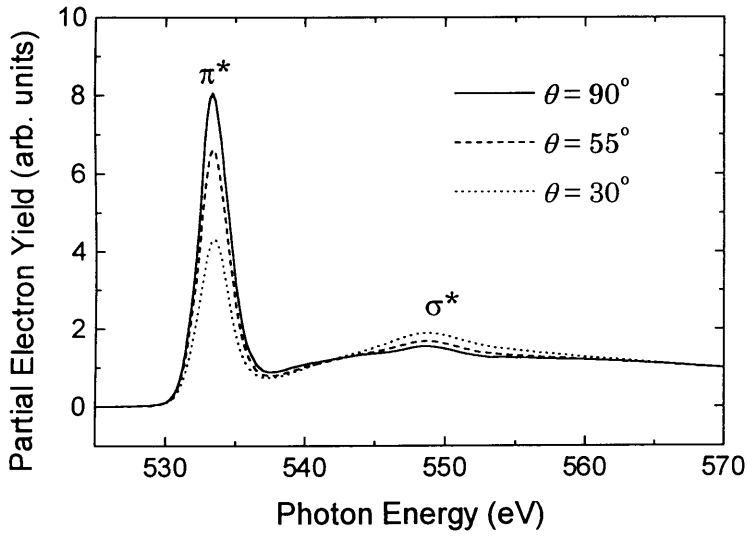

Fig. 5-10. Incidence-angle dependence of the O *K*-edge NEXAFS spectra of CO adsorbed on the 4 ML *fcc*-Co film grown on Cu(100).

Figure 5-11 shows the Co $L_{III,II}$-edge circularly polarized spectra of clean and CO-adsorbed 4 ML *fcc*-Co film, together with those of bulk *hcp* Co. The spectra were obtained from the raw data by the linear pre-edge subtraction and subsequent normalization with the $L_{III,II}$-edge jumps. For the quantitative evaluation of the Co spin and orbital moments described below, information on the number of *d* holes, n_h, is necessary. The white-line intensities, which are proportional to n_h, were estimated by subtracting the step functions for the $L_{III,II}$ edges from the polarization-averaged spectra [17]. The *d*-hole number of reference bulk *hcp* Co was assumed to be 2.50 [24,25]. For the saturation (self-absorption) effect of the electron yield measurements [18], the spectra of bulk Co

was rescaled assuming the electron escape depth of 25 Å and the infinite thickness of bulk Co. On the other hand, no saturation effect was taken into account for the present ultrathin Co films on Cu(100). Resultantly obtained n_h for each sample is inserted in Fig.5-11. The uncertainty for the estimated hole number, n_h, mainly come from the ambiguity of the background and step functions, sometimes resulting in the errors of more than 10 % for absolute n_h values.

Figure5-12 shows the Co $L_{III,II}$-edge XMCD spectra. These spectra were obtained by the subtraction between the two spectra given in Fig. 5-11 and the subsequent rescaling with the factor of $P_c \cos\theta$. The rescaling was performed in order to compensate the reduction of the XMCD signal due to the imperfect polarization and the angle between the direction of the magnetization and incident x rays. The value of P_c was determined so that the spin moment of bulk *hcp* Co may match the value of m_s = 1.62 (the unit of Bohr magneton) reported by the transmission XMCD

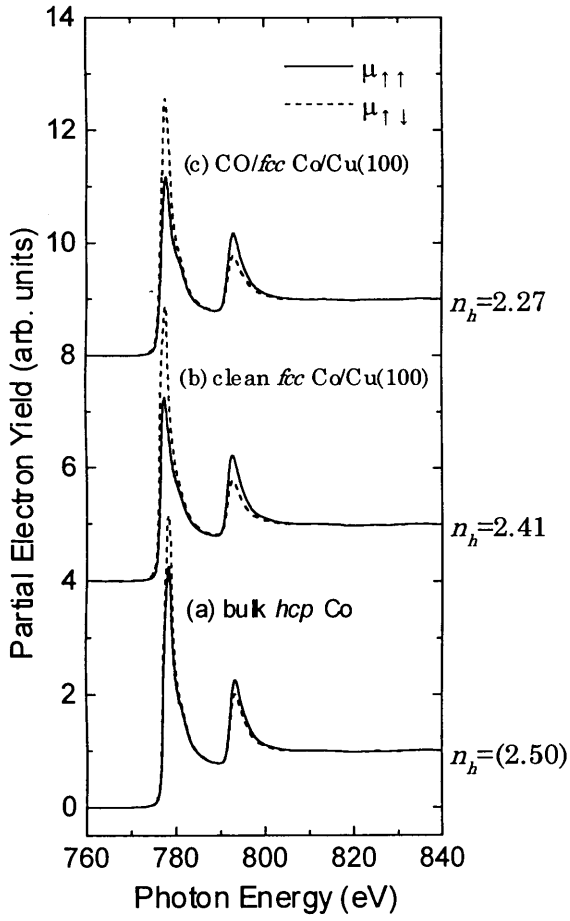

Fig. 5-11. Co *L*-edge circularly polarized x-ray absorption spectra for (a) bulk *hcp* Co, (b) clean 4 ML *fcc*-Co film and (c) CO-adsorbed film. The estimated values of n_h are also inserted.

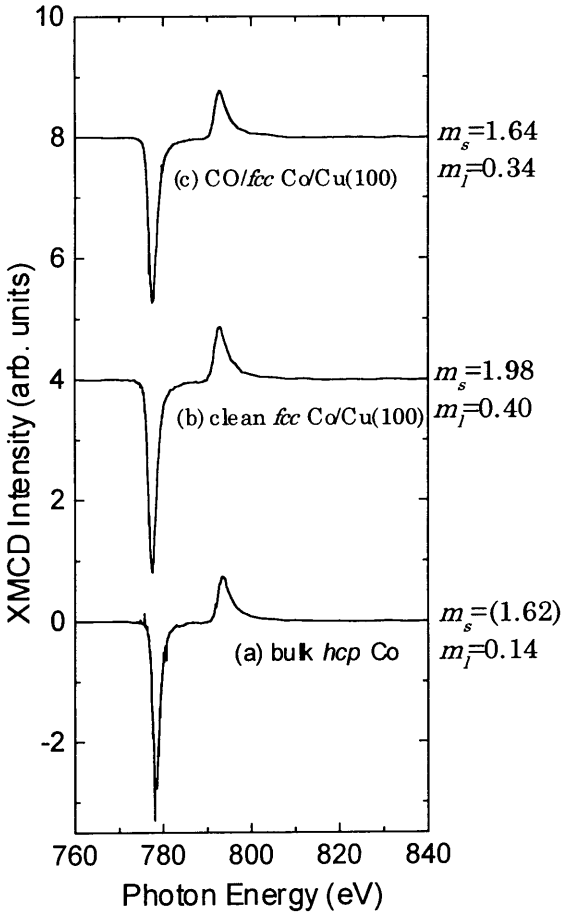

Fig. 5-12. Co *L*-edge XMCD spectra for (a) bulk *hcp* Co, (b) clean 4 ML *fcc*-Co film and (c) CO-adsorbed film. The obtained m_s and m_l are also given.

measurements [26]. By employing the well-established sum rules [27,28] with the assumption of n_h = 2.50 for bulk *hcp* Co (the magnetic dipole contribution, m_T, was neglected), the circular polarization factor was consequently estimated. Thus there are some uncertain parameters such as n_h, m_T, and the electron escape depth, which make the estimation of P_c unreliable. The present uncertainty of P_c, however, provides no serious problem since the relative XMCD changes are the main focus of the present study.

It can be recognized from Fig. 5-12 that the magnetization of Co is apparently suppressed with the CO adsorption. The spin and orbital moments of Co at each stage were evaluated by using the data of bulk *hcp* Co as a standard and neglecting again the magnetic dipole terms. The obtained values for the spin and magnetic moments, m_s and m_l respectively, are indicated in Fig. 5-12. The obtained magnetic moments may have large (>10 %) errors due mainly to the uncertainty in the n_h values. The relative difference between the clean and CO-adsorbed films, however, seems to be rather reliable because the same background and step functions can be used since the film thickness was not changed. The spin moment is reduced to m_s = 1.64 (17% reduction relative to that of the clean 4 ML Co film), with the adsorption of molecular CO. This indicates that CO is a good magnetization killer as predicted in the previous theoretical study [10], considering that the obtained moment is an average over the whole Co film not only for the topmost layer.

Figure 5-13 gives the O *K*-edge XMCD spectra of CO adsorbed on the 4 ML Co film, together with the circularly polarized absorption spectrum. Since the difference between the two spectra, $\mu_{\uparrow\uparrow}$ and $\mu_{\uparrow\downarrow}$, is quite small, only one of them is shown. In order to confirm the reliability of the XMCD data, the spectra taken with different helicity of the rays were also shown. Here, the XMCD spectra are similarly normalized with the factor of $P_c \cos\theta$ as well as the O *K*-edge jumps. A positive peak is apparently observed in both spectra and the normalized XMCD signal for +0.4 mrad x rays is almost identical to that for –0.2 mrad. This indicates that the obtained XMCD signals are not artifacts, which may originate from some possible slight changes of the electron yield upon flapping of the magnetization direction. Moreover, the XMCD spectra did not change regardless of which direction of the magnetic field was formerly applied (not shown), which excludes the possibility of some time-dependent artifacts. Thus it can be concluded that the present observation of the O *K*-edge XMCD signals are reliable without any doubt.

According to the orbital sum rule described in §2-2-3 [27–29], the positive XMCD signal indicate the opposite orbital magnetic moment of oxygen with the Co film. Moreover, the positive peak in XMCD coincides with the π^* resonance, indicating the presence of a negative orbital magnetic moment in the 2 π^* level which interacts strongly with the Co 3*d* bands. It should be also noted that no XMCD signals were observed for the intense σ^* resonance. This should be because of the localization of the $6\sigma^*$ level within the molecule.

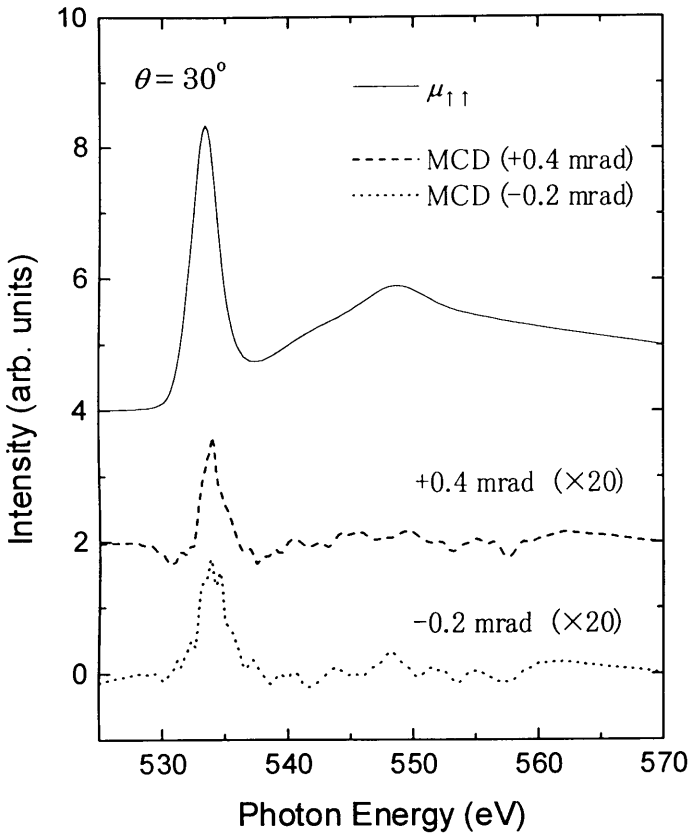

Fig. 5-13. O *K*-edge circularly polarized x-ray absorption spectrum (solid line) and XMCD spectra taken with the +0.4 mrad (dashed line) and –0.2 mrad (dotted line) x rays. Only one spectrum is depicted for the circularly polarized data because of too small differences.

5-3-2. Atomic oxygen adsorption

Figure5-14 gives the incidence-angle dependent O *K*-edge NEXAFS spectra for the c(2×2) oxygen adsorption on 2.4 ML *fcc* Co/Cu(100) and successive oxidation procedures. From the O *K*-edge jumps, relative amounts of deposited O can be estimated. Although no reference spectra are available, O coverage at stage I was assumed to be 0.5 ML because the stage should provide the c(2×2)O overlayer [23] as described in §5-2-4. At stage I, distinct polarization dependence was observed. The first resonance at ~532 eV is enhanced at grazing x-ray incidence, while the second one is pronounced at normal x-ray incidence. The first peak can be ascribed to the transition to the O $2p_z$ level interacting with the Co $3d$ bands [3]. Polarization dependence of the spectra becomes less prominent as Co oxidation proceeds. The spectra of stage III closely resemble the O *K*-edge NEXAFS of NiO [3]. This indicates that the chemical species at stage III should be CoO because of equivalent structures of CoO and NiO (NaCl type). The O coverage for stage III (2.6 ML) is consistent with the value estimated from the initially deposited Co amount of 2.4 ML assuming the

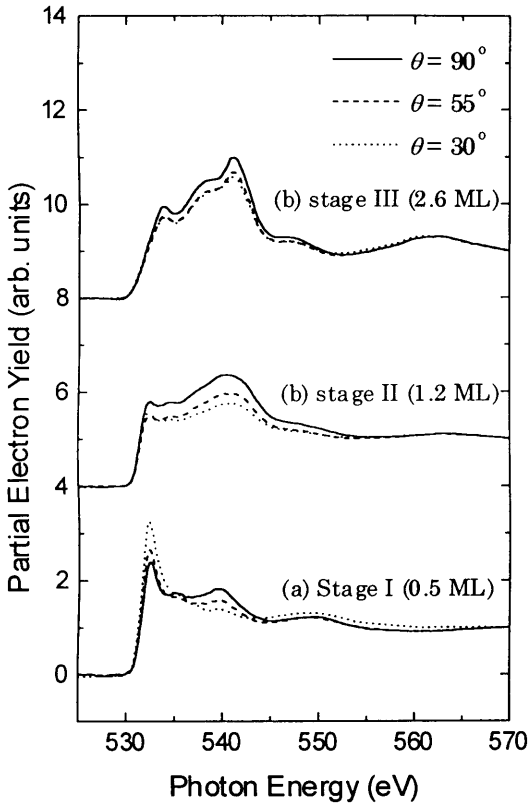

Fig. 5-14. Incidence-angle dependence of the O *K*-edge NEXAFS spectra for the oxidation process (a) stage I, (b) stage II and (c) stage III of the 2.4 ML *fcc*-Co film on Cu(100).

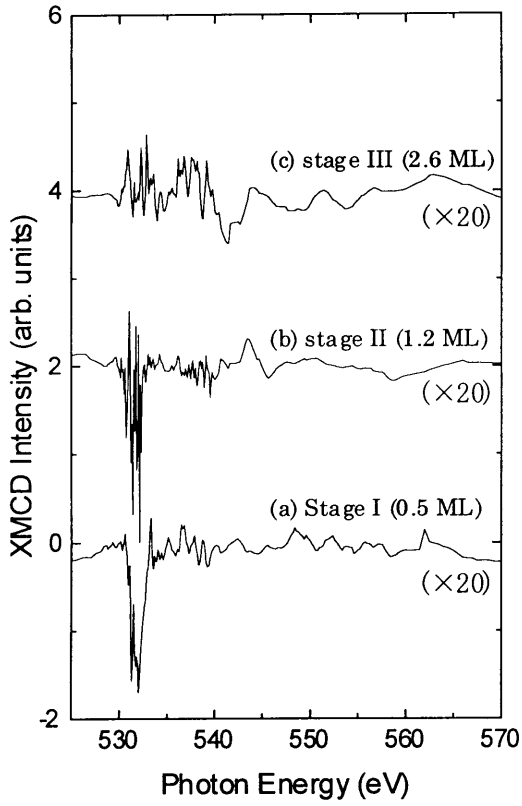

Fig. 5-15. O *K*-edge XMCD spectra for the oxidation process (a) stage I, (b) stage II and (c) stage III of the 2.4 ML *fcc*-Co film on Cu(100).

CoO stoichiometry of 1:1. Stage II is regarded as an intermediate stage of oxidation.

Figure 5-15 shows the O *K*-edge XMCD spectra of the three oxidation stages. Again the spectra are normalized with the factor of $P_c \cos\theta$ as well as the O *K*-edge jumps. Since the reliability of the XMCD observation is confirmed for the CO adsorption, the spectra were taken with only one helicity (+0.4 mrad). Negative peaks are clearly found at both the first and second stages. This indicates that the induced orbital magnetic moment on O is parallel to the Co magnetic moment, in contrast to the CO adsorption. The peak at ~532 eV coincides with the hybridized levels of the O $2p_z$ and Co $3d$ orbitals. As oxidation proceeds, the XMCD signals are attenuated and completely diminished at stage III, which is quite reasonable since bulk CoO is antiferromagnetic.

Let me now turn to the Co $L_{III,II}$-edge XMCD spectra of 2.4 ML *fcc* Co on Cu(100) through the oxidation process. Figure 5-16 shows circularly polarized spectra, together with the estimated n_h values. Although the errors in n_h values are rather large as described above, a significant increase in n_h can be observed for stage III, which consists with the deep oxidation of the Co film. The Co

$L_{III,II}$-edge XMCD spectra and obtained magnetic moments, m_s and m_l, are given in Fig. 5-17. It can be apparently seen that the magnetization of Co is suppressed with the oxidation and is almost diminished at stage III, which is consistent with the O *K*-edge results. In the c(2×2)O/Co state (stage I), the spin moment is reduced to m_s = 1.58 (18% reduction relative to that of the clean 2.4 ML Co film, m_s = 1.93). Much more drastic suppression of the magnetization is found at stage II (66 % reduction) and the magnetization is almost completely diminished at stage III, which consists of CoO.

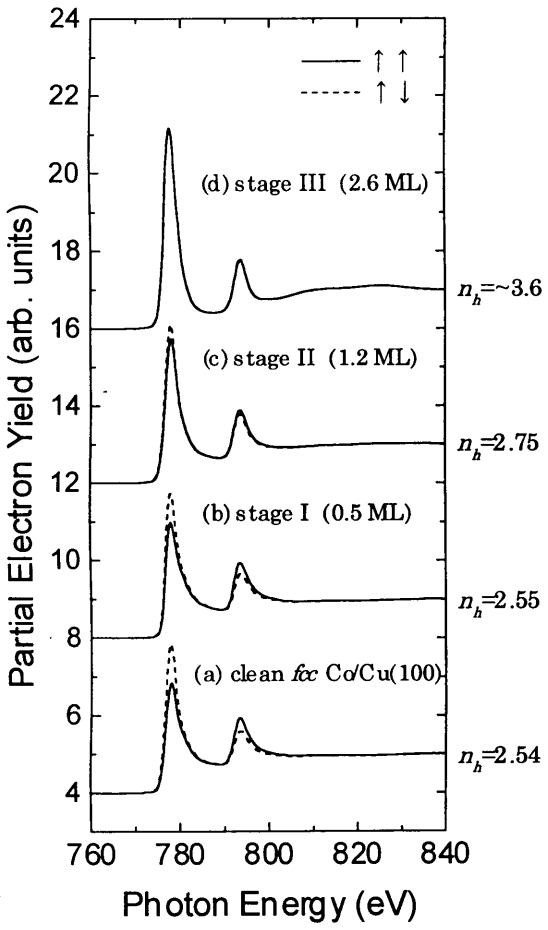

Fig. 5-16. Co *L*-edge circularly polarized x-ray absorption spectra for (a) clean 2.4 ML *fcc*-Co film onCu(100) and (b)–(d) O-adsorbed film (stage I, II and III). The estimated values of n_h are also inserted.

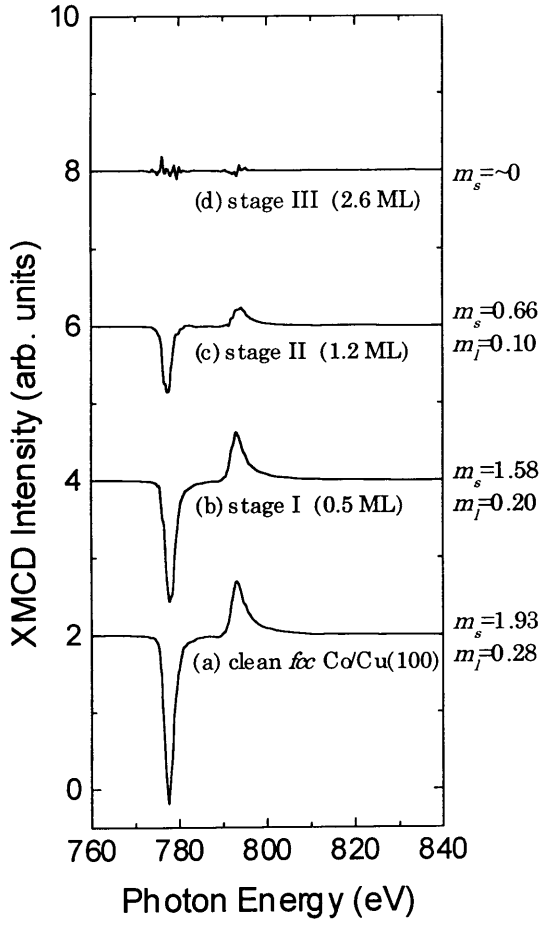

Fig. 5-17. Co *L*-edge XMCD spectra for (a) clean 2.4 ML *fcc*-Co film onCu(100) and (b)–(d) O-adsorbed film (stage I, II and III). The obtained m_s and m_l are also given.

5-4. Discussion

Before discussing the experimental observations, let me here recall the theoretical study reported very recently by Pick *et al* [10]. They have performed semiempirical tight-binding calculations of the spin magnetic moments for the atomic O and molecular CO adsorption on the *hcp* Co(0001) surface and the Co_{13} and Co_{55} clusters. As for the (1×1)-O adsorption on Co(0001), they found a ferromagnetic coupling of the O spin magnetic moment (m_s = 0.08) and some suppression of the surface Co magnetization (m_s = 1.43 compared to that on the clean surface of m_s = 1.70). On the other hand, in the case of atop-CO adsorption, the spin magnetic moments of CO and surface Co were estimated to be –0.03 and 0.48, respectively. This implies that CO is antiferromagnetically coupled with the total Co magnetization and the spin magnetic moment of the surface Co atom is drastically reduced. In the case of bridge-site adsorption of CO, on the other hand, the magnetization quenching is much less prominent (0.10 and 1.61 for CO and Co, respectively). For the CO adsorption on the Co_{13} and Co_{55} clusters, they found that the total magnetization in one Co atom directly interacting with CO is antiferromagnetic (–0.11 for the icosahedral Co_{13} cluster and –0.05 for Co_{55}).

These results can be interpreted as follows. In general, the interaction between CO and transition metal atoms is understood in terms of a cooperation of donation and back donation from CO to metal atoms. In this case, the CO $2\pi^*$ orbitals should be considered, which play a role for the back-donating interaction. In the case of the atop-site adsorption, the Co $3d$ orbitals interacting with CO $2\pi^*$ are purely of π symmetry, as illustrated in Fig. 5-18. Due to pure and hence strong interaction between the CO $2\pi^*$ and Co $3d\pi$ orbitals, the hybridized occupied levels resultantly become more stable and more delocalized, accompanied by a suppression of the exchange splitting. These effects should result in a significant modification for the exchange splitting between the hybridized orbitals and other $3d$ levels at the nearest-neighbor Co atoms. In the case of small modification, the exchange splitting is reduced to yield weaker ferromagnetic interaction. In the case of significant modification, a delocalized scheme becomes probable, which consequently overcome the ferromagnetic exchange and turns to antiferromagnetic interaction. On the contrary, the bridge-site adsorption of CO leads to mixing between the σ and π orbitals due to a symmetry lowering. The CO $2\pi^*$ levels interact less significantly with each Co $3d$ level, resultantly preserving the ferromagnetic coupling between Co–CO and the rest Co atoms.

In the case of atomic O adsorption at the hollow site, strong antiferromagnetic coupling should be still less probable than the bridge-site adsorption of CO. All the Co $3d$ orbitals participate in the chemical bonds with oxygen (O $2p_z$), yielding weaker contribution of each Co $3d$ orbital to the Co–O bonding. Due to this compensation, the magnetizations of the surface Co atoms and hence of the O atoms remain ferromagnetic. Atomic O adsorption shows a less prominent effect for the

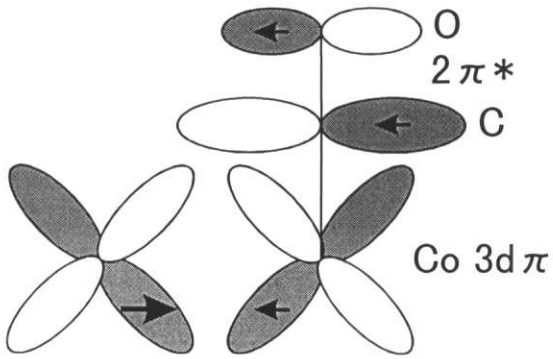

Fig. 5-18. Schematic view of the π-type interaction between the CO $2\pi^*$ and Co $3d\pi$ orbitals in the case of atop adsorption of molecular CO.

strong ferromagnet of the Co thin films. This is interesting when one recalls that the total chemical binding energy for the atomic O adsorption should be greater than that for atop CO.

The most important experimental results in the present work are that molecular CO adsorbed on the 4 ML *fcc* Co film on Cu(100) has the positive O *K*-edge XMCD signal, while the negative peak is observed for the O adsorption. The present results imply that the $2p$ orbital moments of molecular CO and atomic O on Co films are antiparallel and parallel to the Co magnetization, respectively, according to the sum rule [27–29]. In the case of *K*-edge XMCD of Ni, the relation between the orbital moments and the XMCD signal does not still seem to be straightforward possibly because of complicated compensation due to huge contribution of Ni $3d$ levels [29]. The present results might be, however, easier to understand since the magnetic moment of oxygen, though small, mostly originates from the O $2p$ levels, which directly contribute to the *K*-edge XMCD spectra.

In order to compare the present results with the previous theoretical predictions [10], the information about the adsorption site of CO is necessary. Unfortunately, no structural studies have been performed for the CO adsorption on *fcc* Co(100) because bulk *fcc* Co cannot be obtained under usual conditions. However, an atop site adsorption is most probable but a bridge one may coexist, from an analogy with CO/Ni(100) and CO/Co(0001) [30–34]. Therefore, above discussion about the purity of the *p*-type interaction seems to be valid also for the present system, at least qualitatively. Although the spin moments were calculated in the previous study while the present work observed orbital moments, both studies suggested the antiparallel and parallel alignments of the CO and O moments with the total Co ones, respectively.

The direction of the spin moment of oxygen may be determined with a following hypothesis. It

is well known that for the Co $3d$ magnetization the orbital moment is aligned along the parallel direction with the spin moment. This is simply explained using the Hund's rule; a parallel orientation of the $3d$ orbital and spin moments is predicted when more than half of the $3d$ levels are occupied as in Co. If the Hund's rule can be applied to the oxygen $2p$ shell, it may be similarly predicted that the spin and orbital moments of oxygen are aligned parallel to each other, since the O $2p$ subshells are filled by more than half electrons both in the molecular CO and atomic O adsorbate systems. In such a situation, the spin magnetic moments of CO and O on Co should be, respectively, antiparallel and parallel to that of the Co thin films, this being essentially consistent with the theoretical predictions [10]. Figure 5-19 shows magnetic structure models for CO/Co and O/Co derived from the present observations and previous theoretical study [10]. For the verification of the present hypothesis, some sophisticated theoretical studies which directly treat the O K-edge XMCD are indispensable.

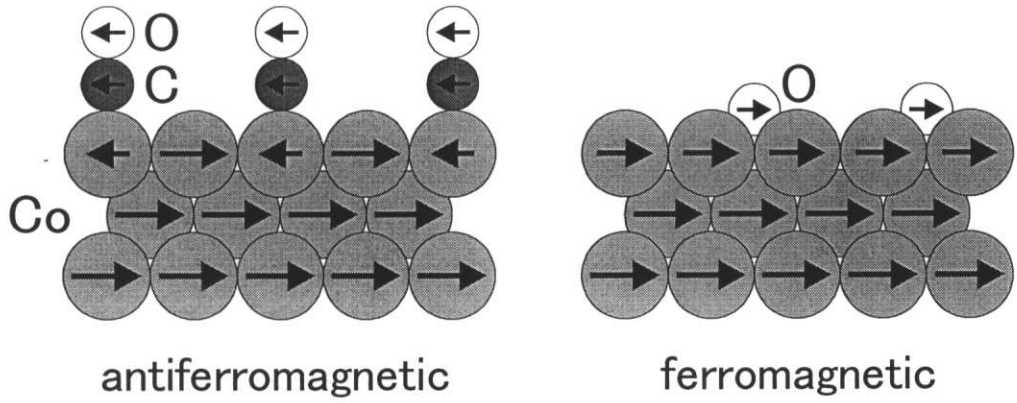

Fig. 5-19. Magnetic structure models for the CO- and O-adsorbed Co thin films derived from the present experimental results and the previous theoretical study [10].

5-5. Summary

O *K*-edge XMCD spectra of molecular CO and atomic O adsorbed on *fcc* Co ultrathin films grown epitaxially on Cu(100) were successfully recorded to investigate induced magnetization on the adsorbates. The saturated CO adsorption phase exhibited a positive XMCD sign for the CO π^* level, while the c(2×2)O overlayer gave a negative sign concerning the O $2p_z$ level. Further note that in the CO adsorption case no XMCD signal was observed for the σ^* resonance. According to the sum rule [27–29] for *K*-edge XMCD, these findings suggested, respectively, the antiparallel and parallel alignments of the orbital magnetic moments of molecular CO and atomic O with the Co magnetic moments. For the O deposited surface, the XMCD intensity was found to be attenuated and diminished as oxidation proceeds.

These observations were comparatively discussed with the theoretical studies [10], which predicted antiferromagnetic and ferromagnetic interactions for the molecular CO and atomic O adsorption on the Co films, respectively. A possible explanation was presented to relate the present results to the previous work [10] using the Hund's rule. If the Hund's rule can be applied to oxygen, the orbital and spin moments should be parallel to each other, since the O $2p$ subshells are filled by more than half electrons in both the molecular CO and atomic O cases. Accordingly, the antiferromagnetic and ferromagnetic couplings of CO and O with Co films were suggested.

The present work has demonstrated the possibility of the XMCD technique for studying the magnetization of adsorbates as well as substrates. Further theoretical works are desired to obtain deeper insight on the XMCD spectra.

References

[1] S.R. Chubb and W. E. Pickett, Phys. Rev. Lett. **58**, 1248 (1987).

[2] R. Wu and A.J. Freeman, Phys. Rev. B **45**, 7532 (1992).

[3] F. May, M. Tischer, D. Arvanitis, M. Russo, J. Hunter Dunn, H. Henneken, H. Wende, R. Chauvistré, N. Mårtensson and K. Baberschke, Phys. Rev. B **53**, 1076 (1996).

[4] W.L. O'Brien and B.P. Tonner, Phys. Rev. B **58**, 3191 (1998).

[5] S. Andrieu, E. Foy, H. Fischer, M. Alnot, F. Chevrier, G. Krill and M. Piecuch, Phys. Rev. B **58**, 8210 (1998).

[6] R. Vollmer, Th. Gutjahr-Loser, J. Kirschner, S. van Dijken and B. Poelsema, Phys. Rev. B **60**, 6277 (1999).

[7] S. Hope, E. Gu, B. Choi and J.A.C. Bland, Phys. Rev. Lett. **80**, 1750 (1998).

[8] M. Getzlaff, J. Bansmann, and G. Schönhense, J. Chem. Phys. **103**, 6691 (1995).

[9] J. Bansmann, L. Lu, and M. Getzlaff, Surf. Sci. **402–404**, 371 (1998).

[10] Š. Pick and H. Dreyssé, Phys. Rev. B **59**, 4195 (1999).

[11] K. Attenkofer and G. Schütz, J. Phys. IV France, **7**, C2-459 (1997).

[12] E. Pellegrin, L.H. Tjeng, F.M.F. de Groot, R. Hesper, G.A. Sawatzky, Y. Moritomo, and Y. Tokura, J. Phys. IV France, **7**, C2-405 (1997).

[13] W. L. O'Brien, T. Droubay and B.P. Tonner, Phys. Rev. B **54**, 9297 (1996).

[14] F. Huang, M.T. Kief, G.J. Mankey and R.F. Willis, Phys. Rev. B **49**, 3962 (1994)

[15] M. Tischer, O. Hjortstam, D. Arvanitis, J. Hunter Dunn, F. May, K. Baberschke, J. Trygg, J.M. Wills, B. Johansson, and O. Eriksson, Phys. Rev. Lett. **75**, 1602 (1995).

[16] J. Hunter Dunn, D. Arvanitis, N. Mårtensson, M. Tischer, F. May, M. Russo, and K. Baberschke, J. Phys. Condens. Matter **7**, 1111 (1995).

[17] J. Stöhr and R. Nakajima, J. Phys. IV France, **7**,C2-47 (1997).

[18] R. Nakajima, J. Stöhr, and Y.U. Idzerda, Phys. Rev. B **59**, 6421 (1999).

[19] J. Fassbender, R. Allenspach and U. Dürig, Surf. Sci. **383**, L742 (1997).

[20] U. May, J. Fassbender and G. Güntherodt, Surf. Sci. **377–379**, 992 (1997).

[21] O. Heckmann, H. Magnan, P. le Fever, D. Chandesris and J.J. Rehr, Surf. Sci. **312**, 62 (1994).

[22] H. Li and B.P. Tonner, Surf. Sci. 237, **141** (1990).

[23] W. Clemens, E. Vescovo, T. Kachel, C. Carbone, and W. Eberhardt, Phys. Rev. B **46**, 4198 (1992).

[24] O. Eriksson, B. Johansson, R.C. Albers, A.M. Boring, and M.S.S. Brooks, Phys. Rev. B **42**, 2707 (1990).

[25] P. Söderlind, O. Eriksson, B. Johansson, R.C. Albers, and A.M. Boring, Phys. Rev. B **45**, 12911 (1992).

[26] C. T. Chen, Y.U. Idzerda, H.J. Lin, N.V. Smith, G. Meigs, E. Chaban, G.H. Ho, E. Pellegrin, and F. Sette, Phys. Rev. Lett. **75**, 152 (1995).

[27] B.T. Thole, P. Carra, F. Sette, and G. van der Laan, Phys. Rev. Lett. **68**, 1943 (1992).

[28] P. Carra, B.T. Thole, M. Altarelli, and X. Wang, Phys. Rev. Lett. **70**, 694 (1993).

[29] J. Igarashi and K. Hirai, Phys. Rev. B **50**, 17820 (1994).

[30] H. Papp, Surf. Sci. **129**, 205 (1983).

[31] F. Greuter, D. Heskett, E.W. Plummer and H.-J. Freund, Phys. Rev. B **27**, 7117 (1985).

[32] J. Lahtinen, J. Vaari and K. Kauraala, Surf. Sci. **418**, 502 (1998).

[33] A. R. Kortan and R.L. Park, Phys. Rev. B **23**, 6340 (1981).

[34] J. Lauterbach, M. Wittmann and J. Küppers, Surf. Sci. **279**, 287 (1992).

Concluding remarks

In the present study, a high-resolution soft x-ray monochromator was developed and successfully applied to the investigations on the surface geometrical and electronic structures and surface magnetism, by use of the x-ray absorption spectroscopies.

I at first constructed a soft x-ray monochromator equipped with a VLS plane grating. Owing to a new design concept and proper alignments of the beamline optics, a reasonable resolving power as well as high photon flux was obtained. Thanks to the new beamline, the submonolayer amounts of specimen can be investigated with the x-ray absorption spectroscopies. Moreover, the purity of the light was significantly improved in order to obtain the absorption spectra with high quality for the surface systems. The scattered light levels were drastically lowered by using a VLS grating fabricated with aspheric wavefront holographic recording. The higher spectral orders were efficiently removed with a harmonic-rejection double-mirror system.

The adsorption structure of the methoxy species on Cu(111) was determined by means of O *K*-edge EXAFS and NEXAFS with the new monochromator. The results are consistent with those obtained from the XPD measurements. Thanks to the high spectral resolution, the orientation of the species was properly determined and information about the electronic structure was obtained from a newly observed resonance. The methoxy adsorbate on Ni(111) was also studied with NEXAFS. The electronic properties for the methoxy species on Cu(111) and Ni(111) were comparatively related to the molecular bond lengths, which were also estimated from the NEXAFS data.

O *K*-edge XMCD spectra were for the first time recorded for the submonolayer amounts of light-element adsorbate; molecular CO and atomic O adsorbed on the *fcc*-Co(100) thin films. After the improvements of the circularly polarized x-ray source (*i.e.* the beamline) as well as the measuring setup, significant signals were obtained both for CO and O. The opposite alignments of the orbital magnetic moments for CO and O were suggested directly from the XMCD data, and the origins of this difference were discussed referring to a previous theoretical study.

As a future prospect, the reliability of the XAFS and XMCD spectra should be improved. In fact, some improvements have been performed from the XAFS measurements (chapter 4) to the XMCD ones (chapter 5). It is because quite high quality absorption spectra are required to obtain reliable XMCD data. A new electron detector was installed, at first, in order to obtain more reliable spectra with higher S/N ratio. Moreover, I modified the measuring setup and made it possible to keep the sample temperature at any point from 100 to 500 K. This improved the stability of the spectra, since it has been restricted by the surface contamination mainly due to the adsorption of the water in the vacuum system. The contamination ratio can be significantly

reduced by keeping the sample at ~200 K, which provides enough time to obtain the reliable data. These improvements are also effective to the XAFS measurements, of course. In addition, a fluorescence detector is now under commissioning to rise the signal-to-background (S/B) ratio.

The quality of the XMCD data can be drastically improved by changing the sample magnetization direction at each energy during the scan. The energy shift between two spectra, $\mu_{\uparrow\uparrow}$ and $\mu_{\uparrow\downarrow}$ is a serious problem in the present measurements, where the magnetization is reversed only at the start of each scan. The energy calibration procedure lowers the quality of the difference spectrum. A new control system is in preparation to make it possible to apply the magnetic field automatically.

As regards the determination of the surface structure, one must remember another powerful tool, *i.e.* XPD. Now that the high photon flux can be obtained over a wide energy range with the newly constructed monochromator, it is possible to perform the XPD measurements if one has a high sensitivity electron analyzer. Fortunately, a surface analyzing system equipped with a high-performance electron analyzer is now under construction. More reliable and detailed geometrical information about the surface adsorbates will be obtained with the combination of the XAFS and XPD techniques as described in §1-2-1.

In summary, it was demonstrated that the XAFS and XMCD techniques have great possibilities for investigating the structure, electronic property and magnetism of the surfaces. With these techniques one can clarify, for instance, the mechanism of the drastic changes in the surface magnetism caused by the molecular adsorption, by relating the extraordinary magnetism to the surface structures and electronic properties. The developments of the XAFS and XMCD measurements as well as the soft x-ray monochromator have opened up a wide road through the wilderness of the surface chemistry and surface magnetism.